ABSTRACT

FU, YUQIANG. Novel Strategies for Coupling 3D LES with ODT Solutions Based on Wavelet and Assimilation Methods. (Under the direction of Tarek Echekki.)

Downscaling and upscaling schemes for the hybird model of the Large eddy simulation (LES) and the One dimensional turbulence model (ODT) are developed and validated. The downscaling, which passes large scale velocity components information from the deterministic LES model to the subgrid closure stochastic ODT model using a wavelet-based approach. Upscaling scheme is implemented using the Kalman filter, which combines density information from ODT with density information advanced by the LES continuity equation.

The wavelet-based downscaling is achieved by collecting large-scale wavelet coefficients from the LES velocity components and small-scale wavelet coefficients from the ODT velocity components. The resulting velocity fields show better consistency with LES in large-scale and ODT in small-scale in both physical domain and Fourier domain. This is a significant improvement compared with the interpolation based downscaling scheme because the energy matching drives the ODT, which serves as a subgrid clousre model to be more consistent with LES.

The Kalman filter based upscaling is also implemented. The energy equation is not solved in LES for the LES-ODT formulation due to the fact that combustion happens mainly in subgrid scale. By the Kalman filter implementation, the LES density is corrected by the independently evolved filtered ODT density. This gives a smoother result compared with the filtered ODT density alone.

Novel Strategies for Coupling 3D LES with ODT Solutions Based on Wavelet and Assimilation Methods

by
Yuqiang Fu

A dissertation submitted to the Graduate Faculty of
North Carolina State University
in partial fulfillment of the
requirements for the Degree of
Doctor of Philosophy

Mechanical Engineering

Raleigh, North Carolina

2013

APPROVED BY:

Tiegang Fang	Hong Luo
Alexei Saveliev	Tarek Echekki Chair of Advisory Committee

DEDICATION

To my parents.

BIOGRAPHY

The author was born on February 17th, 1986 in Jiangyin, China. He obtained his Bachelor of Science degree in Thermal Energy and Power Engineering from Tsinghua University in July 2007. To further his study, he joined Purdue University in August 2008 and obtained a Master of Science degree in Aerospace Engineering in December 2010. Immediately after his graduation from Purdue University, he started his graduate work at North Carolina State University towards a Doctor of Philosophy degree in Mechanical Engineering.

ACKNOWLEDGEMENTS

I would like to thank my advisor Dr. Tarek Echekki, for his guidance toward my Ph.D. degree. His intelligence, brilliant technical insight and constant support benefit me a lot and I am very grateful. I would like to thank Dr. Alexei Saveliev, Dr. Hong Luo, Dr. Tiegang Fang and Dr. Helmut Hergeth for serving on my Ph.D. committee.

Also, I would like to appreciate my fiancee for her support. Thanks to all of my labmates for their help.

TABLE OF CONTENTS

LIST OF TABLES

LIST OF FIGURES

Chapter 1

Introduction

1.1 Background

Combustion is crucial to human life today since most of our energy consumption is generated through this process. The development of our society depends heavily upon our understanding of the science of combustion. In modern engineering applications, increasing combustion efficiency as well as keeping emission levels as low as possible is highly desirable. In most practical applications of combustion — such as internal combustion engines, industrial furnaces and jet engines — we encounter turbulent combustion. Instances of laminar combustion are rare. Many approaches have been developed to study turbulent combustion; and computational fluid dynamics (CFD) is one of them.

In the 1600s, Isaac Newton developed the laws of motion; and this led to the famous NavierCStokes equations, or N-S equations, named after Claude-Louis Navier and George Gabriel Stokes. So far, the N-S equations are the most accurate way of describing fluid motion, but the analytical solution of N-S equations still remains unknown. As such, CFD as an attempt to solve the equations numerically instead of analytically has gained great

popularity. There are three categories of CFD approaches right now — direct numerical simulation (DNS), Reynolds averaged Navier-Stokes (RANS) and large-eddy simulation (LES).

1. **Direct Numerical Simulation (DNS)**

   The first direct numerical simulation (DNS) computation was performed by Orszag and Patterson in 1972 [59] with a 32^3 grid and Reynolds number (based on Taylor microscale) of 35. In contrast, the largest DNS simulation in 2002 had the grid size of 4096^3 [35] and Reynolds number (based on Taylor microscale) of 1201. DNS is considered as the most accurate and conceptually the simplest approach in CFD, since it solves N-S equations directly without any modeling. Unlike other turbulence models, DNS has to solve from the smallest scale that turbulence has, which is considered as the Kolmogorov scale η, to the largest scale, the macroscopic scale L. Also, the DNS integration time step should be sufficiently small to satisfy accuracy and stability requirement of the discretization scheme. In most cases, a moderate DNS simulation requires millions of CPU-hours. A recent 3D DNS simulation of turbulent lifted hydrogen jet flame in a heated co-flow air costs 3.5 million CPU-hours using a top supercomputer for a computational domain of 24 mm by 32 mm by 6.4 mm with 0.07 ms time span [50].

   DNS is highly dependent on the computer processing speed. The computational cost for DNS increases proportionally with Re_L^3, which is the Reynolds number cube based on macroscopic scale. DNS was restricted for homogeneous flow in cubic computational domain for a long time; but now it has been used for more cases like channel flow [49], even with boundary layer treatment [85]. Nevertheless, solutions to most practical problems using DNS remains unfeasible in the foreseeable future,

despite the fact that with the consideration of chemical reaction, the computational cost of DNS increases approximately linearly with the number of chemical species [16]. But the importance of DNS cannot be underestimated as it is an excellent way of studying the fundamentals of turbulence and combustion [31, 68, 72, 28, 84, 85, 49, 35, 50, 11].

2. **Reynolds-Averaged Navier-Stokes (RANS)**

   While DNS is highly restricted by Reynolds number and geometry, Reynolds-Averaged Navier-Stokes (RANS) is an alternative for studying turbulent combustion. In DNS, 99% of the computational cost goes to the calculation of small scale energy, which contains only 20% of the total energy. By time or ensemble averaging of the instantaneous transport equation for mass, momentum and reactive scalars, RANS averages out small scale energy which costs most of the time in DNS. Yet these energy cannot be ignored, and closure models are needed, which is the most challenging task for RANS. Various closure models have been developed, like $k-\epsilon$ model, $k-\omega$ model. Moreover, a lot of variants of RANS have also been developed, including [26]

   (a) Unsteady RANS (U-RANS) [82, 70]: The Reynolds averaged equations and models are solved in three-dimensions with time dependence.

   (b) Time-dependent RANS (T-RANS) [36, 27, 37]: Comparing with the conventional RANS, the subgrid model of T-RANS covers only the incoherent or random fluctuations while the large scale information are fully resolved.

   (c) Hybrid RANS/LES: There are a lot of models that combine RANS with LES [21], including weighted sum of RANS and LES [56]. Another example is detached eddy simulation(DES) which uses RANS or LES in different regions

[78], for example, using RANS for near wall region and LES for the rest [13], *etc.*

3. **Large-Eddy Simulation (LES)**

   First proposed by Smagorinsky in 1963 [75], LES is gaining more and more popularity recently [65]. By filtering the instantaneous equations, the larger scale information is expressed explicitly, and similar to RANS, a challenge remains for the closure, known as the subgrid scale stress (SGS). Several subgrid scale stress models were proposed [63], including two-point closure [47], scale-similar and mixed models [71], one-equation model [24] and the most widely adopted dynamic model [23].

   Apart from subgrid closure, there are still other problems in LES. Although the computational cost of LES is much less than DNS, LES still cannot handle some complex cases, especially at high Reynolds number [66]. Computational power in the future might better meet the requirements of LES, but for now several alternatives have been developed, such as VLES (very-large eddy simulation) [51], DES (detached-eddy simulation) [81].

   In terms of computational cost, LES lies between DNS and RANS, but much closer to RANS than to DNS; as a matter of fact, most LES combustion models are derived from RANS model [66]. Compared to RANS, LES can provide significant advantages [64, 16]:

   (a) The large-scale motion of the turbulence that contains most of the turbulent kinetic energy and controls the dynamics of the turbulence is resolved.

   (b) Because of the band scale nature of LES (from filter scale Δ to macroscopic scale L), it can be easily implemented in a multiscale framework, such as LEMLES and ODTLES frameworks [10, 73].

There are also various new tools applied to the simulation of turbulence, like wavelet transform (WT) [18, 58], Kalman filter (KF) [6, 7], artificial neural network (ANN) [74], *etc*. Most of these new tools are coupled with LES to utilize the scale separation feature of LES.

1.2 Motivation

As discussed above, the simulation of turbulence itself is a challenging task and far from solved, whether in terms of mathematical and intuitive understanding, or in terms of obtaining engineering accuracy [77]. Adding combustion into turbulence introduces more challenges, such as [48, 16]:

1. There are some laminar flames whose thicknesses are much smaller than the Kolmogorov scale; and there are reactions whose rates are much faster than the turnover time of a Kolmogorov eddy. So, finer resolution and smaller time steps are required for DNS simulation of turbulent combustion which increases the computational cost of DNS dramatically.

2. Besides the subgrid-scale closure for LES and RANS model for turbulence, additional closure of the reaction terms are also needed. Moreover, approaches to the closure of the reaction terms that is applicable to general reacting flows is extremely difficult due to the fundamental differences between various combustion conditions.

3. Combustion itself is a complex chemical process involving heat release and a large number of species; and including all these species introduces a large number of equations that need to be solved.

LES is a very promising tool for the simulation of combustion, especially for the premixed turbulent combustion case, as it is inherently more complex than non-premixed because there is a much stronger coupling between chemistry and turbulence [2]. The reason that LES can handle combustion better than RANS is that LES explicitly resolves the large-scale unsteady motions that are known to play a significant role when the reactants are premixed. Also, premixed flames are sensitive to burner geometry and to large-scale, unsteady phenomena [2]. But a problem for LES is that premixed flames usually have very thin flame structure, which lie within one grid cell for LES. The difficulties inspire numerous multiscale hybrid models [10, 73].

1.3 LES Model and Closure for Turbulent Combustion

When applying LES filtering, the function of a filtered variable is not equal to the filtered function of the variable ($f(\tilde{x}) \neq \tilde{f}(x)$) for non-linear functions. Therefore, filtering the nonlinear momentum equation results in a residual term, the SGS stress; and closure is needed. In turbulent combustion, the chemical reaction is an even more nonlinear term governed by Arrhenius equation. Residual terms other than the SGS term show up on filtering the exponential terms of combustion. Even more, there is $N-1$ unclosed terms for N species because the sum of the their mole fraction adds up to unity $\sum X_i = 1$. In general, LES simulation of turbulent combustion containing N species results in N residue terms including SGS term and all of them need to be closed. All of the residual terms count for the information smaller than the filter size, and SGS term counts for the subgrid scale velocity fluctuation while the reaction rate residual term counts for the

subgrid scale combustion features.

As in turbulence without combustion, subgrid scale energy accounts for 20% of the total energy [65]; but in turbulent combustion, it is totally different as most combustion happens in a scale smaller than LES filter size. So LES itself cannot identify combustion features in most cases, but these combustion features cannot be ignored as the small scale combustion features will evolve and finally emerge with each other visible to large scale. This makes the closure of reaction rate terms important for these terms play a key role in turbulent combustion.

It is difficult to have the reaction rate closure for LES. But LES is still considered as one of the most promising models for turbulent combustion for several reasons [30]:

1. LES handles transport processes affected by the resolved, large-scale motions, and the modelling effort of turbulence is reduced to the residual motion structures.

2. Although LES experiences difficulties near the wall, important aspects of combustion processes, like main reactions, heat release, *etc.*, frequently take place far away from walls.

3. Because fresh and burned gas zones, having different turbulent characteristics, are instantaneously identified at the resolved grid level, a better description of turbulence-chemistry interactions can be expected.

There are two different types of subgrid scale models for combustion source term closure, either based on separation of scales and/or separation of model elements [16]. The eddy dissipation model (EDM) [52], the eddy break-up (EBU) [79] model and the non-premixed flamelet model [61] are among the first category. They both assume fast chemistry and reaction occurs on a smaller scale than the small scales of turbulence.

On the other hand, the Bray-Moss-Libby (BML) model [3] and the conditional moment closure (CMC) model [1] belong to the second category; both of them adopt a new variable — progress variable. The probability density function (PDF) of the progress variable is given in BML model while the transport equation of progress variable is derived in CMC model.

While the large scale mixing and combustion are supposed to be coupled with small scale mixing and combustion, the EDM and EBU models cut the connection between these scales by imposing assumptions. The BML and CMC models introduce a new variable to represent the coupling and give different solutions for different combustion modes (premixed and non-premixed flames). Structure-based models, such as the linear-eddy model (LEM) [38] and the one-dimensional turbulence (ODT) model [42], give an alternative way of modeling without imposing these assumptions. Here is a brief introduction for some selected models.

1.3.1 Flamelet Model

The flamelet model was first developed in the case of non-premixed combustion by Peters [61]. The assumption of the flamelet model is that the chemical timescales are short enough that reactions occur in a thin layer around stoichiometric mixture on a scale smaller than the small scales of turbulence [64].

The flamelet models were not used specifically for LES closure until Pierce & Moin developed the flamelet/progress variable (FPV) model [62]. As the name indicates, instead of solving transport equations for all the species, transport equations for the mixture fraction and the reaction progress variable are used to reduce the number of terms that need closure [62]. The closure for these two scalars, mixture fraction and progress variable, is

solved using a presumed probability density function (PDF) method.

The FPV model gives a different way of defining scalars for chemical reactions; and this model can give a better description of local extinction and reignition phenomena and flame lift-off. The challenge of the FPV model is that the FPDF of mixture fraction and reaction progress variable need to be provided in order to close the model. Also, it was found that the steady-state assumption of the flamelet solution during reignition at low scalar dissipation rate is inaccurate [62].

1.3.2 Conditional Moment Closure

The conditional moment closure (CMC) model was first proposed by Klimenko [46] and Bilger [1] for the RANS model [64]. It was adopted in LES formulation for non-premixed combustion by Kim & Pitsch [45]. By filtering conditionally on iso-surfaces of the mixture fraction, the small-scale mixing and chemical reactions are resolved. The closure for chemical reaction rates are given by assuming that fluctuations on iso-surfaces of the mixture fraction occurs only on the large scale, thus the conditionally filtered reaction rates are obtained [45]. The LES-CMC approach shows better results than the corresponding RANS-CMC approach due to resolved large-scale conditional fluctuations of the scalar dissipation rate and of reactive scalars. Also, the accuracy of CMC closure for LES is less sensitive to the level of local extinction than that of CMC for RANS [45].

The advantage for CMC model is that it uses conventional turbulent models to predict the flow and mixing fields with the capability of modeling more types of combustion than flamelet model [2]. The CMC model has already achieved a lot of success for a wide range of problems, but it also has limitations. It cannot be used for cases with radical species, which peak in thin layers within the filter scale. It is also important that the assumption of

statistical homogeneity be restricted to regions smaller than the large scales of turbulence [64].

1.3.3 The Linear-Eddy Model (LEM)

Proposed by Kerstein [38], the linear-eddy model (LEM) time advances the 1D unsteady diffusion-reaction equations, including associated dilatations along the 1D domain. This advancement is punctuated by instantaneous rearrangements of property profiles by mapping operations of a specified form. In effect, the outcome of each map constitutes a new initial condition for further time advancement [16]. The key feature of the LEM is the separate treatment of the two primary physical mechanisms that govern the scalar mixing process: turbulent stirring and molecular diffusion [22]. Despite its 1D nature, LEM can run by itself, and it has been proved that LEM on its own has the capability of simulating a variety of combustion cases, for example, shear layer mixing [39], Mixing and differential molecular diffusion in round jets [43], diffusion flame [41], *etc.* [39, 38, 40].

The modeling process concerns more about the subgrid scale information and their interaction with large scales instead of resolving all scales when the LEM serves as the subgrid closure for LES, known as the LEMLES model. For this reason, LEM domains are often embedded within LES grids in order to resolve the unresolved scales of LES. For example, an LEM domain can be embedded normal to the flame within each LES cell without the presentation of any physical Cartesian direction [16]. In the LEMLES model, convective transport of the scalar field across LES grid cells is accomplished by a splicing method. It is also shown that the LEMLES model is suitable for both premixed and non-premixed flames [76, 10]. Comparison with DNS was also performed and LEMLES results agree with DNS results [10]. It should also be noted that because the LEM domains in

each LES grid cell are independent of each other with communication occurs only at the large eddy time steps, the LESLEM formulation is ideally suited to implementation on parallel processing machines [22].

Despite the universal applications of LEMLES, it also shows some limitations. The eddy frequency and eddy size distribution that are essential for generating turbulence are prescribed by a predefined energy spectrum and flow properties are specified empirically by assigning parameters that govern the random event sequence [8]. Therefore, local turbulent properties like turbulent intensity are not fully considered. For flows whose turbulence properties are known empirically, this approach has been proven useful, but a more general model is required for general flows.

1.3.4 The One-Dimensional Turbulence (ODT) Model

A recent refinement of the LEM led to the one-dimensional turbulence (ODT) model [42]. The major difference between LEM and ODT lies in the probability distribution function (PDF) from which the maps representing turbulent eddies are sampled. The LEM is sampled as a fixed function form while in the ODT, the PDF is relevant with eddy time scale and local flow state. Therefore, a local and instantaneous representation of the flow state is required, which makes the ODT to be a fundamentally different type of model than the LEM [16]. Similar to the LEM, the stand-alone ODT model has been studied for many cases, like jet diffusion flames [15], buoyant fire plumes [67], auto ignition in jet flows [14], *etc.*, but in this thesis, the primary concern is ODT serveing as a subgrid closure for LES.

For the subgrid model of LES, known as the ODTLES formulation, ODT domains are embedded in LES solutions to resolve subgrid scale statistics. ODT domains can be fixed

in space (Eulerian formulation) or attached along the normal to the flame brush (Lagrangian formulation). Comparing with the LEMLES, the ODTLES presents additional advantages [16]:

1. ODT has the ability to provide closure for both scalars and momentum; thus, one has the flexibility to choose the closure for scalars or momentum or both.

2. In ODT, both momentum and scalars are coupled within ODT fine space and time resolutions which are comparable with DNS resolution; and this fine resolution coupling is very crucial near physical boundaries where the boundary conditions for both scalars and momentum are implemented.

3. In the LEMLES model, splicing method is used for large scale transport between different LEM segments. The LES-ODT formulation of Cao and Echekki [9] proposed an alternative representation for large scale transport based on ODT domains extending beyond a single LES cell, so the large scale transport along ODT domain direction can be resolved within ODT itself without interacting with other ODT domains or LES.

1.4 Objectives

The goal of this dissertation is to develop novel schemes of coupling between the LES and the ODT using the wavelet-based approaches for downscaling (information passing from large scale to small scale, or from the LES to the ODT in current LES-ODT framework) and the Kalman filter for upscaling (information passing from small scale to large scale, or from the ODT to the LES in current LES-ODT framework). Comparison between DNS and LES-ODT model with these novel coupling strategies are performed for various

turbulence and turbulent combustion cases, including isotropic turbulence cases, twin flame cases, *etc.* Also, wavelet and Fourier based spectra results for turbulent flows are proposed, showing the validity for the coupling schemes proposed in this dissertation in spectrum space. Besides the upscaling and downscaling, other applications based on wavelet transform and Kalman filter are also proposed, including adjusting turbulent intensity parameter in ODT and filtering combustion features from ODT.

1.5 Outline

The remainder of this dissertation is organized as follows. Chapter 2 introduces the LES-ODT formulation, including a detailed introduction for ODT, LES-ODT grid formulation as well as upscaling and downscaling. Chapter 3 presents information on the wavelet transform as well as the Fourier transform and the Short-Time Fourier transform. Chapter 4 addresses wavelet-based downscaling for LES-ODT formulation discussed in chapter 2. Other applications based on the wavelet transform are also discussed, which involve adjusting the main parameter for the ODT model using wavelet spectra and filtering turbulent combustion features. Chapter 5 introduces the Kalman filter and proposes a Kalman filter based smoothing scheme as the upscaling approach. This novel upscaling approach is further illustrated by comparing Fourier spectra of both LES and ODT. The final chapter presents general conclusions and provides recommendations for future work.

Chapter 2

LES-ODT Formulation

2.1 Objective

In this chapter, the LES-ODT model formulation is presented as well as the detailed description of ODT. ODT itself involves three simultaneous processes: eddy events, diffusion and convection; and all three will be introduced in detail later on. Most of the discussion is based on the dissertation of Cao [8].

2.2 LES-ODT Grid Formulation

The LES-ODT grid formulation represents a hybrid scheme of LES and ODT. Both LES and ODT occupy the entire computational domain. An example of the formulation proposed by Cao & Echekki [9] is shown in Figure 2.1. In Figure 2.1, only one xz plane slice and one xy plane slice for a $5 \times 5 \times 5$ case is shown for illustration. The common points between LES and ODT, as shown by large dots, are called nodes in the ODT formulation, which represent common intersection points between 3 ODT domains. The

fine small dots in the ODT formulation are ODT grid points. The ODT has a DNS-like resolution, which means the fine grids between LES grids should provide small scale information down to the Kolmogorov length scale for turbulence and fine reaction zones for combustion.

2.3 Governing Equation

2.3.1 LES governing equation

The LES governing equations are obtained by filtering the transport equations for momentum. The LES simulation serves as the basis of LES-ODT simulation. The LES governing equation are solved on their own, with small scale and reaction information passed from ODT. The LES governing equations are given as [8]

Continuity Equation:

$$\frac{\partial \bar{\rho}}{\partial t} + \frac{\partial \bar{\rho}\tilde{u_j}}{\partial x_j} = 0 \tag{2.1}$$

Momentum Equation:

$$\bar{\rho}\frac{\partial \tilde{u_i}}{\partial t} = \frac{\partial}{\partial x_j}\left[\bar{\rho}\left(\tilde{u_i}\tilde{u_j} - \widetilde{u_i u_j}\right)\right] + \left\{-\frac{\partial \bar{P}}{\partial x_i} - \bar{\rho}\tilde{u_j}\frac{\partial \tilde{u_i}}{\partial x_j} + \frac{\partial \bar{\tau}_{ij}}{\partial x_j}\right\} \tag{2.2}$$

In Eq. (2.2), the viscous stress τ_{ij} is expressed as

$$\tau_{ij} = \mu\left[\left(\frac{\partial u_i}{\partial x_j} + \frac{\partial u_j}{\partial x_i}\right)\right] - \frac{2}{3}\mu\delta_{ij}\frac{\partial u_k}{\partial x_k} \tag{2.3}$$

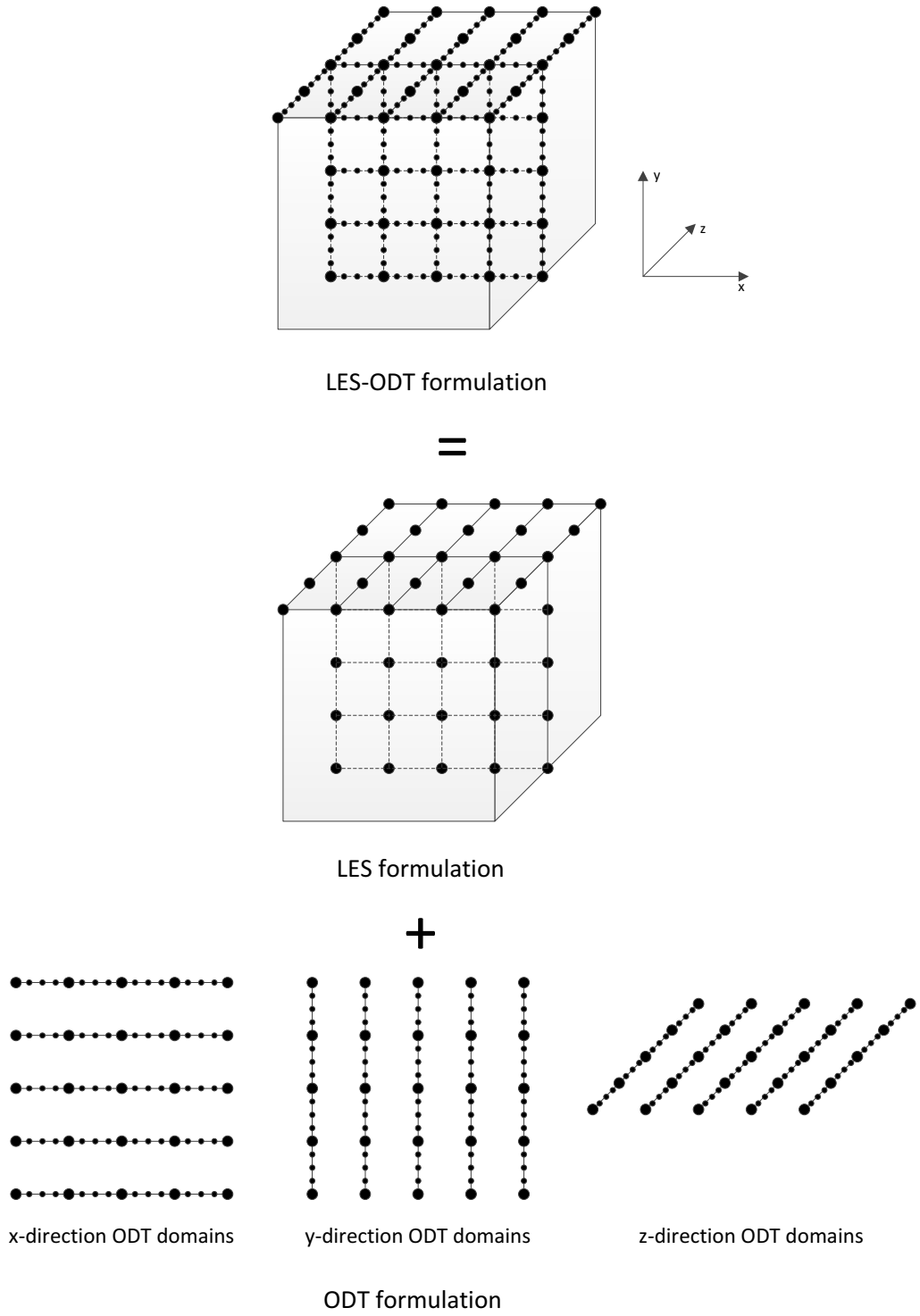

Figure 2.1: LES-ODT grid layout.

Here, " $\bar{}$ " means filtered quantity of LES; " $\tilde{}$ " means Farvre-averaging which is expressed as

$$\begin{cases} \phi = \tilde{\phi} + \phi'' \\ \tilde{\phi} = \dfrac{\overline{\rho\phi}}{\bar{\rho}} \end{cases} \tag{2.4}$$

The LES does not solve for the energy equation or the species equations because most of the turbulent combustion happens in a smaller scale than the LES filter scale. The subgrid stress is represented by $\bar{\rho}\left(\tilde{u}_i\tilde{u}_j - \widetilde{u_i u_j}\right)$ in the momentum equation; and it is modeled using a standard SGS stress model. For the cases in this dissertation, the Smagorinsky model is used.

The purpose of the LES governing equations in the LES-ODT formulation is to obtain the Favre-filtered velocity components $\tilde{u}_1$, $\tilde{u}_2$ and $\tilde{u}_3$. The filtered density $\bar{\rho}$ in LES does not account for the effect of heat release; therefore, it is obtained from the ODT solution.

2.3.2 ODT governing equation

The ODT governing equations are obtained from the instantaneous transport equation for scalars and momentum equation along 1D ODT domains with large-scale contributions from LES governing equations. The ODT governing equation can be expressed as [8]

Momentum Equation:

$$\rho\frac{\partial u_i}{\partial t} = \left[\frac{\partial}{\partial\eta}\left(\mu\frac{\partial u_i}{\partial\eta}\right) + \Omega_{u_i}\right] + \left\{-\frac{\partial\hat{P}}{\partial x_i} - \rho\hat{u}_j\frac{\partial u_i}{\partial x_j} + \frac{\partial\hat{\tau}_{i1}}{\partial x_1} + \frac{\partial\hat{\tau}_{i2}}{\partial x_2}\right\} \tag{2.5}$$

Energy Equation:

$$\rho\frac{\partial T}{\partial t} = \left[\frac{1}{c_P}\frac{\partial P}{\partial t} + \frac{1}{c_P}\frac{\partial \dot{q}''_\eta}{\partial \eta} - \frac{1}{c_P}\sum_{k=1}^{N} h_k\dot{\omega}_k + \Omega_T\right] + \frac{1}{c_P}\left\{-\rho\hat{u}_i\frac{\partial T}{\partial x_i} + \frac{\partial \hat{\dot{q}}''_1}{\partial x_1} + \frac{\partial \hat{\dot{q}}''_2}{\partial x_2}\right\} \tag{2.6}$$

Species Equation:

$$\rho\frac{\partial Y_k}{\partial t} = \left[\frac{\partial J_{k,\eta}}{\partial \eta} + \dot{\omega}_k + \Omega_{Y_k}\right] + \left\{-\rho\hat{u}_i\frac{\partial Y_k}{\partial x_i} + \frac{\partial \hat{J}_{k,1}}{\partial x_1} + \frac{\partial \hat{J}_{k,2}}{\partial x_2}\right\} \tag{2.7}$$

From Eqs. (2.5)–(2.7), η represents the spatial coordinate along with the ODT direction. Terms with a superscript " $\hat{}$ " represent information passing from LES, or downscaling, which will be discussed in detail later. Ω_{u_i}, Ω_T, Ω_{Y_k} represent stochastically implemented subgrid scale transport. The terms inside " [ ] " are directly modeled inside ODT; but the terms inside " { } " are not captured by the 1D ODT directions; and, therefore, they must be modeled, as discussed below.

The ODT within LES-ODT formulation consists of three parallel processes:

Turbulent transport: Subgrid-scale turbulent transport, which is represented stochastically, and is represented by Ω_{u_i}, Ω_T, Ω_{Y_k} in Eqs. (2.5)–(2.7). These terms are modeled with 'eddy event' in ODT.

Diffusion and reaction: Diffusion along with chemical reaction are represented in terms $\frac{\partial}{\partial \eta}\left(\mu\frac{\partial u_i}{\partial \eta}\right)$, $\frac{1}{c_P}\frac{\partial \dot{q}''_\eta}{\partial \eta} - \frac{1}{c_P}\sum_{k=1}^{N} h_k\dot{\omega}_k$ and $\frac{\partial J_{k,\eta}}{\partial \eta} + \dot{\omega}_k$ in Eqs. (2.5)–(2.7). These are 1D diffusive terms and can be numerically solved.

Convection: Convection involves the following terms: $-\rho\hat{u}_j\frac{\partial u_i}{\partial x_j}$, $-\rho\hat{u}_i\frac{\partial T}{\partial x_i}$ and $-\rho\hat{u}_i\frac{\partial Y_k}{\partial x_i}$ in Eqs. (2.5)–(2.7). Solving these terms involve node–convection at each ODT node along with intra–node relaxation along each ODT domain.

2.4 ODT Formulation—Subgrid Scale (SGS) Turbulent Transport

SGS turbulent transport is emulated by discrete eddy events; and one commonly used way for implementing eddy events is by using triplet maps [44] which were originally implemented within the context of LEM [40, 41]. The triplet map is applied to all three velocity components as well as all the scalar fields. Note that, as discussed later, the location and size of triplet map is sampled and selected.

2.4.1 Triplet map

The triplet map is the simplest mapping that can be used to emulate an eddy event and conserve energy at the same time. The triplet map is defined as [44]

$$f(y) \equiv y_0 + \begin{cases} 3(y-y_0) & \text{if } y_0 \le y \le y_0 + \frac{1}{3}l \\ 2l - 3(y-y_0) & \text{if } y_0 + \frac{1}{3}l < y \le y_0 + \frac{2}{3}l \\ 3(y-y_0) - 2l & \text{if } y_0 + \frac{2}{3}l \le y \le y_0 + l \\ y - y_0 & \text{otherwise} \end{cases} \tag{2.8}$$

$f(y)$ is the mapping function, y_0 is the starting location of the eddy and l is the length of the eddy. For eddy in the range $[y_0, y_0+l]$, given a coordinate y, $f(y)$ will give the location after the eddy event. For example, the velocity component $v(y)$ needs to be mapped, and after mapping, the velocity $v(y)$ profile becomes $v(f(y))$. The triplet map Eq. (2.8) takes a line segment $[y_0, y_0 + l]$, shrinks it to a third of its original length, $[y_0, y_0 + 1/3l]$, and then places three copies on the original domain at $[y_0, y_0+1/3l]$, $[y_0+1/3l, y_0+2/3l]$ and $[y_0+2/3l, y_0+l]$, and then the middle copy is inverted. This mapping maintains continuity

while emulateing the rotational effect of turbulent eddy motion [44]. A schematic view of the triplet map procedure is shown in Figure 2.2.

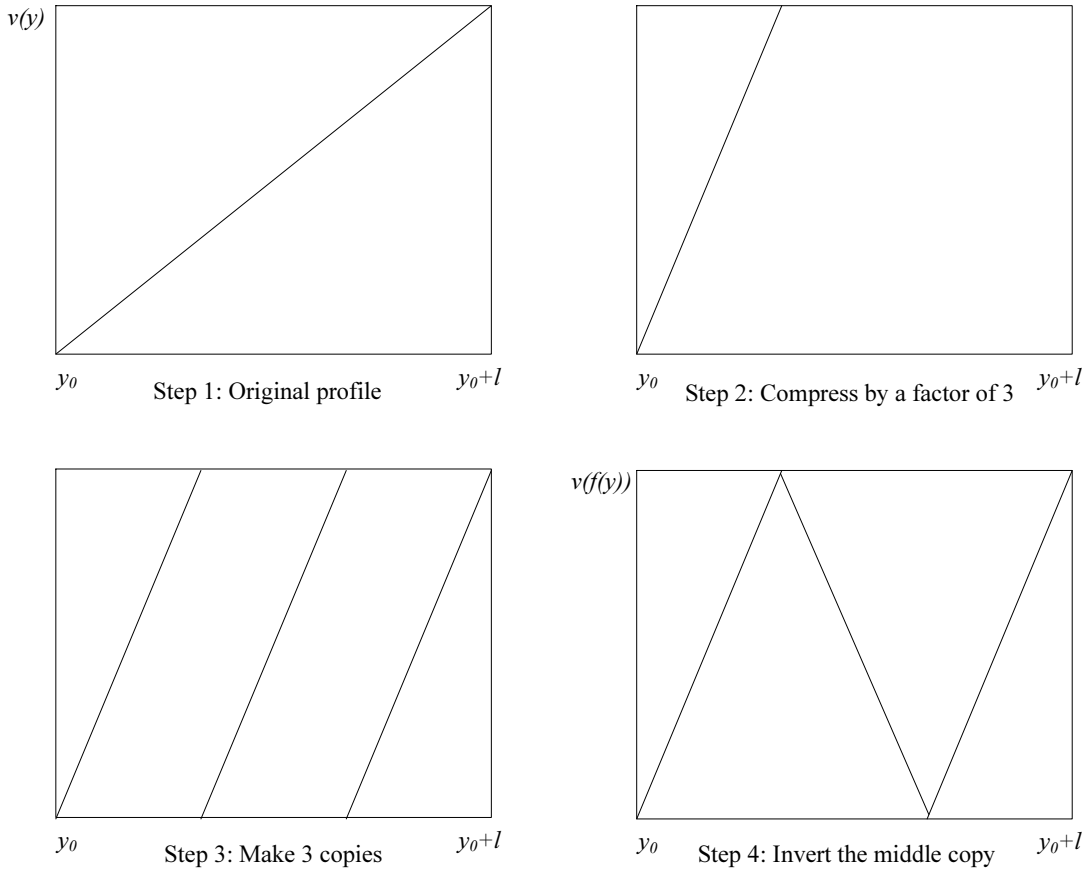

Figure 2.2: The triplet map procedure.

The discrete triplet map is defined under the condition that the length of the triplet

in term of the grid points should be a multiple of 3, and it is defined as [55]

$$f(j) \equiv j_0 + \begin{cases} 3(j-j_0) & \text{if } j_0 \le j \le j_0 + \frac{1}{3}ke \\ 2ke - 3(j-j_0) & \text{if } j_0 + \frac{1}{3}ke < j \le j_0 + \frac{2}{3}ke \\ 3(j-j_0) - 2ke & \text{if } j_0 + \frac{2}{3}ke \le j \le j_0 + ke \\ j - j_0 & \text{otherwise} \end{cases} \tag{2.9}$$

Here in Eq. (2.9), j_0 represents the starting location index of the eddy event; ke represents the length scale of the eddy event, and j is the grid index needs to be mapped while $f(j)$ is the grid index after mapping. The minimum length of an eddy event is 6 grid points, which corresponds to a length less than or equal to the Kolmogorov length scale δ, or

$$6\Delta x_{ODT} \le \delta \tag{2.10}$$

For further representation, Figure 2.3 shows a discrete triplet map for a 9 point eddy event. It is easy to identify from Eq. (2.8), Eq. (2.9) or from Figure 2.3, the triplet map implementation here as a permutation of grid indices; and the summation of the parameter over the whole domain does not change before and after the triplet map. Thus, a triplet map implementation conserves energy.

2.4.2 Pressure scrambling model

In the study of layer formulation in stably stratified turbulent flows, Wunsch & Kerstein [86] found that applying a triplet map to the density field will change the total potential energy while leaving the total kinetic energy unchanged. In order to ensure energy conservation, a kernel function $K(y)$ is added to the velocity field within every eddy event.

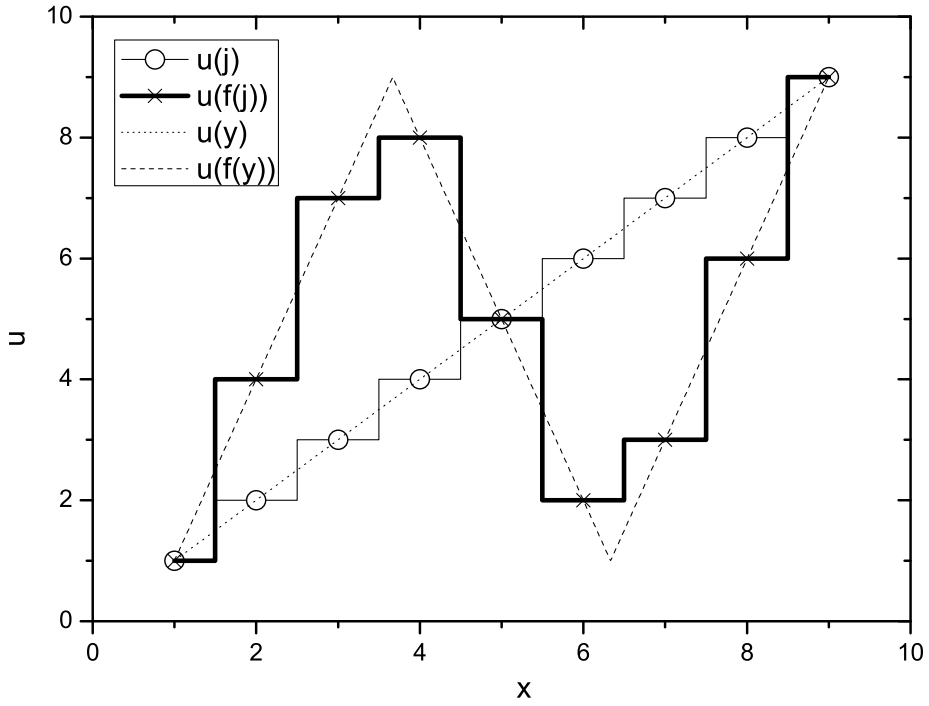

Figure 2.3: Discrete triplet map for a 9 point eddy, adapted from Mcdermott [55].

The kernel function $K(y)$ is defined as

$$K(y) \equiv y - f(y) \tag{2.11}$$

with $f(y)$ the triplet map function. The kernel function only has a non-zero value inside an eddy with zeros at both end of the eddy to maintain continuity. The eddy event maps the velocity and scalar fields with

$$\begin{aligned} v_i(y) &\longrightarrow v_i[f(y)] + c_i K(y), \\ \phi(y) &\longrightarrow \phi[f(y)]. \end{aligned} \tag{2.12}$$

The coefficients c_i are calculated for every velocity component based on energy conservation. The kinetic energy of an individual eddy for one velocity component is defined as

$$E_i \equiv \frac{1}{2} \int \rho v_i^2(y) dy. \tag{2.13}$$

The density ρ is defined as mass per unit length. Based on the kernel transformation, the kinetic energy change for an eddy after the mapping is

$$\begin{aligned} \Delta E_i &= \frac{1}{2}\rho \int_{y_0}^{y_0+l} \left[\left(v_i(f(y)) + c_i K(y) \right)^2 - v_i^2(y) \right] dy \\ &= \rho c l^2 v_{i,K} + \frac{2}{27} \rho l^3 c_i^2 \end{aligned} \tag{2.14}$$

The derivation of Eq. (2.14) is based on the definition

$$v_{i,K} \equiv \frac{1}{l^2} \int_{y_0}^{y_0+l} v_i(f(y)) K(y) dy \tag{2.15}$$

the energy conservation for a triplet map is

$$\int_{y_0}^{y_0+l} [v_i^2(f(y)) - v_i^2(y)]dy = 0 \tag{2.16}$$

and the identity derived directly from the definition of discrete triplet map function [8]

$$\int_{y_0}^{y_0+l} K^2(y)dy = \frac{4}{27}l^3 \tag{2.17}$$

Solving Eq. (2.14) for c_i gives

$$c_i = \frac{27}{4l}\left(-v_{i,K} \pm \sqrt{v_{i,K}^2 + \frac{8}{27}\frac{\Delta E_i}{\rho l}}\right) \tag{2.18}$$

Based on the energy conservation and the interpretation of pressure scrambling as a tendency to restore isotropy, Kerstein [44] found that the explicit form of the kinetic energy change ΔE_i must be of the form

$$\Delta E_i = \alpha \sum_j T_{i,j} Q_j \tag{2.19}$$

where $Q_j (j = 1, 2, 3)$ is a quantity with units of energy, α is a free parameter, and the transfer matrix $\boldsymbol{T}$ is defined as

$$\boldsymbol{T} = \frac{1}{2}\begin{bmatrix} -2 & 1 & 1 \\ 1 & -2 & 1 \\ 1 & 1 & -2 \end{bmatrix} \tag{2.20}$$

With the fact that the energy can be removed from an eddy is bounded, the bound is determined by maximizing $-\Delta E_i$ with respect to c_i in Eq. (2.14). Q_i is set to this value

because the coefficient α can then be interpreted as the fraction of the maximum possible energy extracted from each velocity component. Q_j is then obtained

$$Q_i = \frac{27}{8}\rho_0 l v_{i,K}^2 \tag{2.21}$$

Substitute into Eq. (2.18) gives the explicit expression of c_i [44]:

$$c_i = \frac{27}{4l}\left(-v_{i,K} + \mathrm{sgn}(v_{i,K})\sqrt{v_{i,K}^2 + \alpha\sum_j T_{ij} v_{j,K}^2}\right) \tag{2.22}$$

2.4.3 Eddy sampling

SGS turbulent transport in ODT is implemented stochastically; therefore, the eddy event used to emulate the turbulent stirring event needs to be sampled. There are two major questions associated with eddy sampling: how many eddy events should occur? and what size and position distributions for eddies should be adopted? The first question is addressed by eddy rate distribution. The second question is addressed by eddy size probability density function (PDF) and eddy location PDF.

Eddy rate distribution

The eddy event should occur with frequencies comparable to the turbulent eddy turnover time. The eddy rate is a function of y_0–starting location of an eddy; l–eddy size and t–time, which is denoted as $\lambda(y_0, l; t)$. The physical meaning of the eddy rate $\lambda(y_0, l; t)$ is the expected chance of occurance of an eddy with lower boundary between $[y_0, y_0 + l]$ and eddy size between $[l, l + dl]$ [16]. From dimensional analysis, the eddy rate distribution

can be defined as

$$\lambda(y_0, l; t) \equiv \frac{C}{l^2 \tau(y_0, l; t)} \tag{2.23}$$

where l is the eddy size; τ represents the time scale of an turbulent eddy; and C is an arbitrary constant. To estimate τ, Kerstein *et al.* [44] related it to turbulent kinetic energy and applied dimensional analysis, giving

$$\frac{\rho_0 l^3}{\tau^2(y_0, l)} \sim \sum_j B_j Q_j \tag{2.24}$$

where B_j are arbitrary dimensionless constants, and the quantities Q_j are the measurement of available kinetic energy based on the velocity components along with ODT domain direction. The calculation of Q_j is the same as in Eq. (2.21). Combing Eq. (2.24) with Eqs. (2.19)–(2.21) yields

$$\left(\frac{l}{\tau}\right)^2 \sim v_{i,K}^2 + \alpha \sum_j T_{ij} v_{i,K}^2 \tag{2.25}$$

Due to the damping effects of viscosity, any eddy with a time scale much longer than the corresponding viscous time scale τ_ν for that eddy size should be prohibited [44]. By introducing the viscous penalty constant, Eq. (2.25) should be rewritten as

$$\left(\frac{l}{\tau}\right)^2 \sim v_{i,K}^2 + \alpha \sum_j T_{ij} v_{i,K}^2 - Z\frac{\nu^2}{l^2} \tag{2.26}$$

with the viscous time scale

$$\tau_\nu \sim \frac{l^2}{\nu} \tag{2.27}$$

Combing Eq. (2.26) with the definition of the eddy rate Eq. (2.23) and with the coefficient in Eq. (2.26) being absorbed in the parameter C gives the eddy rate distribution

for i direction

$$\lambda(y_0, l; t) \equiv \frac{C}{l^2 \tau(y_0, l; t)} = \frac{C\nu}{l^4} \sqrt{\left(\frac{v_{i,K} l}{\nu}\right)^2 + \alpha \sum_j T_{ij} \left(\frac{v_{j,K} l}{\nu}\right)^2 - Z} \tag{2.28}$$

The three free parameters in the eddy rate distribution function Eq. (2.28), C, α and Z, are discussed as follows.

1. C : This parameter determines the intensity of the turbulence in the model; therefore, it also determines the Reynolds number of the turbulence.

2. α : The coefficient α determines how much kinetic energy is transferred between different velocity components or kinetic energy in different directions. For an ODT implementation without pressure scrambling, $\alpha = 0$; and the second term in the square root is dropped out.

3. Z : The viscous cutoff parameter determines the smallest eddy that can happen in the ODT simulation. With a small positive Z value, if the eddy is too small, or l in Eq. (2.28) is too small, the term under the square root will become negative; therefore, this eddy will be suppressed.

The acceptance probability

Instead of explicitly constructing and eddy rate PDF as of Eq. (2.28), the PDF of both l and y are needed; and even more, sampling l and y distribution across their entire range are required when sampling the eddy rate distribution. Instead of sampling three PDFs at the same time, which is extremely expensive, the 'rejection method' [69] is implemented [15]. In this approach, the acceptance probability is proposed based on the PDFs of λ, f, and g. $f(l)$ and $g(y_0)$ are the presumed PDFs of the eddy length l and the eddy location

y_0. The trial values are proposed based on the sampling of λ, f and g and then accepted with a probability—the acceptance probability. Following Echekki [15], the acceptance probability is calculated as

$$P_a = \frac{\lambda(y_0, l:t)\Delta t_s}{f(l)g(y_0)} \tag{2.29}$$

Δt_s is the time step between successive eddy events. The adjustment of Δt_s is very important in the ODT implementation. It must be chosen to be reasonably small in order for the value of P_a below unity. If Δt_s is too small, which yields the value of P_a much smaller than unity, stirring events are over-sampled, resulting in a higher computational cost than needed. If the choice of Δt_s is too large, it is even worse. The value of P_a can go over unity; therefore, the stirring events are under-sampled. In that case there are not enough eddies, which may generate unrealistic results.

The form of f and g are not unique. In fact, any PDFs of f and g will result in the right distribution since ODT tries to build its own distribution. Following Kerstein [42] and Echekki [15], a reasonable guess for the f and g forms are as follows.

Eddy distribution

The eddy size has the presumed distribution of [15]

$$f(l) = \frac{A}{l^2} \tag{2.30}$$

A is a constant and l is the eddy size. A is determined by satisfying $f(l)$ by PDF criteria

$$\int_a^b f(l)dl = 1 \tag{2.31}$$

where a is the smallest eddy size and b is the largest eddy size. Substituting Eq. (2.30) into Eq. (2.31) gives

$$A = \frac{ab}{b-a} \tag{2.32}$$

Thus, the eddy size distribution is given as

$$f(l) = \frac{ab}{b-a}\frac{1}{l^2} \tag{2.33}$$

Eddy location distribution

The presumed eddy location PDF is a uniform distribution function over the whole ODT domain and can be expressed as

$$g(y_0) = \frac{1}{L} \tag{2.34}$$

L is the length of ODT domain.

2.4.4 The ODT parameter

There is only one ODT free parameter, denoted as C in the eddy rate distribution Eq. (2.28). It was used in the original ODT formulation [42] and many other ODT applications. The parameter C influences a number of physical parameters. It determines the time scale of the eddy event from Eq. (2.28). C in Eq. (2.28) is proportional to the eddy rate distribution function $\lambda(y_0, l : t)$; thus proportional to the number of successful eddy events (not rejected by the acceptance probability). As the eddy event is an energy cascade process, with energy cascading from scale l to scale $l/3$, C is also proportional to the energy transfer rate across scales and the intensity of turbulence. In this case, C is also proportional to the turbulent Reynolds number Re, which is also an indicator of turbulence intensity [42]. In any case, C is a crucial parameter for the turbulence and

determining the value of it is important for the implementation of ODT.

Kerstein [42] proposed several ways to determine the value of C empirically for limited types of turbulent flows. In the freely-decaying turbulence, by applying the isotropy condition $< u'^2 >=< v'^2 >$, the empirical value of C is obtained in the simulation. Also for the wall bounded flow, an optimal C value is obtained to match the friction law and growth law of the spatially-developing planar boundary layer. These approaches are purely empirical and limited to several types of turbulent flow. The approach to present a universal way of determining the C constant is developed in this dissertation in the LES-ODT formulation by matching the wavelet spectra between LES and ODT. This ensures that the ODT matches the LES turbulent intensity.

2.5 ODT Formulation—Diffusion and Reaction

Molecular diffusion and reaction terms are represented by deterministic solutions of the 1D transport equation. The governing equation for diffusion and reaction process in ODT is represented as [8]

Diffusion for velocity:

$$\rho \frac{\partial u_i}{\partial t} = \frac{\partial}{\partial \eta}\left(\mu \frac{\partial u_i}{\partial \eta}\right) \tag{2.35}$$

Reaction–diffusion for temperature:

$$\rho \frac{\partial T}{\partial t} = \frac{1}{c_P}\frac{\partial \dot{q}''_\eta}{\partial \eta} - \frac{1}{c_P}\sum_{k=1}^{N} h_k \dot{\omega}_k \tag{2.36}$$

Reaction–diffusion for mass fractions:

$$\rho \frac{\partial Y_k}{\partial t} = \frac{\partial J_{k,\eta}}{\partial \eta} + \dot{\omega}_k \tag{2.37}$$

In the LES-ODT implementation, the diffusion terms in the governing equation is multiplied by a factor of 3 to account for the diffusion in the other two directions normal to the ODT domain under the assumption of local isotropy [8].

2.6 ODT Formulation—Large-Scale Convection

The convection process is adopted through two steps: node convection and intra-node relaxation [8]. Since ODT does not have any information normal to its orientation, *e.g.*, x-direction ODT domains does not have y-direction or z-direction information, it is assumed that diffusion from directions normal to ODT orientation will pass through ODT nodes, and the convection terms for ODT nodes are calculated using coarse grid information from LES as nodes lay on both LES and ODT. This process is called node convection; and the intra-node relaxation is applied for the rest of ODT points that do not intersect with LES. It is adopted by assuming that the convection for these ODT points only take place in one direction—the ODT orientation. The transport equation for ODT convection process is expressed as [8]

Convection for velocity:

$$\frac{\partial u_i}{\partial t} = -\hat{u}_j \frac{\partial u_i}{\partial x_j} \tag{2.38}$$

Convection for temperature:

$$\frac{\partial T}{\partial t} = -\hat{u}_j \frac{\partial T}{\partial x_j} \tag{2.39}$$

Convection for mass fractions:

$$\frac{\partial Y_k}{\partial t} = -\hat{u}_j \frac{\partial Y_k}{\partial x_j} \tag{2.40}$$

and $\hat{u}_j$ represents velocity resolved by LES.

The two types of convection, node convection and intra-node convection, are adopted differently. The node convection involves the summations from three directions within Eqs. (2.38)–(2.40) at the nodes. All information for node convection comes from the LES solution. As for every node, there are three ODT domains that go through it. Thus, the solution value at the nodes after the node convection are the average between the three ODT domains.

For the intra-node convection, in order to simulate the effect from the other two directions, the governing equation can be rewritten as

Convection for velocity:

$$\frac{\partial u}{\partial t} = -\kappa \hat{u} \frac{\partial u}{\partial \eta} \tag{2.41}$$

Convection for temperature:

$$\frac{\partial T}{\partial t} = -\kappa \hat{u} \frac{\partial T}{\partial \eta} \tag{2.42}$$

Convection for mass fractions:

$$\frac{\partial Y_k}{\partial t} = -\kappa \hat{u} \frac{\partial Y_k}{\partial \eta} \tag{2.43}$$

where η is the spatial coordinate along ODT direction. κ is set to 3 in this case to simulate the effect from all three directions.

2.7 ODT Implementation

The ODT implementation can be divided into three parallel processes: ODT diffusion, ODT stirring and ODT convection, as shown in Figure 2.4. The three parallel processes have their own time steps. The three time steps need to be comparable with the DNS time step and much smaller than the LES time step. The ODT time step, which is used to synchronize the three parallel processes with the LES process, is set the same as the LES time step. At each ODT time step, the time of three processes are set first; then the processes are executed based on which process has the smallest time until all three processes reach the ODT time step. For every LES time step, all ODT domains will excuse the procedure in Figure 2.4 once.

2.8 LES-ODT Coupling

The LES-ODT coupling is carried out both spatially and temporally. The spatial coupling of LES-ODT takes care of the information exchange between LES and ODT. Passing information from LES to ODT is carried out by downscaling; and passing information from ODT to LES is done by upscaling. Due to the different time steps involved in the formulation, temporal coupling is done to synchronize the time between LES and ODT.

2.8.1 LES-ODT Spatial Coupling

Cao [8] proposed the tri-linear interpolation of the velocity components for the down-scaling process which is the 3D extension of linear interpolation. The upscaling process

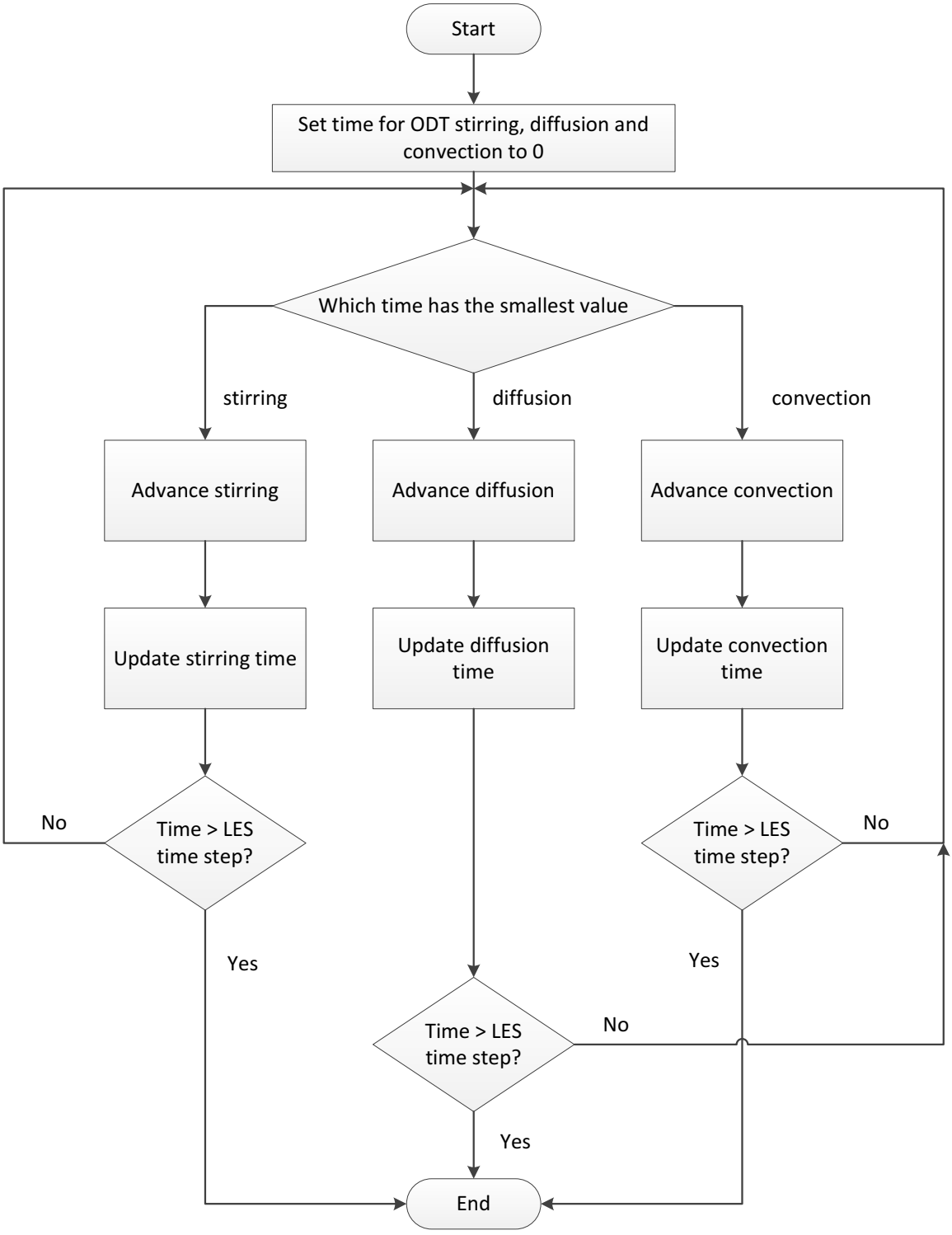

Figure 2.4: Flowchart for ODT procedure.

is achieved by filtering the density field from ODT to LES. The filtering is defined as

$$\bar{f}(x) = \int f(x')G(x - x')dx. \tag{2.44}$$

The integration is carried out over the entire domain; $\bar{f}$ is the filtered function; f is the original function; and G is the filter function. In the LES-ODT formulation proposed by Cao & Echekki [9], box filter function is used. With the box filter, the filtered function $\bar{f}(x)$ is the average of the original function $f(x')$ within the interval $x-\frac{1}{2}\Delta < x' < x+\frac{1}{2}\Delta$, or mathematically expressed as

$$G(x') = \begin{cases} 0, & |x - x'| > \dfrac{\Delta}{2} \\ \dfrac{1}{\Delta}, & |x - x'| < \dfrac{\Delta}{2} \end{cases} \tag{2.45}$$

The schematic illustration of the downscaling and upscaling is shown in Figure 2.5. The novel strategy of spatial coupling based on wavelet transform and Kalman filter for both upscaling and downscaling will be discussed in later chapters. Inspired by the fact that redundancy presents for the velocity field; while both LES and ODT solve for momentum equations, it is desirable to establish a downscaling scheme based on both velocity fields. Instead of passing velocity information from LES to ODT, both velocity fields are used in order to get a compounded velocity field that has large scale velocity information from LES and small scale velocity information from ODT. The Kalman filter based upscaling scheme proposed in this dissertation is based on the redundancy of the density field from both LES and ODT. With the consideration of the error caused by the filtering the ODT density and the truncation error of the LES, the Kalman filter combines both LES and ODT density fields to get an optimal density field with the consideration

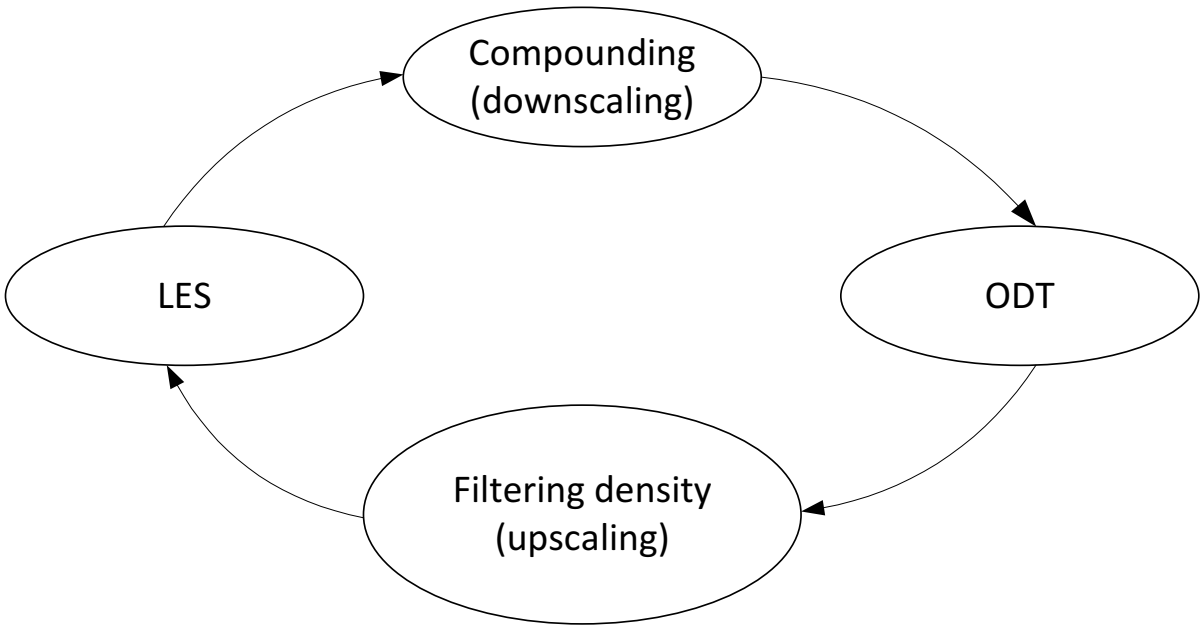

Figure 2.5: Upscaling and Downscaling for LES-ODT Formulation

of the errors of both LES and ODT density fields.

2.8.2 LES-ODT Temporal Synchronization

LES and ODT are integrated and solved simultaneously. Since LES has different time steps as ODT stirring, diffusion and convection, they have to synchronize with each other. In order to have good spatial coupling, LES and ODT are advanced alternatively with a time difference of half a LES time step as shown in Figure 2.6.

First, ODT advances half a LES time step, meaning stirring, diffusion and convection advance until Δt_{LES} is reached; then LES catches up by one whole LES time step Δt_{LES}, and ODT takes turn, until a certain LES time step is reached. Therefore, there is a time shift between LES and ODT by half a LES time step. For spatial downscaling, the coupled LES and ODT velocity fields are used over the entire ODT integration time

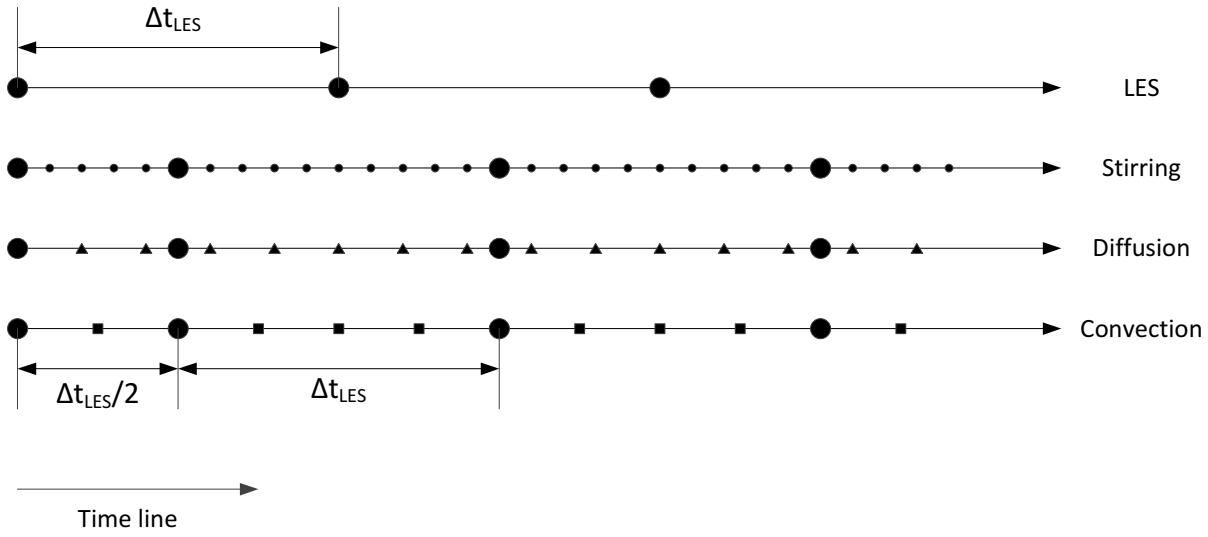

Figure 2.6: Temporal Synchronization between LES and ODT(adapted from Cao [8])

step, therefore, using the value in the middle gives better accuracy. The same approach is used for upscaling, where the filtered density that passes into LES is most accurate at half LES time step.

2.9 Numerical Implementation for LES-ODT Coupling

The flowchart for LES-ODT formulation is shown in Figure 2.7. ODT is first initialized from a fine grid initial state, like DNS initial solution. Then, LES is initialized from ODT by filtering the ODT solution. Then, LES and ODT are integrated alternatively with LES-ODT velocity field compounding right before ODT integration and density filtering from ODT to LES before LES integration. The program will stop after reaching a certain LES time.

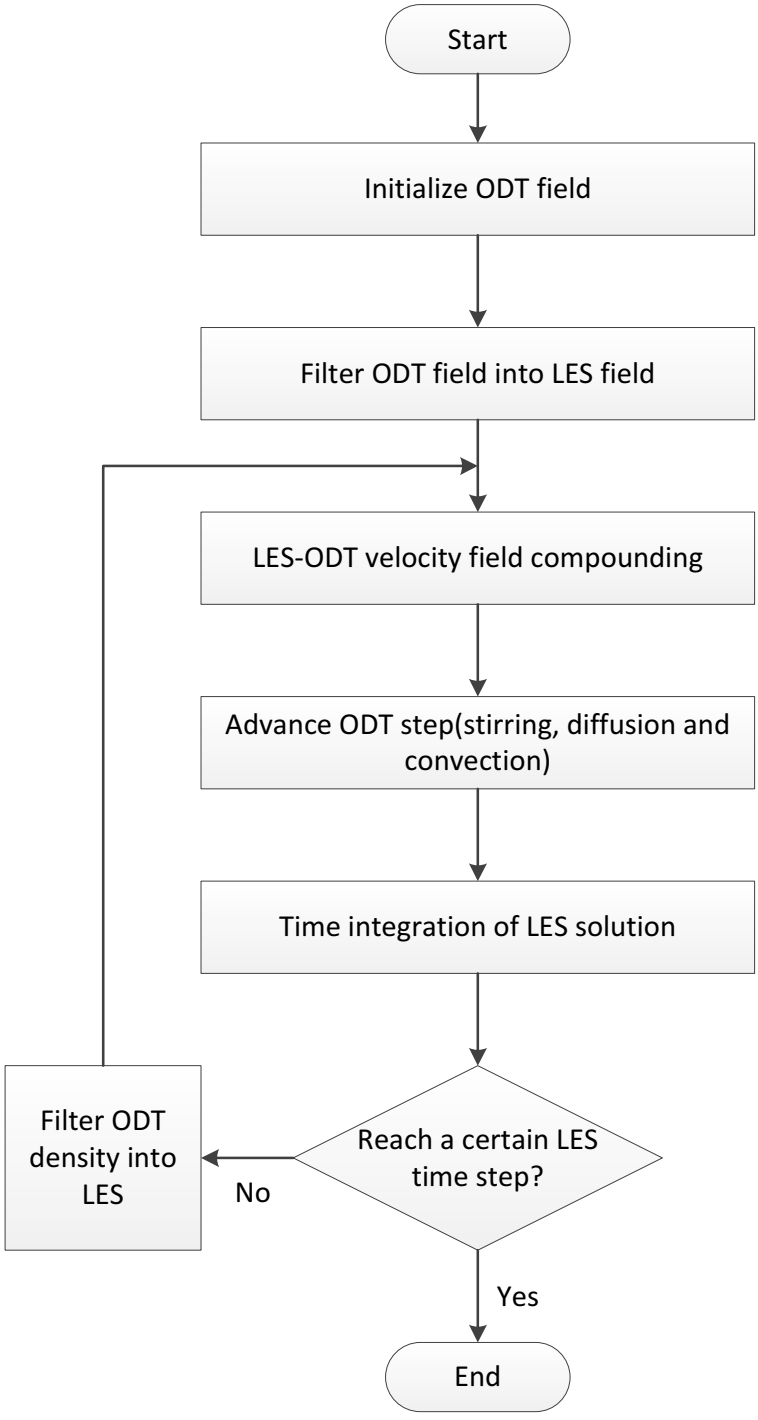

Figure 2.7: Flowchart for LES-ODT formulation

Chapter 3

Wavelet Transform and Multiresolution Analysis

3.1 Introduction and Motivation

The original LES-ODT downscaling presented in Cao's dissertation [8] involves a replacement of the large-scale velocity component in the ODT solution by the LES solution using interpolation. Tri-linear interpolation was adopted for the downscaling by Cao [8] which is a 3D extension of 1D linear interpolation. It is implemented to interpolate LES resolved velocity field into ODT grid during simulation. In the present work we implement wavelet analysis as a multiresolution tool to both correct the large-scale velocity field in ODT and to filter the ODT density onto the LES grid. In this chapter, basic ideas of wavelet transform as well as other famous transforms will be presented with emphasis on Fourier transform and short-time Fourier transform.

3.2 The Fourier Transform

3.2.1 The Continuous Fourier Transform

The Fourier transform was first developed by Joseph Fourier. Fast Fourier transform (FFT), an algorithm to compute the discrete Fourier transform, is one of the most widely adopted algorithms in engineering, science and mathematics. Mathematical expression of Fourier transform is given as

$$F(\omega) = \frac{1}{\sqrt{2\pi}} \int_{-\infty}^{\infty} f(t)\ e^{-\pi i \omega t} dt. \tag{3.1}$$

While the inverse Fourier transform is expressed as

$$f(t) = \frac{1}{\sqrt{2\pi}} \int_{-\infty}^{\infty} F(\omega)\ e^{\pi i \omega t} d\omega. \tag{3.2}$$

In Eq. (3.1) and Eq. (3.2), $f(t)$ is the original function which is ready to be transformed, and it is a function of t. For most cases in turbulence, t can be either distance/location or time. ω is the frequency and the output F is a function of frequency only. The purpose of the Fourier transform is to transform of a function from time/space domain into frequency/wave number domain.

Take the following function as an example

$$f(t) = \begin{cases} \cos(2\pi \cdot 20t) + \cos(2\pi \cdot 50t) & \text{for } 0 \leq t \leq 0.4 \\ 0 & \text{elsewhere} \end{cases}. \tag{3.3}$$

By using the Fourier transform table [34], the result of the Fourier transform is given as

$$F(f(t)) = \frac{1}{2}\delta(\omega + 20) + \frac{1}{2}\delta(\omega - 20) + \frac{1}{2}\delta(\omega + 50) + \frac{1}{2}\delta(\omega - 50). \tag{3.4}$$

δ is the Dirac delta function which has the definition

$$\delta(t) = \begin{cases} +\infty, & x = 0 \\ 0, & x \neq 0 \end{cases} \tag{3.5}$$

while satisfying the identity

$$\int_{-\infty}^{+\infty} \delta(x)dx = 1. \tag{3.6}$$

The Fourier transform of Eq. (3.3) as shown in Eq. (3.4) has four peaks at $\omega = -20$, $\omega = -50$, $\omega = 20$ and $\omega = 50$, discarding the negative frequencies which have no physical meaning gives the two frequencies shown in Eq. (3.3), 20Hz and 50Hz.

3.2.2 The Discrete Fourier Transform

The Discrete Fourier transform (DFT) of a sequence $x_0, x_1, \cdots, x_{N-1}$ can be expressed as

$$X_k = \sum_{N=0}^{N-1} x_n \cdot e^{-i\pi kn/N} \tag{3.7}$$

and the inverse Discrete Fourier transform is expressed as

$$x_n = \frac{1}{N} \sum_{k=0}^{N-1} X_k \cdot e^{i\pi kn/N} \tag{3.8}$$

The discrete Fourier transform of Eq. (3.3) is shown in Figure 3.1, the transform results in two peaks at 20Hz and 50Hz also.

(a) Plot of Eq. (3.3)

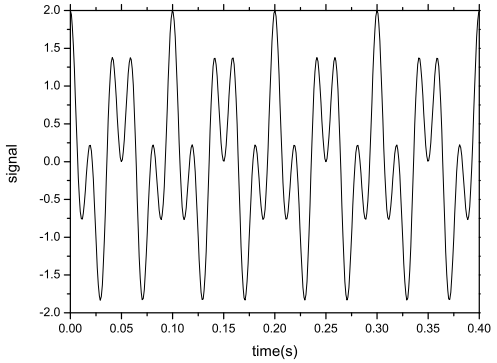

(b) DFT of Eq. (3.3)

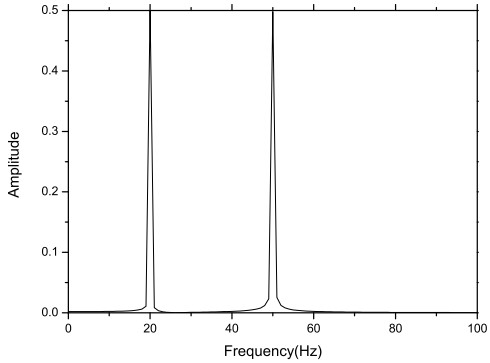

Figure 3.1: Eq. (3.3) and its DFT result

3.2.3 The Fast Wavelet Transform

The Fast Fourier transform (FFT) is designed to yield exactly the same result as Discrete Fourier transform formula of Eq. (3.7), but much faster in terms of computational time. In almost every aspect, FFT is superior to DFT. For most engineering problems as well as in this dissertation, DFT is the same as FFT unless explicitly stated.

3.3 The Short-Time Fourier Transform

The Fourier transform is great for some engineering applications, but not all of them. As presented in Eq. (3.1), the integration is applied over the whole time span, which means that when an event happens (which shows up in the function x) at a different time, it does not really matter in terms of Fourier transform. But in most turbulent combustion cases, knowing when combustion happens is not enough, knowing where it happens is also critical.

In order to illustrate the limitation of the Fourier transform visually, a function is given as

$$x = \begin{cases} 2\cos(2\pi \cdot 20t) & \text{when } 0 \leq t \leq 0.2 \\ 2\cos(2\pi \cdot 50t) & \text{when } 0.2 < t \leq 0.4 \\ 0 & \text{elsewhere} \end{cases} \tag{3.9}$$

The function as well as its FFT result is shown in Figure 3.2. By comparing with Figure 3.1, the results are very similar; the peaks are in the same frequency and they have the same magnitudes. The difference between Eq. (3.3) and Eq. (3.9) is significant, but the difference between their Fourier transform results is limited, and this kind of issues related with time/location–frequency motivates the use of the short-time Fourier transform.

(a) Plot of Eq. (3.9)

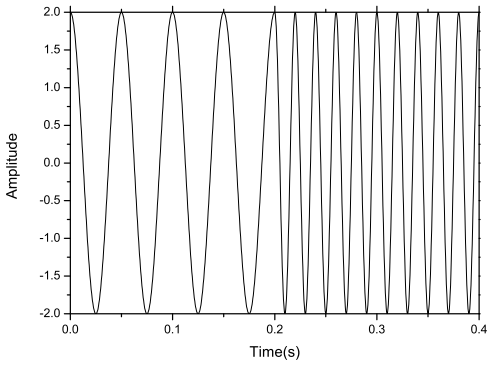

(b) FFT of Eq. (3.9)

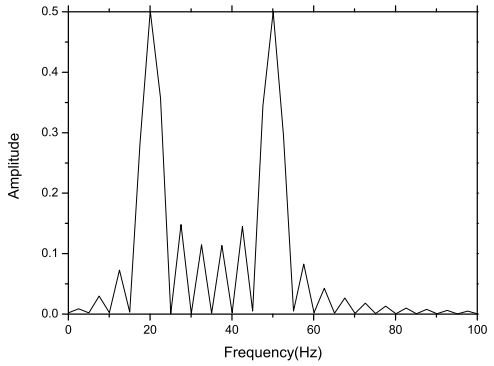

Figure 3.2: Eq. (3.9) and its FFT result.

3.3.1 The Window Function

The idea of the short-time Fourier transform is to apply a 'window' for the original signal $x(t)$, and the ideal case for the 'window' is to retain part of the signal that we are interested in and set everything else to zero. Mathematically, it is designed as a window function, and by multiplying the window function with the original signal, part of signal is remained and the rest becomes zero.

There are a lot of window functions, such as the rectangular window function, the triangular window function, the Hanning window function, the Gaussian window function, *etc.* Plots of a few window functions are shown in Figure 3.3. All the window functions should be localized within a narrow band.

3.3.2 The Short-Time Fourier Transform

With the idea of the window function, the approximate frequency contents of a signal $f(t)$ within a certain range in the physical domain can be obtained by first windowing the function using an appropriate window function $\phi(t)$ to produce the windowed function $f_b(t) = f(t)\phi(t-b)$, and then a Fourier transform is applied to the windowed function. Therefore, the short-time Fourier transform (STFT) may be defined as

$$STFT(b,\omega) = \frac{1}{\sqrt{2\pi}} \int_{-\infty}^{\infty} f(t)\phi(t-b)e^{-i\omega t}dt \tag{3.10}$$

and the inverse STFT is given as

$$\phi(t-b)f(t) = \frac{1}{\sqrt{2\pi}} \int_{-\infty}^{\infty} STFT(b,\omega)e^{i\omega t}d\omega \tag{3.11}$$

(a) Rectangular Window Function

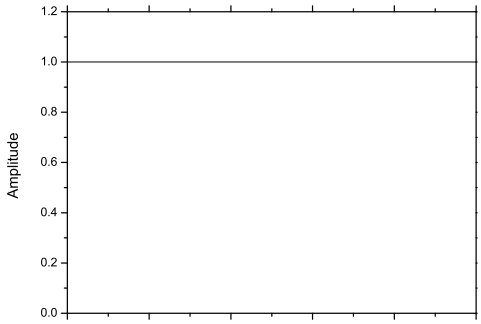

(b) Triangular Window Function

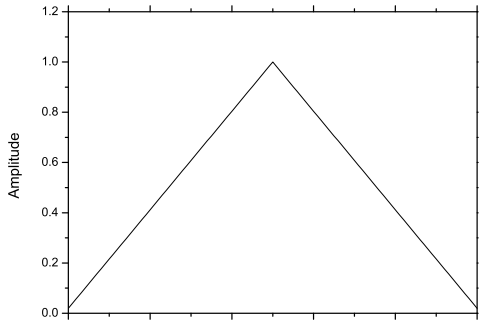

(c) Hanning Window Function

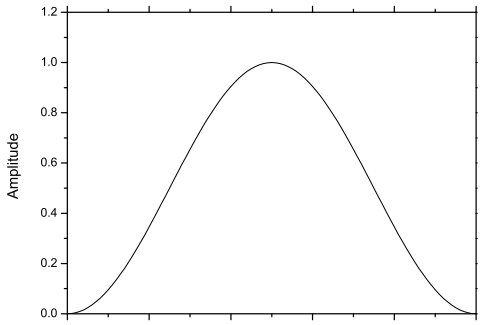

(d) Gaussian Window Function

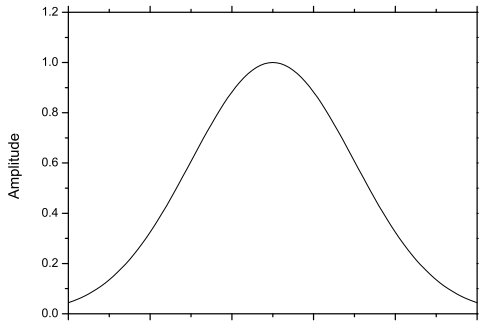

Figure 3.3: Some Window Functions

As can be noted from Eq. (3.10) and Eq. (3.11), the STFT and the inverse STFT are the Fourier transform and inverse Fourier transform of $f(t)\phi(t-b)$, the input function times a window function. The result of STFT is a function of frequency ω and location b, which is very direct and intuitive with the concept of window function.

Using STFT, the function shown above as restated in Eq. (3.12) can be better analyzed.

$$x(t) = \begin{cases} 2\cos(2\pi \cdot 20t) & \text{when } 0 \leq t \leq 0.2 \\ 2\cos(2\pi \cdot 50t) & \text{when } 0.2 < t \leq 0.4 \\ 0 & \text{elsewhere} \end{cases} \tag{3.12}$$

The STFT result as well as the original function is shown in Figure 3.4. On the right frequency–time graph, the brightness indicates the value or magnitude of the frequency at a certain time. As a matter of fact, in STFT, it is better to describe that there is a certain range of frequency exists within a certain range of physical domain (window size). Frequency and location cannot be both accurate, which is related to an important concept in multiresolution analysis called the uncertainty principle.

3.3.3 The Uncertainty Principle

The uncertainty principle is described as follows: One cannot know the exact time and frequency of a signal or, more precisely, the product of the time resolution and the frequency resolution should be greater than or equal to $1/4\pi$,

$$\Delta t \Delta f \geq \frac{1}{4\pi} \tag{3.13}$$

This principle is valid for any frequency–time analysis approach; whether it is Fourier transform, STFT or the wavelet transform which will be introduced later. The STFT of

(a) Plot of Eq. (3.12)

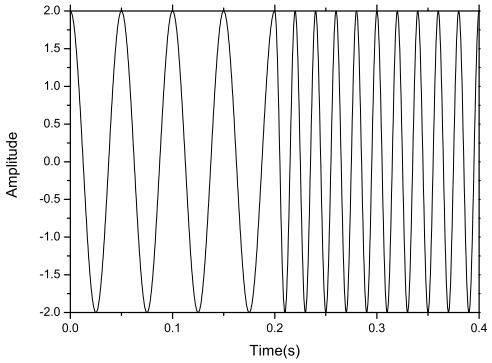

(b) STFT of Eq. (3.12)

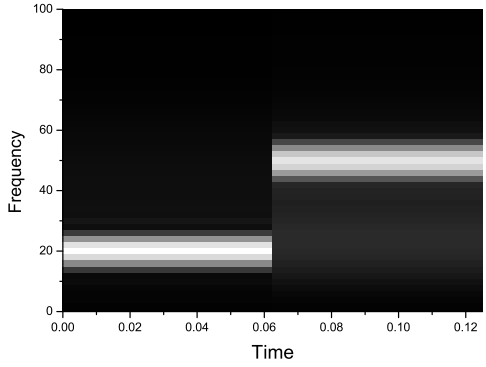

Figure 3.4: Eq. (3.9) and its STFT result

Eq. (3.12) of different frequency–time resolution is shown in Figure 3.5. The signal has a total number of 1000 data points. Figure 3.5a has the narrowest window and Figure 3.5d has the widest window, which means Figure 3.5a has the best time resolution and, of course, the worst frequency resolution; and Figure 3.5d has the worst time resolution and the best frequency resolution. Actually, Figure 3.5a is similar to the original function as shown in the left part of Figure 3.4, and Figure 3.5d is similar to the FFT result shown in the right part of Figure 3.4. Considering two extremes, the best time resolution that is accurate in time gives absolutely no frequency resolution, which is the original signal, and the best frequency resolution which is accurate in frequency gives no time resolution which is the Fourier transform. This can be further proved as in Eq. (3.14) and Eq. (3.15). By selecting an window function $\phi(t) = 1$, which means that the time resolution is the worst, and we get the accurate frequency result or Fourier transform as shown in Eq. (3.14). by selecting a window function $\phi(t) = \delta(t)$, which has the best time resolution gives the worst frequency resolution or the original signal as shown in

Eq. (3.15).

$$\mathrm{STFT}(t', f) = \int_{-\infty}^{\infty} f(t) e^{-j\pi f t} dt = \int_{-\infty}^{\infty} x(t) e^{-j\pi f t} dt = \mathrm{FT}(f) \tag{3.14}$$

$$\mathrm{STFT}(t', f) = \int_{-\infty}^{\infty} x(t)\delta(t - t') e^{-j\pi f t} dt = x(t') e^{-jft'} \tag{3.15}$$

(a) 2 Points Window STFT

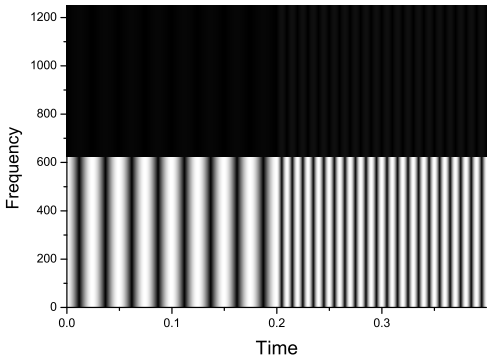

(b) 128 Points Window STFT

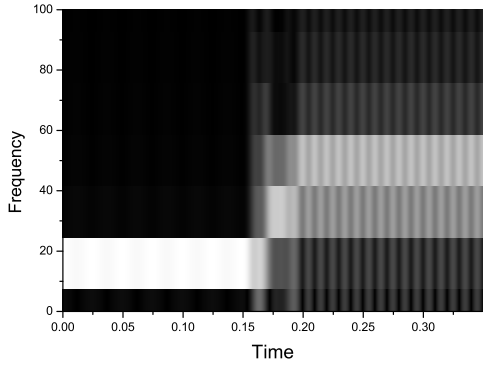

(c) 512 Points Window STFT

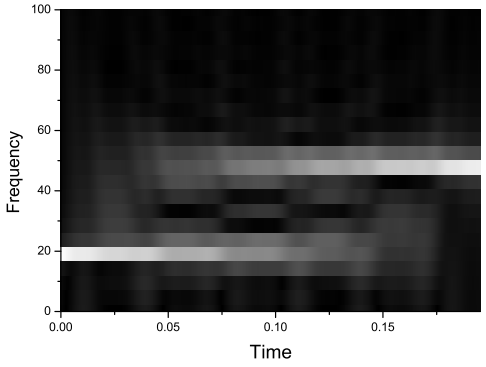

(d) 950 Points Window STFT

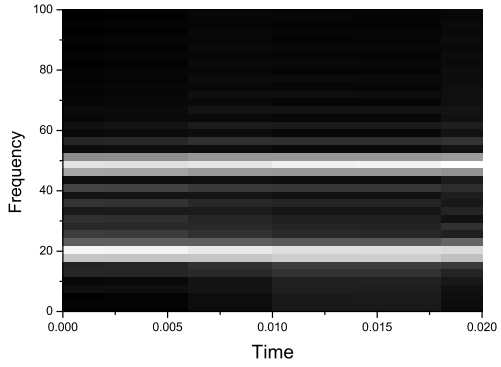

Figure 3.5: Different Frequency–Time Resolutions for STFT.

3.4 The Wavelet Transform

As clearly stated in the previous section, it is impossible to break the uncertainty principle. The wavelet transform gives an alternatively way of dealing with the multiresolution problems. While the short-time Fourier transform has a fixed window function which fixes the time and frequency resolution, wavelet transform uses window function, also called mother wavelet, with variable window size. Within the uncertainty principle framework, it is possible to acquire any frequency–time resolution using wavelet transform. Therefore, it is possible to have good time resolution and poor frequency resolution at high frequencies and good frequency resolution and poor time resolution at low frequencies. This is the reason that this multiresolution analysis tool is so useful as a replacement of STFT.

3.4.1 The Continuous Wavelet Transform (CWT)

The continuous wavelet transform is given by

$$W_\psi f(a,b) = \int_R f(t)\psi_{a,b}(t)dt \tag{3.16}$$

In the expression, $f(t)$ is the original signal to be transformed, a is the parameter of scale, and b is the parameter of location. $\psi(t)$ is called the mother wavelet. $\psi_{a,b}(t)$ is given by

$$\psi_{a,b}(t) = \frac{1}{\sqrt{a}}\psi\left(\frac{t-b}{a}\right). \tag{3.17}$$

The inverse wavelet transform is given by

$$f(t) = \frac{1}{C_\psi}\int_{-\infty}^{+\infty}\int_{-\infty}^{+\infty} W_{\psi,f}(a,b)\psi_{a,b}(t)\frac{dbda}{a^2}, \tag{3.18}$$

where the constant C_ψ is expressed as

$$C_\psi = \int_{-\infty}^{+\infty} \frac{\left|\hat{\psi}(\omega)\right|^2}{|\omega|} d\omega. \tag{3.19}$$

In this expression, $\hat{\psi}(\omega)$ is the Fourier transform of $\psi(t)$.

One important difference can be identified by comparing the definition of the wavelet transform Eq. (3.16) with the definition of the short-time Fourier transform Eq. (3.10). While the STFT has the exponential term $e^{-i\omega t}$ from Fourier transform, there is no Fourier transform inside wavelet transform, and wavelet transform does not transform a signal from physical domain to frequency domain. In fact, the only thing that the wavelet transform does is to apply various dilated and translated variations of the mother wavelet, or window function, to the input function $f(t)$. With proper design of the mother wavelet, the wavelet transform can extract the physical information at different scales from a signal.

There are certain criteria that a mother wavelet needs to meet. For example, in order for the successful reconstruction of wavelet, the constant C_ψ, which depends only on the wavelet itself according to Eq. (3.19), has to meet the admissibility condition:

$$C_\psi = \int_{-\infty}^{+\infty} \frac{\left|\hat{\psi}(\omega)\right|^2}{|\omega|} d\omega < \infty \tag{3.20}$$

As $\hat{\psi}(\omega)$ is the Fourier transform of $\psi(t)$, $\hat{\psi}(\omega)$ has to be zero to meet the admissibility condition. Substituting back into the definition of Fourier transform Eq. (3.1) gives

$$\int \psi(t) dt = 0 \tag{3.21}$$

There are other criteria, and constructing a wavelet function is a challenging task [12, 5]. Some commonly used wavelet functions are shown in Figure 3.6. They include 1) the Haar wavelet, 2) the Shannon wavelet, 3) the Mexican hat wavelet, and 4) the Daubechies wavelet.

(a) Haar wavelet

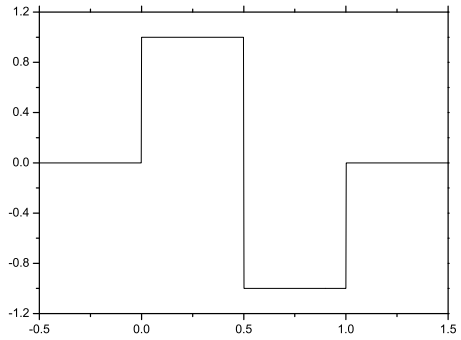

(b) Shannon wavelet

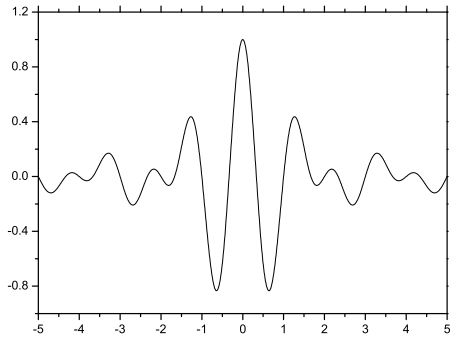

(c) Mexican hat wavelet

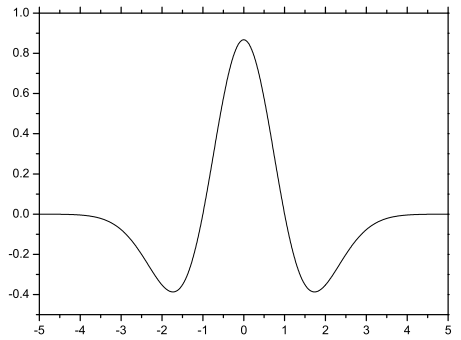

(d) Daubechies wavelet (db4)

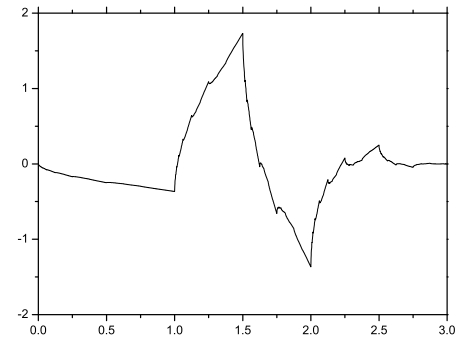

Figure 3.6: Different common mother wavelets.

Now we illustrate the implementation of the wavelet transform using the example

problem previously discussed

$$x = \begin{cases} 2\cos(2\pi \cdot 20t) & \text{when } 0 \leq t \leq 0.2 \\ 2\cos(2\pi \cdot 50t) & \text{when } 0.2 < t \leq 0.4 \\ 0 & \text{elsewhere} \end{cases} \tag{3.22}$$

Computing the continuous wavelet transform according to Eq. (3.16) is to calculate the wavelet coefficients for every $[a, b]$ combination while every time there is a small increment for a or b. This is discretized continuous wavelet transform; and it is different from the discrete wavelet transform, which will be discussed later.

The continuous wavelet transform of Eq. (3.22) using the Meyer wavelet is shown in Figure 3.7. The x-axis represents the translation within physical space, or b in the wavelet transform definition Eq. (3.16), and y-axis represents scales, or a in Eq. (3.16). a is proportional to physical domain coordinate; but, unlike time–frequency coordinate in STFT, b is a parameter of scale. The scale in wavelet transform is the same as the scale in a map; and it can be treated as the inverse of the frequency. Accordingly, large scales represent low frequencies and *vice versa*. As for the image itself, the light regions represent large wavelet coefficients and the dark regions are large negative wavelet coefficients, while the gray regions show the wavelet coefficients around zero. Note that only the gray regions, which have the wavelet coefficients around zero, represent that there is no information at this time and scale, while the rest, whether it is large positive wavelet coefficients or large negative wavelet coefficients show information at that time-scale.

Comparing with the plot of the function shown in Figure 3.2a, it is easy to identify that both figures have the same number of waves, either in the 20Hz zone or the 50Hz zone; but in Figure 3.7, the waves at the two frequencies lay in different scale zone and

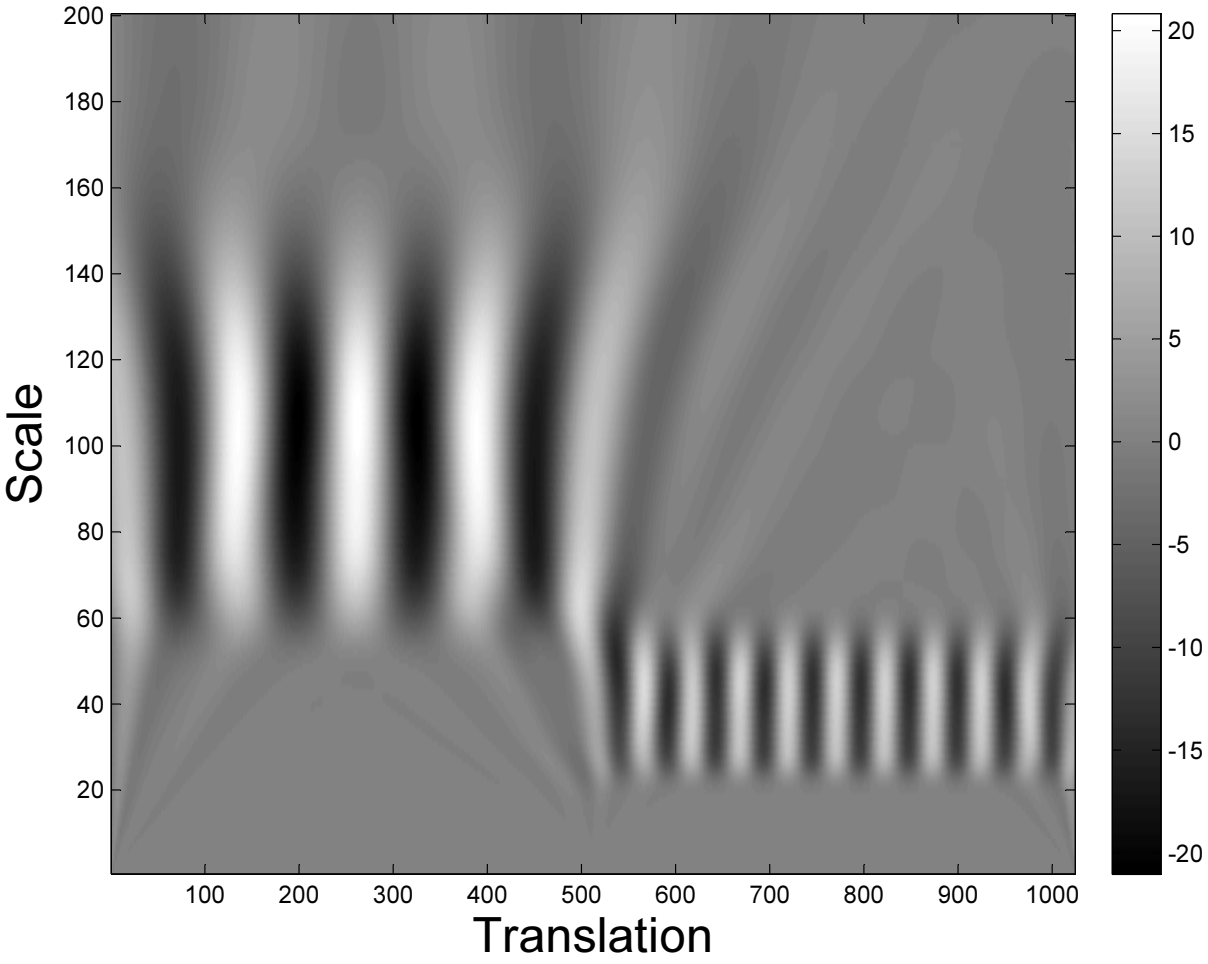

Figure 3.7: Continuous Wavelet Transform for Eq. (3.22)

they do not stay in just one single scale number. Instead, they span a range of scale numbers. The lower frequency part (left half of the graph) has a larger span in the scale coordinate than the higher frequency part (right half of the graph). As scale is related with the inverse of frequency, the high scale part represents a good frequency resolution and the low scale part represents a poor frequency resolution.

3.4.2 The Discrete Wavelet Transform and Fast Wavelet Transform

The continuous wavelet transform gives the capability of multiresolution analysis; but, it also gives redundant information as it is a function of two variables a and b. Therefore, transforms a one-dimensional signal into a two-dimensional space and its calculation may result in extra computational time and storage space. The discrete wavelet transform (DWT) and the fast wavelet transform (FWT) were developed as an alternative of CWT.

Instead of calculating wavelet coefficients for all $[a_i, b_j]$ combinations, only a selected number of $[a_i, b_j]$ pairs is calculated in DWT. By selecting $a = 2^m$ and $b = n2^m$, and the mother wavelet can be expressed as

$$\psi_{m,n}(t) = 2^{-\frac{m}{2}} \psi \left(2^{-m}t - n\right) \tag{3.23}$$

Instead of scale parameter a in CWT, the parameter of level m is used in DWT. In fact, using a coordinate based on m instead of a is the same as a 2 based log scale based on a. The grid lattice of DWT is shown in Figure 3.8. The adjacent levels have a factor of 2 for physical domain resolution, with different levels having a different number of wavelet coefficients. The time–frequency resolution for DWT is often shown as Figure 3.9. It shows time-frequency resolution for 4 levels of wavelet coefficients. As frequency doubles,

the frequency resolution is halved and the time resolution is doubled; while the area of every rectangular box is the same, which is a result of the uncertainty principle.

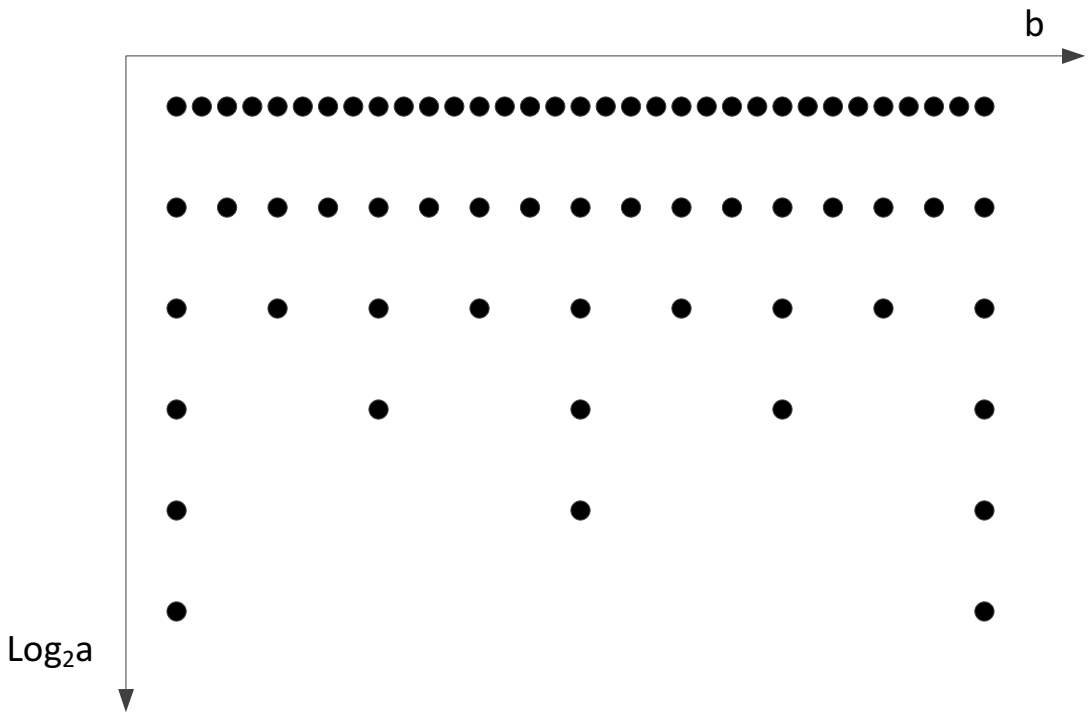

Figure 3.8: Grid Lattice for Discrete Wavelet Transform

The fast wavelet transform (FWT) is a faster way of calculating DWT. It produces exactly the same wavelet coefficients as DWT. In engineering perspective, it is the same as the relationship between Discrete Fourier transform and Fast Fourier transform, DWT and FWT are used interchangeably for most of the cases and of course throughout this dissertation.

Instead of using a wavelet transform definition Eq. (3.16) as well as the discretization formula $a = 2^m$ and $b = n2^m$ to calculate the discrete wavelet coefficients, low-pass and high-pass filters are used to separate the low-frequency and high-frequency information

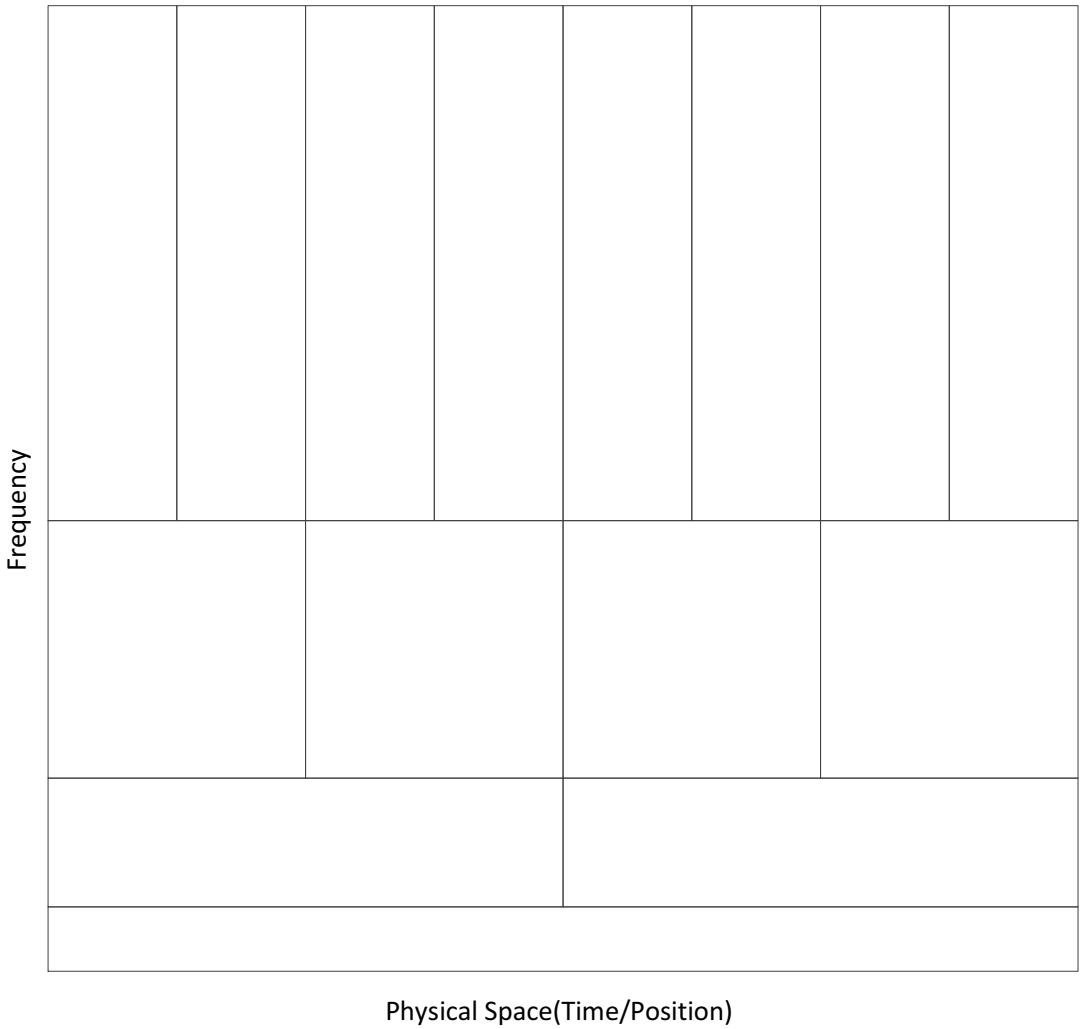

Figure 3.9: Physical Space–Frequency Resolution Representation

out of the original signal. The entire FWT process is shown in Figure 3.10. The signal s is convolved with a low-pass filter and then after the downsampling process gives the approximate wavelet coefficients cA. This information correspond to the low-frequency information. Similarly, convolving s with a high-pass filter and then after the downsampling process gives the detailed wavelet coefficients or high frequency information cD. There are two operations involved in the FWT process, convolution and downsampling, and here are some explanations about them.

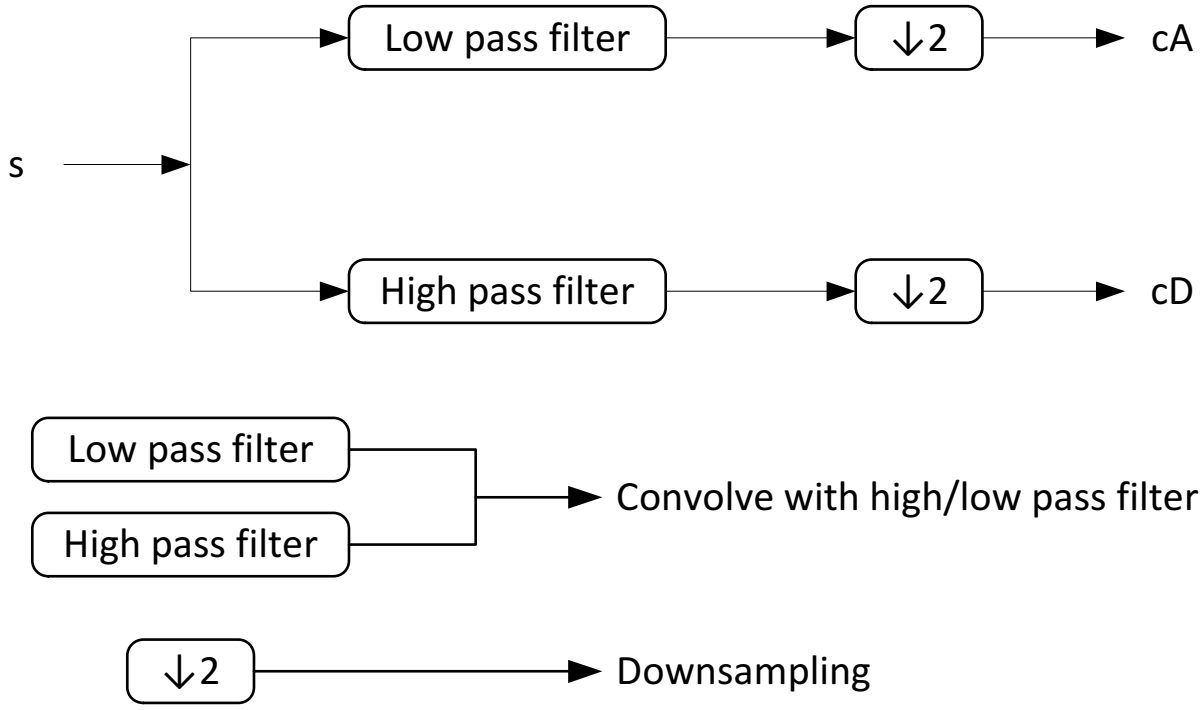

Figure 3.10: Fast wavelet transform process

1. **Convolution**

   Convolution between two series $[a_1, a_2, \cdots, a_n]$ and $[b_1, b_2, \cdots, b_n]$ is the same as

multiplication between two polynomials with coefficients of $[a_1, a_2, \cdots, a_n]$ and $[b_1, b_2, \cdots, b_n]$. So convolution between $[1, 2]$ and $[2, 1]$ gives result of $[2, 4, 3]$.

$$(x + 2) \cdot (2x + 1) = 2x^2 + 4x + 3 \tag{3.24}$$

2. **Downsampling**

   Downsampling is achieved by keeping the even indexed elements while discarding the odd indexed elements. For example, downsampling the signal $[s_1, s_2, \cdots, s_{10}]$ gives $[s_2, s_4, s_6, s_8, s_{10}]$ as shown in Figure 3.11.

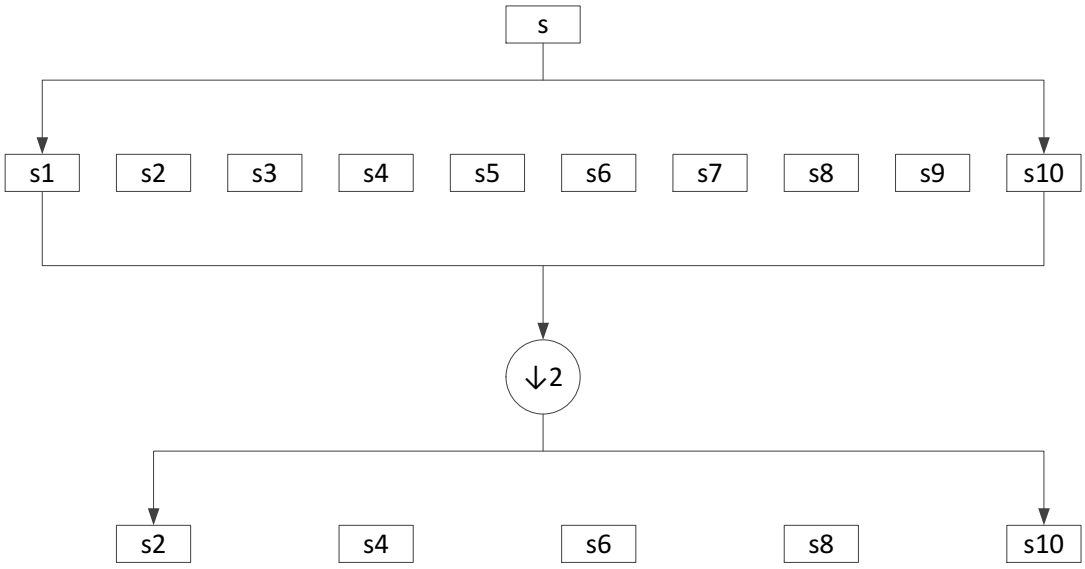

Figure 3.11: Downsampling Process

The DWT of the previous example Eq. (3.22) is shown in Figure 3.12, it is still very clear that there are two frequencies showing up, one at level 5, and the other one shows up at level 6 and 7, and these two frequencies correspond with $50Hz$ and $20Hz$. Also,

comparing the DWT Figure 3.12 with CWT Figure 3.7, level 5 in DWT should correspond with scale of $2^5 = 32$, and level 6 and 7 are the scale of 64 and 128, respectively, and these justifications coincide with the graph.

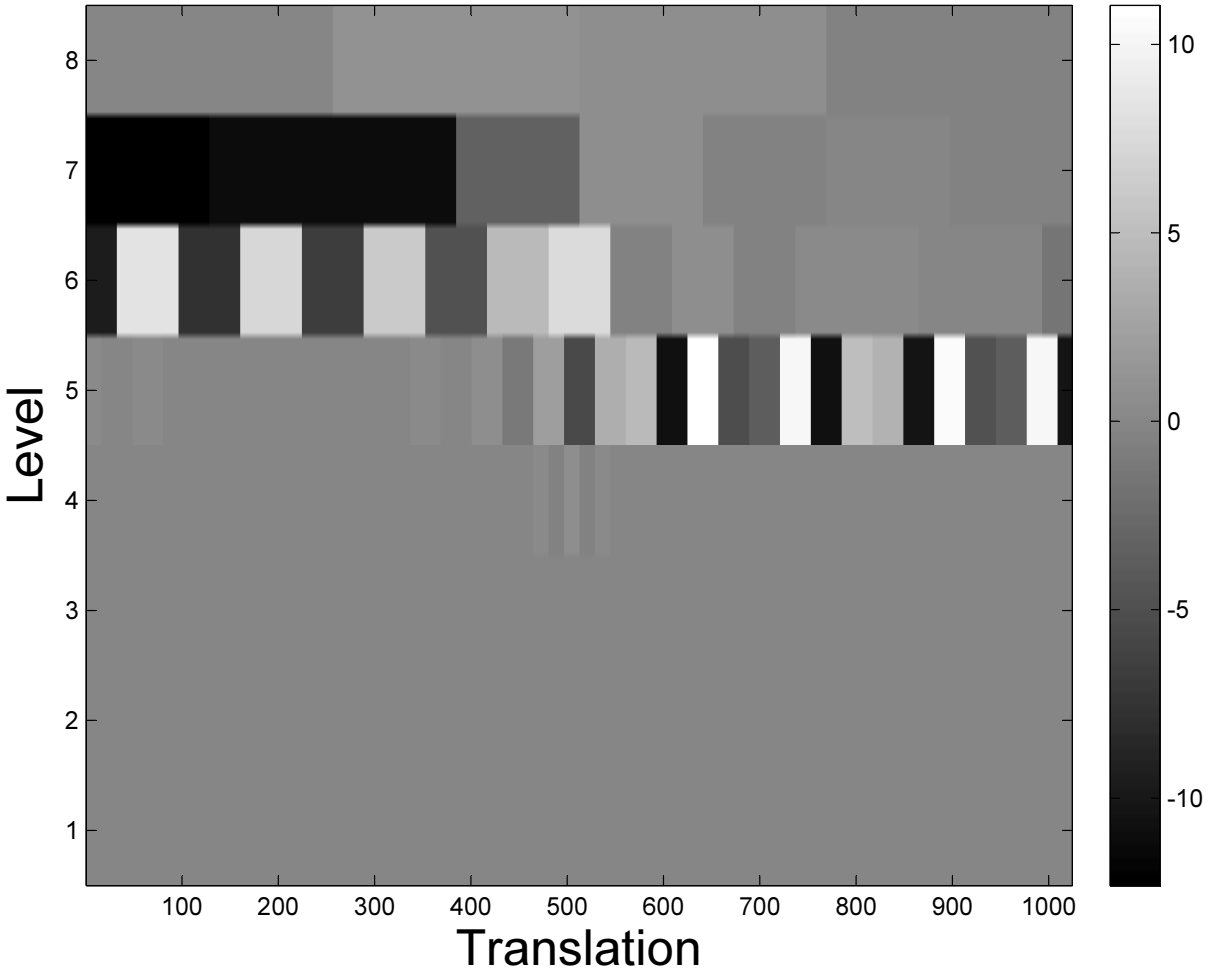

Figure 3.12: Discrete Wavelet Transform for Eq. (3.22)

3.4.3 Wavelet Decomposition and Fast Wavelet Transform Result Representation

In practice, wavelet decomposition is often used; wavelet decomposition will apply FWT several times to the signal. The discrete wavelet transform result Figure 3.12 is a result of wavelet decomposition. After applying FWT to the signal, two sets of wavelet coefficients are obtained, the approximate coefficients cA and detailed coefficients cD, and then FWT is again applied to cA, giving a larger scale set of approximate coefficients as well as detailed coefficients, and this process is repeated for several times until a certain number of level is reached. Showing in Figure 3.13, for example, a signal with frequency from 0 to 200Hz, and first level of wavelet decomposition gives two sets of coefficients — $cD1$ with frequency domain from 100 to 200Hz and $cA1$ with frequency domain from 0 to 100Hz. $cA1$ is again decomposed, resulting in $cD2$ and $cA2$, which have frequency domain of $50 \sim 100Hz$ and $0 \sim 50Hz$, and so on. Figure 3.13 shows a 3 level wavelet decomposition and in most cases, the result of the wavelet decomposition is represented as array arranged as $[cA3, cD3, cD2, cD1]$. Arranging from low frequency to high frequency or large scale to fine scale, these coefficients covers the whole frequency(scale) range, and it has no redundant information as CWT and the original signal can be fully reconstructed by using these coefficients only.

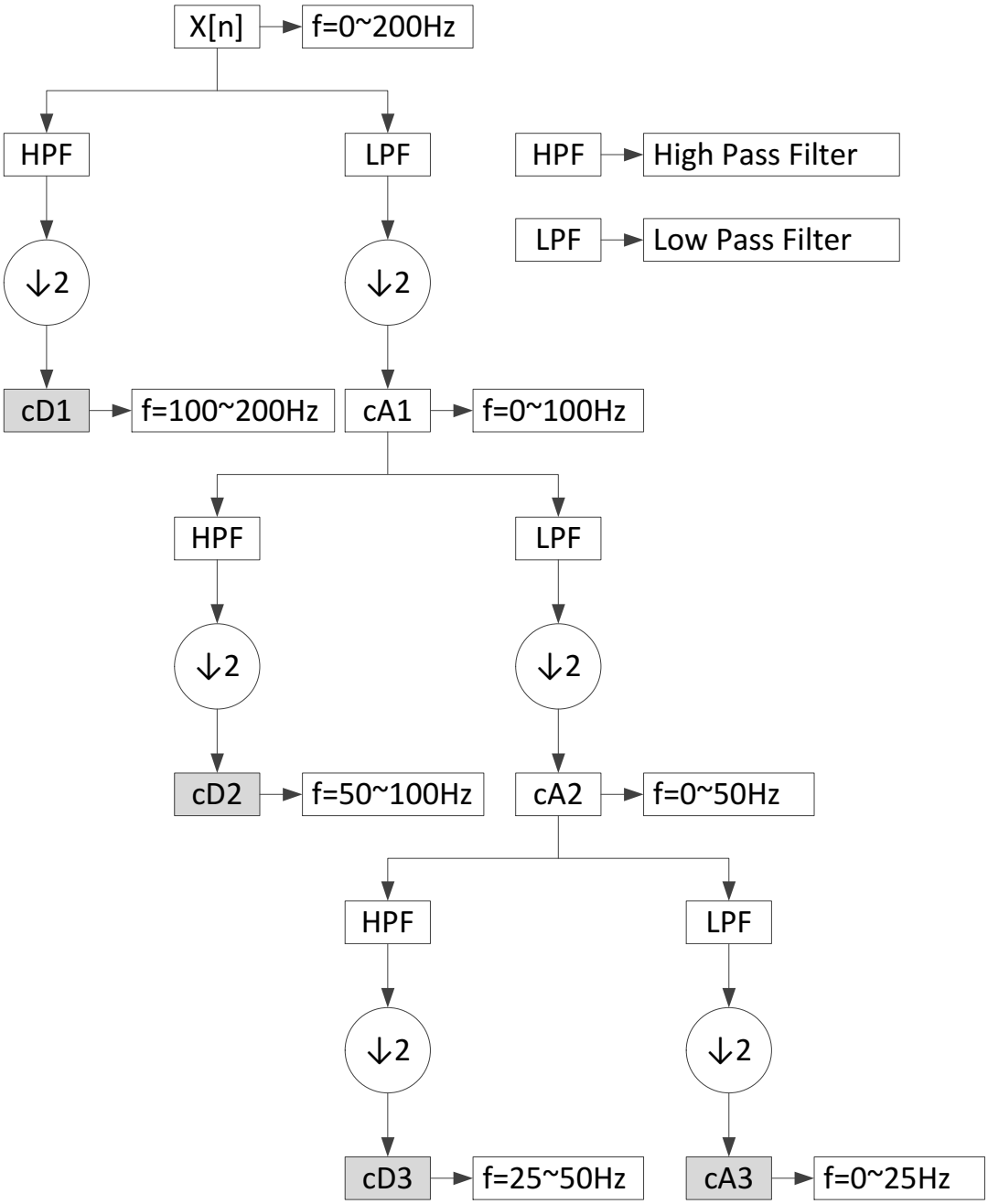

Figure 3.13: Process for a Complete 3 Level Fast Wavelet Decomposition

3.4.4 The Wavelet Spectrum

The discrete wavelet spectrum is calculated as the summation of the wavelet coefficients square at a certain scale. Mathematically, it is defined as

$$E(a) = \sum_i W(a, b_i)^2, \tag{3.25}$$

where $W(a, b_i)$ is the wavelet coefficient at level a and location b_i.

The wavelet energy is different from the Fourier energy. The Fourier energy is a representation of the energy contained at one certain frequency, while the wavelet energy is a description of the energy contained at a certain scale. The wavelet spectrum is also related with Fourier spectrum by [18]

$$E(a) = \sum_i e(\omega_i)|\hat{\psi}(a\omega_i)|^2, \tag{3.26}$$

if the Fourier energy spectrum is denoted as $e(\omega) = |\hat{f}(\omega)|^2$. $\hat{f}$ is the Fourier coefficient of function f, ψ is the mother wavelet. The relationship Eq. (3.26) also gives another information about the wavelet energy spectrum: wavelet energy spectrum corresponds to the Fourier energy spectrum smoothed by the wavelet spectrum at each scale [18].

The smoothness of wavelet energy spectrum is important for the current implementation. Because of the limitation of the computational power, only a limited resolution is adopted, which is far away from generating a smooth Fourier spectrum. The wavelet spectrum is used instead of Fourier spectrum to give a more robust implementation.

3.4.5 Computational Cost

It is important to address the computation cost of the wavelet transform. The fast wavelet transform, which is used for all wavelet transform implementation in this dissertation, has a computational complexity of $O(N)$. The computational cost of wavelet transform is linear with the number of data points. For comparison, fast Fourier transform has a computational complexity of $O(N \log N)$. The computational cost of wavelet transform is less than that of FFT, which enables the wavelet implementation without adding any noticeable time cost.

3.5 More Discussion about the Wavelet

To give more intuitive illustration of wavelet transform, here, a simple wavelet transform with Haar wavelet is given. Haar wavelet is the simplest wavelet among all kinds of wavelets, and some of its properties are not desired in real wavelet transform application, for example, the discontinuity of Haar wavelet will cause a lot of problems in real applications, but for illustrative purpose, it is great because it is the easiest wavelet.

The mother wavelet $\psi(t)$ of Haar wavelet is shown as Figure 3.14 or mathematically described as

$$\psi(t) = \begin{cases} 1 & 0 \leq t < 1/2, \\ -1 & 1/2 \leq t < 1, \\ 0 & \text{otherwise.} \end{cases} \tag{3.27}$$

Low pass filter of Haar wavelet is given as $[1/\sqrt{2}, 1/\sqrt{2}]$ or $[0.7071, 0.7071]$, and high pass filter of Haar wavelet is given as $[-1/\sqrt{2}, 1/\sqrt{2}]$ or $[-0.7071, 0.7071]$.

For signal $[a_1, a_2, \cdots, a_n]$, the convolution with filters are the same as polynomial

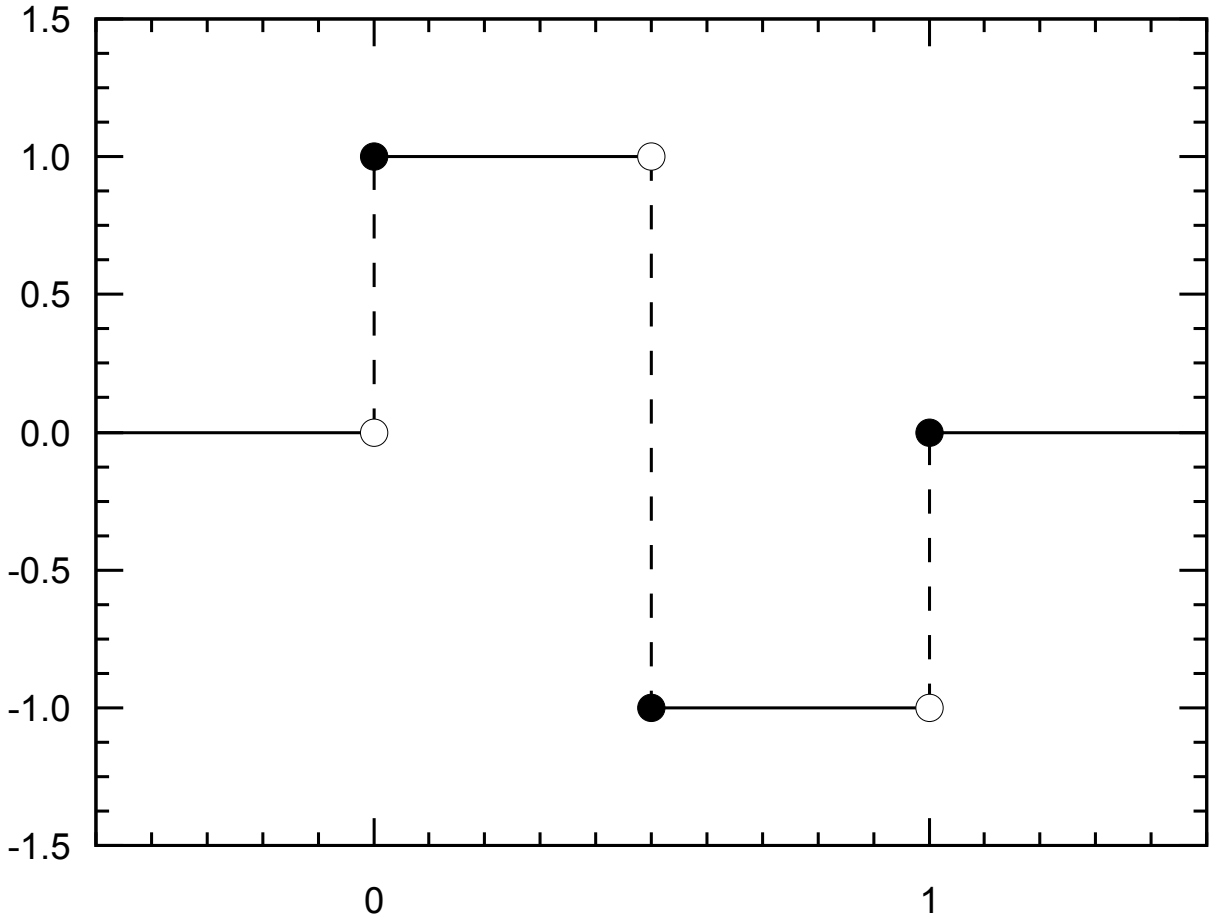

Figure 3.14: The Haar mother wavelet.

multiplication and is calculated as

$$\begin{aligned}
&\left(\sum_{i=1}^{i=n} a_i x^{i-1}\right)\left(\frac{1}{\sqrt{2}}x+\frac{1}{\sqrt{2}}\right)=\frac{1}{\sqrt{2}}a_n x^n+\sum_{i=1}^{i=n-1}\left(\frac{a_{i+1}}{\sqrt{2}}+\frac{a_i}{\sqrt{2}}\right)x^i+\frac{a_1}{\sqrt{2}}\\
&\left(\sum_{i=1}^{i=n} a_i x^{i-1}\right)\left(-\frac{1}{\sqrt{2}}x+\frac{1}{\sqrt{2}}\right)=-\frac{1}{\sqrt{2}}a_n x^n+\sum_{i=1}^{i=n-1}\left(-\frac{a_{i+1}}{\sqrt{2}}+\frac{a_i}{\sqrt{2}}\right)x^i+\frac{a_1}{\sqrt{2}}
\end{aligned} \tag{3.28}$$

Despite the boundary values which may require further treatments in real problem, for Haar wavelet, approximate coefficients are obtained by averaging neighboring points coefficients and detailed coefficients are the difference between neighboring points coefficients with normalizing coefficient $\sqrt{2}$. So, for a constant value signal, like $a = [1, 1, \cdots, 1]$, wavelet coefficients are $[\sqrt{2}, \sqrt{2}, \cdots, \sqrt{2}]$ for approximate coefficients and $[0, 0, \cdots, 0]$ for detailed coefficients, which means that all the energy is concentrated in low frequency region with zero energy in high frequency region. On the other hand, the alternating signal $a = [1, -1, 1, -1, \cdots, 1, -1]$ will have approximate coefficients of $[0, 0, \cdots, 0]$ and detailed coefficients $[-2\sqrt{2}, -2\sqrt{2}, \cdots, -2\sqrt{2}]$, which means that all the energy is concentrated in the high frequency region with no energy in low frequency region.

Chapter 4

Wavelet-Based Implementation and Results

4.1 Introduction and Objectives

As discussed in the previous chapter, the wavelet transform has the ability for multi-resolution analysis; and this ability can be used in turbulence simulation. Farge [18] first discussed the potential applications of the wavelet transform in turbulence, which include energy decomposition and turbulence diagnostics. Mouri [57] showed that the wavelet transform exhibits small scale enhancement of (1) the spatial fluctuation, (2) the correlation in space between adjacent scales and (3) the correlation in space between different directions. Farge [19] utilized the wavelet transform to extract coherent vortices from three-dimensional turbulent flows; and the results showed that 3% of wavelet coefficients can retain 98.9% of the total turbulent energy without losing the $k^{-\frac{5}{3}}$ spectrum. Frantziskonis [20] applied the wavelet-based approach called the compound wavelet matrix (CWM) to solve diffusion-reaction problems. The CWM approach used couples the

fine solution generated by kinetic Monte Carlo method stochastically and the coarse solution generated by solving reaction and diffusion equations deterministically. Based on the CWM method, the dynamic CWM (dCMW) method was proposed [58]. The dCWM method models the time evolution of multiscale and/or multiphysics systems via dynamically updating the compounded wavelet matrix, giving more accuracy and flexibility.

In this chapter, the downscaling process using the wavelet-based compounding approach is presented first. By applying the wavelet transform to both LES and ODT, the LES large scale velocity components and small scale ODT velocity components with scales up to LES filter size are coupled. New velocity profiles are generated and feed back into the ODT.

The second application of the wavelet transform, the spatial filtering of combustion features, is discussed. The combustion features, which are represented by progress variable here, are commonly used to track flames, ignition and extinction. Although the approach can be applied to other combustion features. Chemical reaction equations are not solved in LES for the current research because no portion of the filtered chemical source term can be resolved in LES typically [64]. Flame detection and visualization require the filtering of the progress variable into LES lattice because they cannot be visualized easily under the current ODT grid formulation. The wavelet transform is used to extract progress variable information of the premixed flames above the LES filter scale from ODT.

The last application of the wavelet transform is the wavelet spectra based ODT parameter determination. The ODT parameter that governs the turbulent intensity is crucial for the LES-ODT coupling. For a proper ODT subgrid model implementation, the energy spectrum of ODT should match the energy spectrum of LES. Wavelet spectra of LES and ODT are used and the ODT parameter is adjusted to match the slopes between LES wavelet energy spectra and ODT wavelet energy spectra at the compounding scale,

or LES filter scale.

Finally in this chapter, the results of the three wavelet transform applications are presented for a premixed non-homogeneous decaying isotropic turbulence case. Different initial conditions and run conditions are verified for these implementations.

4.2 Wavelet-Based Compounding

Multiscale schemes for transferring information from large to small scales are typically based on interpolation techniques [8]. Such schemes add additional small-scale features to the field; and even worse, the artificially added fine scale features can have influence to the large scale features. As a superior alternative for the interpolation method, a wavelet-based compounding approach is established to couple two solutions that consist of different scale information, like LES and ODT in the LES-ODT formulation, while obtaining large scale information from LES and small scale information from ODT. Comparing with the interpolation method, the wavelet-based compounding has additional advantages:

1. No artificial information is added at any scale level. While interpolation add additional data points in between, wavelet-based compounding obtains large scale wavelet coefficients from LES and small scale wavelet coefficients from ODT without adding any artificial information.

2. The compounded velocity field is more compatible with ODT. Since ODT is a subgrid closure model for LES in LES-ODT formulation and LES has no information for subgrid scale, it is important for ODT to develop its own subgrid statistics without adding information manually.

3. Wavelet coefficients give important information for both scale and location, and

Table 4.1: Relevant parameters for example problem

LES length (grid points)	16
ODT length (grid points)	256
Compounding level	4
wavelet	Daubechies 4

these wavelet coefficients can be used for other applications like the following ODT parameter determination without re-calculating.

4.2.1 Algorithm and Procedure

The algorithm will be shown with one compounding example. This example is extracted from the real LES-ODT compounding case; but the initial condition and most of the running conditions (Re, Pr for example) are not shown here because they are not relevant to this example. The example problem here is showing one snapshot right before and right after compounding. Some relevant parameters are described in Table 4.1.

In this example problem, LES has 16 data points in each direction and each ODT domain has 256 data points. The LES domain coincides with the ODT domain so they have a smallest resolution difference of 16. A 4 level compounding is applied, since every level will decrease spatial resolution by a factor of 2 thus a 4 level compounding in this case decreases the ODT resolution by 16 and it is the same as the LES resolution. After 4 level decomposition, all LES information can be used in the compounding to replace ODT large scale wavelet coefficients. The procedures are shown in Figure 4.1 as well as following:

1. **Coarse solution interpolation**

   LES and ODT solutions coincide with each other in the physical domain with different resolution and different number of data points. In order to get the same number of wavelet coefficients to perform compounding, LES solution should be interpolated into the same resolution as ODT solution. In this example, LES is interpolated from 16 grid points to 256 grid points. Denote u_{LES} as the LES solution and $u_{LES-interp}$ as the interpolated LES solution.

2. **Wavelet decomposition**

   Wavelet decomposition is performed over fine and interpolated coarse solutions until a certain number of wavelet coefficients is left or until a certain number of wavelet decomposition is achieved. In LES-ODT compounding, information from all scales that LES possess is used, so the same will be done for this example problem. LES has 16 grid points and ODT has 256 grid points, so $\log_2 256 - \log_2 16 = 4$ levels of wavelet decomposition is applied which is mentioned before. The 4 level decomposition is done for both interpolated LES and ODT, so information from different scales for both LES and ODT is acquired. In Figure 4.1, CD1 indicates detailed coefficients for 1st level decomposition, CD2 for 2nd level detailed wavelet coefficients and CA4 indicates coefficients of approximation or large scale coefficients. If C_{LES} represents the wavelet coefficients of the interpolated LES arranged as $(CA4, CD4, CD3, CD2, CD1)$ and C_{ODT} represents the wavelet coefficients of the ODT velocity with the same arrangement.

$$C_{LES} = \mathrm{WT}(u_{LES-interp}) \tag{4.1}$$

$$C_{ODT} = \mathrm{WT}(u_{ODT}) \tag{4.2}$$

WT represent the 4 level wavelet decomposition process.

3. **Selection and identification of overlapping scales**

   Overlapping scales refer to the common or equivalent scales between two solutions. After interpolation, LES solutions have the same smallest scale as ODT solution, although it does not contain any physical information. In this example problem, the wavelet coefficients of the 4th level, the level for the 4th wavelet decomposition is the common scale information between LES and ODT, thus the 4th level is the overlapping scale. As in Figure 4.1, CA4 coefficients are identified as overlapping scale. In the wavelet coefficient array C_{LES} and C_{ODT}, the 1st to the 16th wavelet coefficients represent the common scales.

4. **Substitution**

   For wavelet coefficients other than the overlapping scales, the wavelet coefficients of ODT are used to substitute the wavelet coefficients of interpolated LES. In this example problem, with a total 256 wavelet coefficients for both interpolated LES and ODT, 16 wavelet coefficients from interpolated LES are used; and the rest 240 smaller scale wavelet coefficients from interpolated LES are replaced by corresponding ODT wavelet coefficients. In Figure 4.1, the CA4 part is obtained from LES and the rest, CD1, CD2, CD3 and CD4 are obtained from ODT. This can be expressed as

$$C_{compound} = \begin{cases} C_{LES}(i) & \text{if } i \leq 16 \\ C_{ODT}(i) & \text{if } i > 16 \end{cases}, \tag{4.3}$$

   where i represents the index of the wavelet coefficient arrays. $C_{compound}$ is the wavelet coefficients of the compounded velocity.

5. **Reconstruction**

   The inverse wavelet transform is applied to the new LES wavelet coefficients to get the hybrid solution that has both large scale information from LES solution and small scale information from ODT solution. Similar to the wavelet decomposition steps, 4 levels of inverse wavelet transform are needed in order for the reconstruction.

$$u_{compound} = \text{iWT}(C_{compound}) \tag{4.4}$$

   iWT is the 4 level inverse wavelet transform process; $u_{compound}$ is the desired velocity after the compounding.

4.2.2 Implementation

The above algorithm is for corresponding one LES line and one ODT domain, and for proper coupling between LES and ODT. The procedure stated above needs to be applied for every corresponding LES line–ODT domain pair. There should be $nx \cdot ny + ny \cdot nz + nz \cdot nx$ times of such compounding, where nx, ny and nz are the number of LES grid points in x direction, y direction and z direction, respectively. It is the same as the number of ODT domains. Therefore, for every ODT domain, there is a corresponding LES line to couple with, so every ODT domain can have information passing from LES.

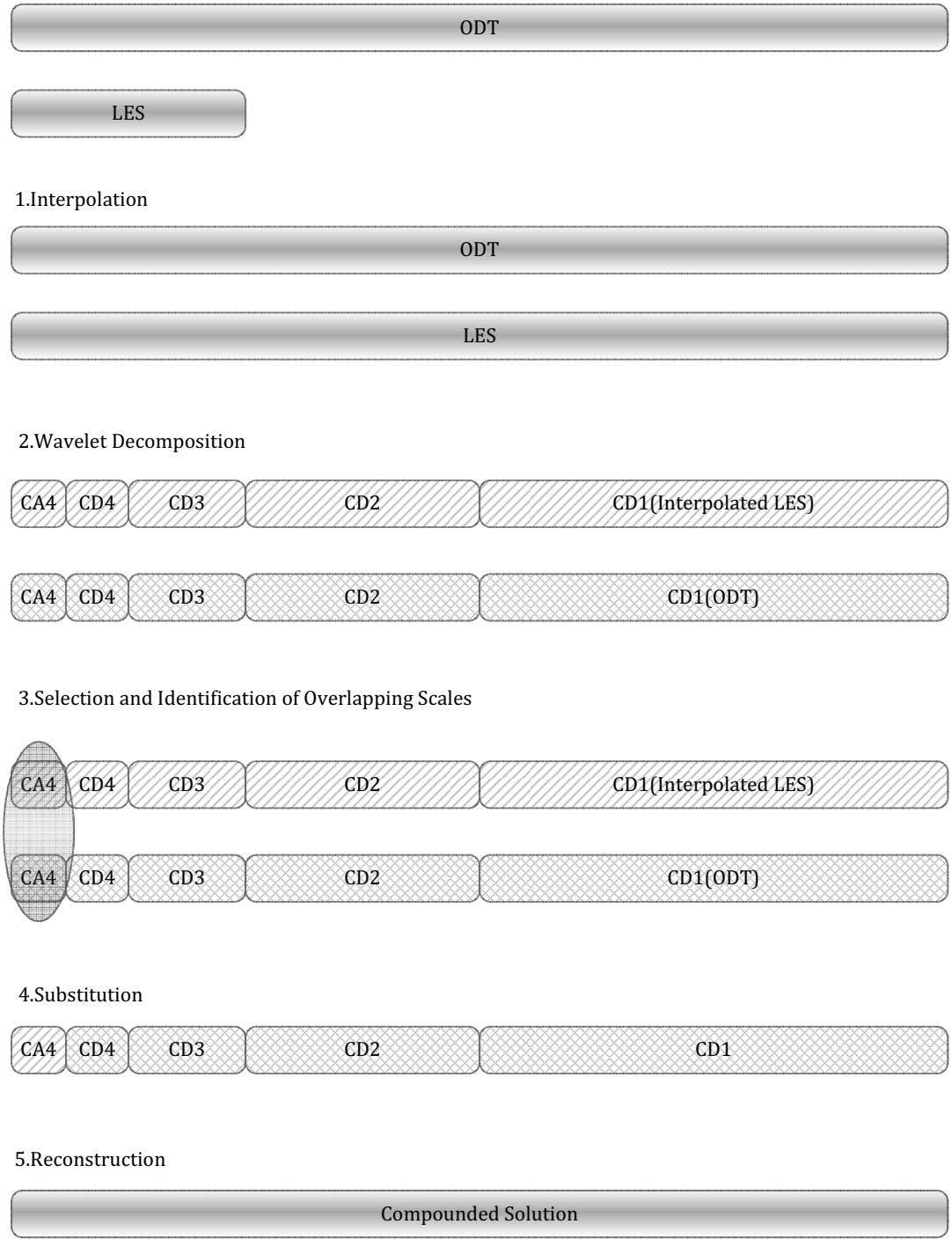

Figure 4.1: Compounding process

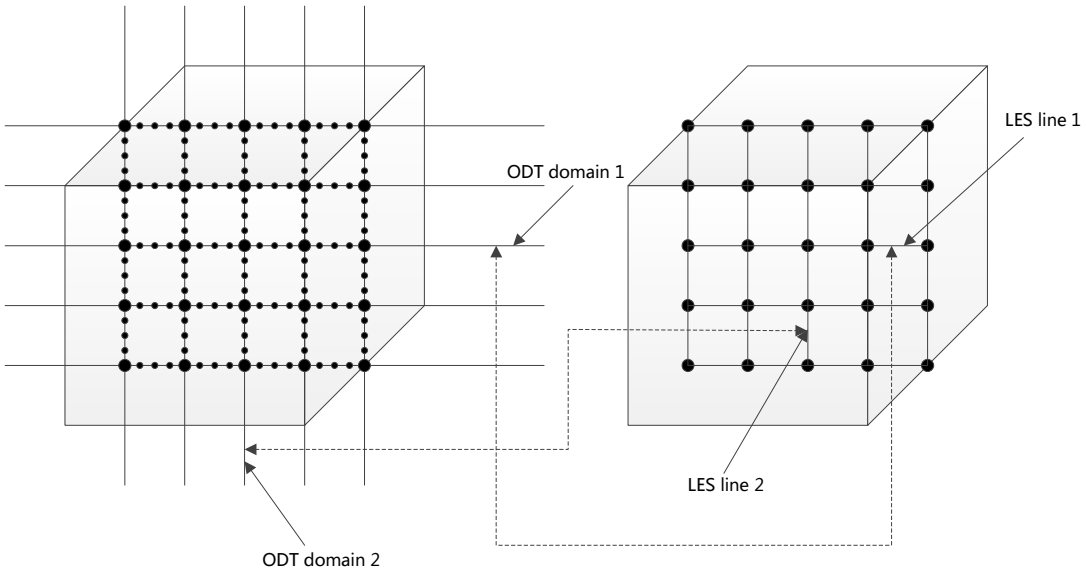

Figure 4.2: Illustration of Compounding Pairs

4.3 Wavelet-based spatial filtering of combustion features

In the LES-ODT formulation, ODT takes consideration of chemical reaction source term while LES does not; so all combustion features lie within ODT. As ODT grid formulation and layout are not uniform and even are overlapping, it is hard to detect or visualize combustion features within ODT directly, and filtering ODT result is necessary. Traditionally, a filtering process is achieved as

$$\bar{f}(x) = \int f(x')G(x - x')dx', \tag{4.5}$$

where the $\bar{f}$ is the filtered function, f is the original function, and G is the filter function. In the formulation of Cao & Echekki [9], a box filter is used for filtering the ODT information to LES grid. Under the influence of this filtering scheme, large scale features are

not necessary preserved. The wavelet transform has the ability of extracting information from certain scales; thus the separation of scales preserves features of every scale under consideration. In the wavelet-based spatial filtering approach, by using the scale separation feature of the wavelet transform, the information under the LES filter size can be eliminated by zeroing out the wavelet coefficients of the small scales without having any influence of large scale.

The progress variable is one of the most important parameters for combustion and it is widely used in many combustion models like the flamelet model and the conditional moment closure model. The progress variable is used here to track the combustion but any other combustion features can be filtered by using this approach. The iso-surface of progress variable is used to visualize the flame surface. Filtering the progress variable of ODT into LES lattice gives the combustion status of the simulation above filter scale.

4.3.1 Algorithm and Procedure

Take the LES-ODT formulation grid set for example as shown in Table 4.2. LES has 16 grid points and ODT has 256 grid points in a given direction. In order to filter ODT solution to the LES grid, ODT has to be filtered into the same scale as LES. Since the discrete wavelet transform increases the scale by 2 every time, 4 discrete wavelet transforms are needed for every ODT domain under the condition of these parameters. Figure 4.3 as well as the explanation of the procedure is shown as following:

1. **Wavelet decomposition**

   Wavelet decomposition is performed over ODT domains. This introduces the application of a multi-level wavelet transform for ODT domains until a certain number of wavelet coefficients left or until a certain level of wavelet decomposition is

Table 4.2: Example Parameters

LES length (grid points)	16
ODT length (grid points)	256
wavelet	Daubechies 4

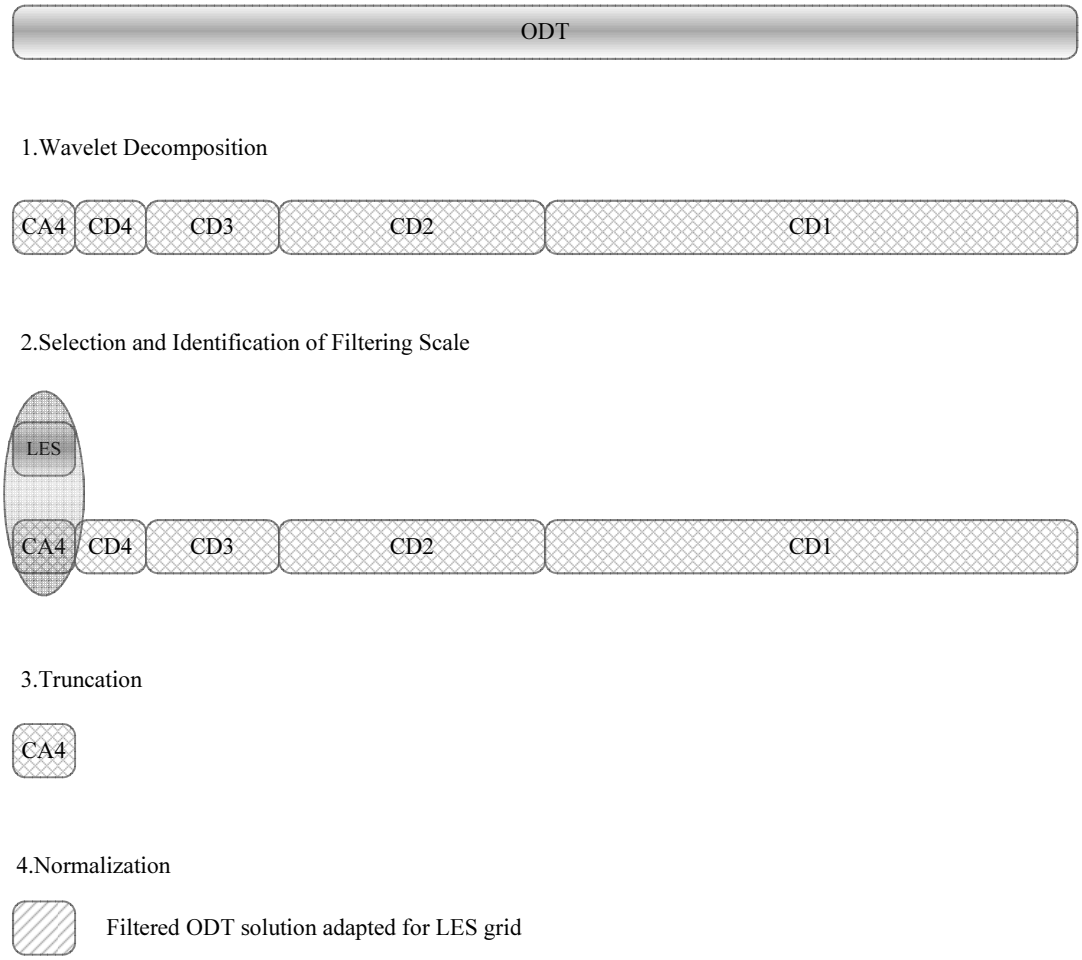

Figure 4.3: Filtering Process

achieved. As explained before, 4 levels of decomposition are required under the condition described in Table 4.2. As shown in Figure 4.3, CD1, CD2, CD3, CD4 and CA4 are wavelet coefficients obtained by apply 4 level wavelet decomposition. The wavelet coefficient array for the ODT progress variable C_c can be arranged as $C_c = (CA4, CD4, CD3, CD2, CD1)$.

2. **Selection and identification of the filtering scale**

   The purpose of the filtering process proposed here is to filter ODT solutions into LES grid, and since LES and ODT both span across the whole computational domain, the filtered ODT solution should have the same grid points as LES. In the example problem, 4 levels of wavelet decomposition give 16 coefficients, just the same as the LES grid points, thus these 16 wavelet coefficients are exactly what is wanted. In the example case, $CA4$ is the desired coefficient or the 1st to the 16th element of the wavelet coefficient array C_c.

   As for some more complicated cases with nonuniform grid, LES may not have the same resolution everywhere in the computational domain, and more levels of wavelet decomposition is required. Therefore, the filtering scale may consist of several segments of wavelet coefficients, like CD5, CD6 and CA6. For this example if 6 levels of wavelet decomposition are applied. In such case, CD5, CD6 and CA6 will be identified and selected, and 2 levels of wavelet reconstruction (inverse wavelet transform) are required.

3. **Truncation**

   All wavelet coefficients except the selected wavelet coefficients are truncated. As in Figure 4.3, CD4, CD3, CD2, CD1 are the detailed coefficients which corresponds to small scale information and should be truncated while CA4 is the approximate

coefficients, which corresponds to large scale information and should be kept. The remaining wavelet coefficients can be expressed as

$$C_{filter} = C_c(1 - 16) \tag{4.6}$$

4. **Normalization**

   Wavelet transform normalizes the wavelet coefficients by a factor of $1/\sqrt{a}$ for energy conservation purpose. For the DWT case, the scale increases by a factor of 2; so one scale larger gives the normalization factor of $\sqrt{2}$. In order to get the proper large scale value, normalization by a factor of $\sqrt{a}$, or $1/\sqrt{2}$ in DWT case, is required for each level of wavelet decomposition. In the example problem, 4 levels of decomposition is applied, resulting in a normalization factor of 4.

$$C_{filter} = C_{filter}/4 \tag{4.7}$$

   Due to the locality of the wavelet transform, the normalized wavelet coefficients is used for the filtered progress variable.

4.3.2 Implementation

With filtering done for one ODT domain shown in the above procedure, the whole computational domain will need to be reconstructed by $nx \cdot ny + ny \cdot nz + nz \cdot nx$ ODT domains. Using the grid information in Table 4.2, that would be 768 ODT domains. Every filtered ODT domain has 16 grid points, which is the same as one LES line. For every LES grid point, there are also three ODT nodes that coincide with it: one from x direction ODT domain, one from y direction ODT domain and one from z direction ODT

domain. Averaging the three data points from the three filtered ODT domains gives the final filtering result. The process can be better illustrated with Figure 4.4, taking one node for example, the node shown in the graph has three ODT domains go though it, ODT1, ODT2, ODT3, and the node is marked as Node1 in ODT1, Node2 in ODT2, Node3 in ODT3. After filtering these three ODT domains, each filtered ODT has the same number of data points as corresponding LES line as shown in the middle part of Figure 4.4, then the three values from the corresponding nodes from three ODT domains averages and one filtered value of the computational domain is given. This averaging process is done for every ODT node or LES point.

4.4 Wavelet spectra based ODT parameter determination

The ODT parameter, which governs the turbulent intensity directly, is a presumed constant in the ODT formulation [44]. It may have different value for different types of turbulent combustion flows; but it is mainly an empirical parameter. The wavelet spectra based ODT parameter determination enables the determination of this parameter dynamically in order to match the turbulent intensity between ODT and LES for better coupling. The idea for this determination is based on matching wavelet spectra slopes between LES and ODT at coupling scale. Because the wavelet spectrum is based on scale rather than frequency for Fourier spectrum, the wavelet transform is the ideal tool for implementing the matching at a certain scale.

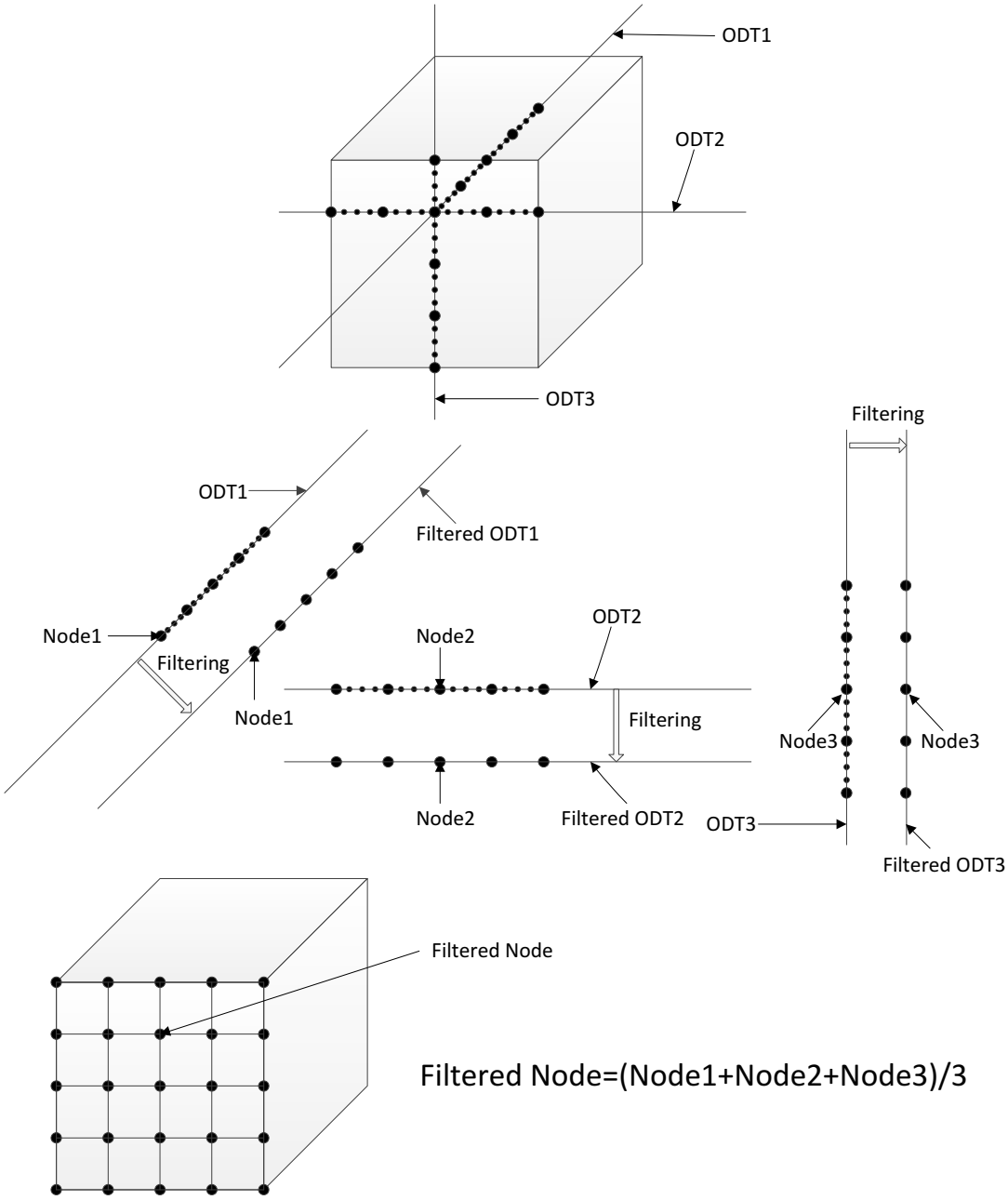

Figure 4.4: Filtering Diagram

4.4.1 Algorithm and Procedure

Currently, the adjustment of the ODT parameter is applied globally, meaning that one common parameter is applied for all the ODT domains, but it can also be applied locally for better matching. The procedure of the adjustment is shown as following.

1. **Parameter Initialization**

   The parameter is initialized at the beginning of the simulation. The initial value is guessed according to the type of the combustion flow; but it will eventually converge even if it is far away from the right value, only taking more time to converge.

2. **Wavelet Decomposition**

   A multi-level wavelet decomposition is performed for all three velocity component over all the ODT domains as well as the LES domain. The level of wavelet decomposition for ODT is determined by the difference between the smallest ODT scale and smallest LES scale. The ODT is wavelet transformed until it reaches the smallest LES scale. For example, if one ODT domain containing 256 grids and a corresponding LES line containing 16 grids, at least 4 level decomposition has to be applied to ODT so the information of the ODT at the coupling scale can be extracted. As for LES, 2 level wavelet decomposition is applied in order to get enough data from wavelet energy spectrum for slope calculation.

3. **Energy Spectrum Calculation**

   The energy spectrum is calculated for both LES and ODT using wavelet coefficients. As the wavelet energy spectrum is defined, the square of all wavelet coefficients are summed up at the same scale. Moreover, the energy for all three velocity components, u, v and w, are summed up as well to get the full energy spectrum for both

LES and ODT. The summation is done for all the available scales. The wavelet energy spectrum of ODT can be calculated as

$$E(a) = \sum_{j=1}^{N} \sum_{i} W_u(a, b_i)^2 + \sum_{j=1}^{N} \sum_{i} W_v(a, b_i)^2 + \sum_{j=1}^{N} \sum_{i} W_w(a, b_i)^2 \tag{4.8}$$

a is the parameter of scale; $W_u(a, b_i)$, $W_v(a, b_i)$ and $W_w(a, b_i)$ are the wavelet coefficient of u, v and w at scale a and location b_i. $N = nx \cdot ny + ny \cdot nz + nz \cdot nx$ is the number of the ODT domains, meaning that the energy spectrum is summed up for all ODT domains. The same calculation is also done for all LES lines. Therefore, the energy spectra of both LES and ODT are obtained in terms of scales.

4. **Energy Spectrum Slope Calculation**

   The slope of the energy spectra at the coupling scale, or the LES filter scale, is calculated for both LES and ODT. The current calculation is based on two points one side difference; but with finer resolution simulation and more scales, more points can be used for better accuracy.

5. **Parameter Adjustment**

   The ODT parameter, denoted as "C", is adjusted as

$$C^{t+\Delta t} = C^t \frac{\text{LES spectrum slope}}{\text{ODT spectrum slope}} \tag{4.9}$$

   The ODT parameter determines the turbulent intensity and the energy transfer rate from large scale to small scale, thus determines the energy spectrum slope. Large ODT parameter gives large ODT energy spectrum slope. If the energy slope of ODT is too large, meaning that energy transfer rate for ODT is too high, and more eddy events are happening than needed; thus reducing the ODT parameter

is needed, and *vice versa*.

4.4.2 Implementation

The above 4 steps should be executed for every LES time step. If the turbulence is steady, this approach can be implemented as a pre-run prior to the full simulation in order to determine the ODT parameter as a constant. As for the unsteady case, the procedures are coupled within LES-ODT advancement. The procedure for the both cases are expressed in Figure 4.5.

4.5 Results and Discussion

4.5.1 Case description and Non-dimensionalized Governing Equations

A case of auto-ignition in non-homogeneous mixture in decaying isotropic turbulence is used to test the validity of the three wavelet transform applications. The LES-ODT grid formulation is the same as discussed in chapter 2 with the ODT domains embedded in the LES domain. The governing equations for both LES and ODT are non-dimensionalized. The non-dimensionalized LES governing equations are shown in Eq. (4.10) and Eq. (4.11).

Continuity Equation:

$$\frac{\partial \bar{\rho}}{\partial t} + \frac{\partial \bar{\rho}\bar{u}_j}{\partial x_j} = 0 \tag{4.10}$$

Momentum Equation:

$$\frac{\partial \bar{u}_i}{\partial t} + \bar{u}_j \frac{\partial \bar{u}_i}{\partial x_j} = -\frac{1}{\bar{\rho}} \frac{\partial \bar{p}}{\partial x_i} + \frac{1}{\bar{\rho}\mathrm{Re}} \frac{\partial^2 \bar{u}_i}{\partial x_i \partial x_j} + \frac{1}{3\bar{\rho}\mathrm{Re}} \frac{\partial}{\partial x_i} \left(\frac{\partial \bar{u}_j}{\partial x_j} \right) + \frac{\partial}{\partial x_j} \left(\bar{u}_i \bar{u}_j - \overline{u_i u_j} \right) \tag{4.11}$$

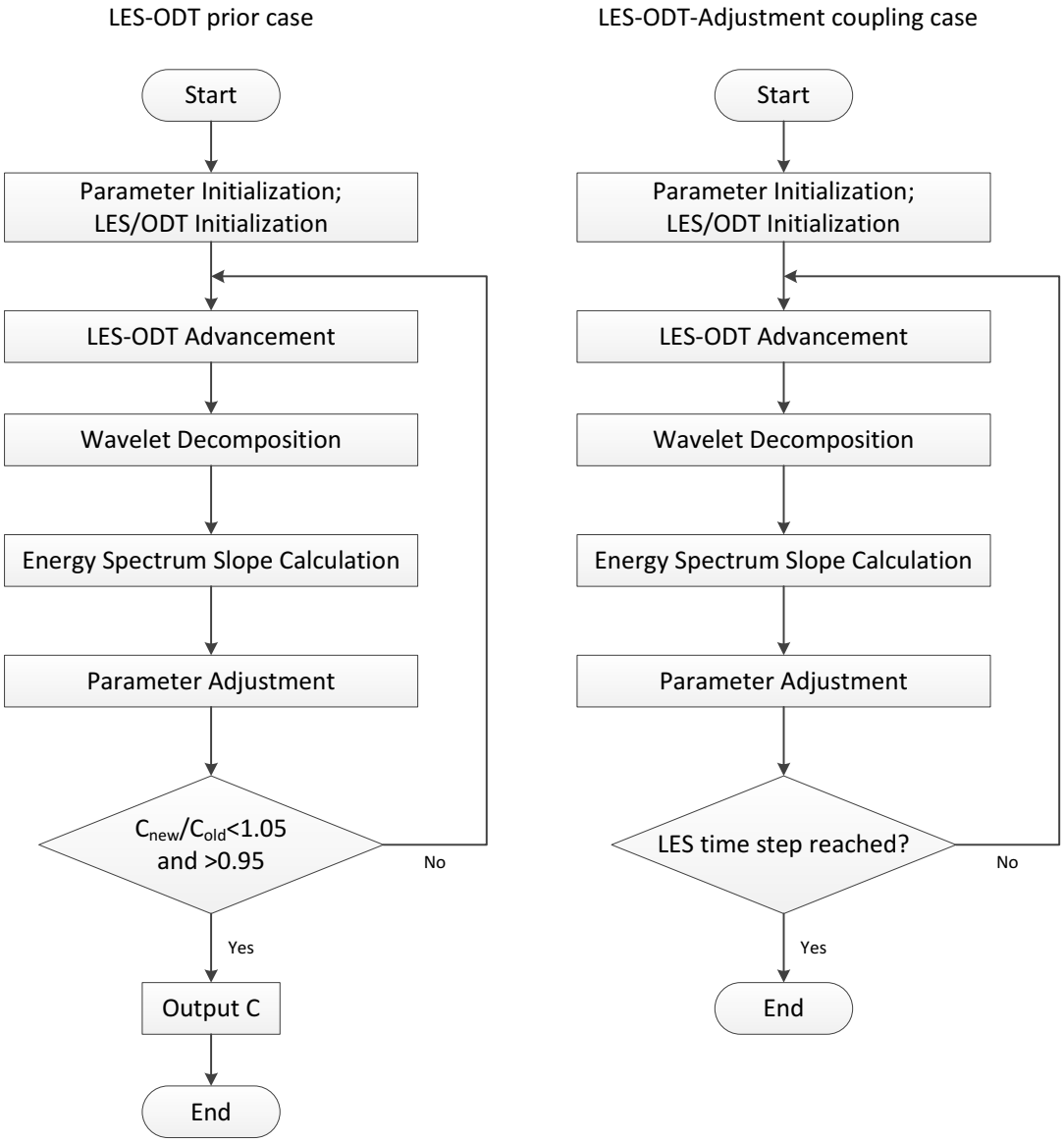

Figure 4.5: Flowchart for ODT parameter adjustment.

The over bars represent LES filtered quantities; $(\bar{u}_i\bar{u}_j - \overline{u_i u_j})$ is the subgrid stress; and Re is the Reynolds number. The non-dimensionalized ODT governing equations are expressed as

Momentum Equation:

$$\rho\frac{\partial u_i}{\partial t} = \left[\frac{3}{\mathrm{Re}}\frac{\partial^2 u_i}{\partial\eta\partial\eta} + \Omega_i\right] + \left\{-\frac{\partial\hat{P}}{\partial x_i} - \rho\hat{u}_j\frac{\partial u_i}{\partial x_j} + \frac{1}{3\mathrm{Re}}\frac{\partial}{\partial x_i}\left(\frac{\partial\hat{u}_j}{\partial x_j}\right)\right\} \tag{4.12}$$

Energy Equation:

$$\rho\frac{\partial T}{\partial t} = \left[\frac{3}{\mathrm{PrRe}}\frac{\partial^2 T}{\partial\eta\partial\eta} + \omega + \Omega_T\right] + \left\{-\rho\hat{u}_j\frac{\partial T}{\partial x_j}\right\} \tag{4.13}$$

Conservation of the Fuel:

$$\rho\frac{\partial Y_F}{\partial t} = \left[\frac{3}{\mathrm{LePrRe}}\frac{\partial^2 Y_F}{\partial\eta\partial\eta} - \omega + \Omega_{Y_F}\right] + \left\{-\rho\hat{u}_j\frac{\partial Y_F}{\partial x_j}\right\} \tag{4.14}$$

Conservation of the Oxidizer:

$$\rho\frac{\partial Y_O}{\partial t} = \left[\frac{3}{\mathrm{LePrRe}}\frac{\partial^2 Y_O}{\partial\eta\partial\eta} - \omega + \Omega_{Y_O}\right] + \left\{-\rho\hat{u}_j\frac{\partial Y_O}{\partial x_j}\right\} \tag{4.15}$$

The subscripts 'F' and 'O' refer to the fuel and the oxidizer, respectively. The terms with superscript " ˆ " represent filtered quantity from the LES. The non-dimensional parameters, Pr and Le are the Prandtl number and the Lewis number.

The parameters of the LES-ODT simulation are shown in Table 4.3. The parameters for LES and ODT are shown in Table 4.4 and Table 4.5, respectively. All these parameters are non-dimensionalized. The definition of some of the parameters are as follows [53].

1. **Reynolds number** (Re)

$$\mathrm{Re} = \frac{\rho_{ref} L_{ref} U_{ref}}{\mu} \tag{4.16}$$

2. **Prandtl number** (Pr)

$$\mathrm{Pr} = \frac{C_p \mu}{\lambda} \tag{4.17}$$

3. **Non-dimensional heat release** (α)

$$\alpha = \frac{T_{ad} - T_{ref}}{T_{ad}} \tag{4.18}$$

4. **Non-dimensional activation energy** (β)

$$\beta = \frac{E_a \alpha}{R_u T_{ad}} \tag{4.19}$$

5. **Damköhler number** (Da)

$$\mathrm{Da} = \frac{L_{ref}/U_{ref}}{\left[\frac{B}{W}\rho_{ref} \exp\left(-\frac{\beta}{\alpha}\right)\right]^{-1}} \tag{4.20}$$

6. **Zeroth-order pressure** (P_0)

$$P_0 = \rho \left[T\left(\frac{\alpha}{1-\alpha}\right) + 1\right] \tag{4.21}$$

While the subscript "ref" means the reference value during non-dimensionalization; μ is the dynamic viscosity; C_p is the specific heat; λ is the thermal conductivity; R_u is the ideal gas constant; T and ρ are non-dimensionalized temperature and density. T_{ad} is the

Table 4.3: Relevant parameters for LES-ODT simulation.

Domain dimension	$3.6 \times 3.6 \times 3.6$
Reynolds number	200
zeroth-order pressure	1.0
Prandtl number	0.7
Damköhler number	200
non-dimensional heat release	0.75
non-dimensional activation energy	2.0
Boundary condition	periodic

adiabatic temperature; E_a is the activation energy in Arrhenius law; B is the collision frequency factor in Arrhenius law and W represents the molecular weight under the assumption that all of the species have the same molecular weight. Under the low-Mach number approximation, the zeroth-order pressure is a constant. Detailed derivation of these non-dimensional numbers can be seen in Mason [53] and Cao [8].

The LES has a layout of $16 \times 16 \times 16$ grid size across the whole computational domain with an integration time step of $\Delta t = 0.04$. Every ODT domain has the length of 3.6 with 256 grids and there is a total of 768 of it. The viscous penalty is discussed in chapter 2 and the velocity energy exchange coefficients is also presented in chapter 2. The ODT eddy size is selected between 6 and 16 ODT grids. The three ODT time steps, the ODT stirring time step, the ODT diffusion time step and the ODT convection time step, are $\Delta t_s = 1.0 \times 10^{-5}$, $\Delta t_d = 1.2 \times 10^{-5}$ and $\Delta t_c = 0.9 \times 10^{-5}$, respectively.

The computational domain is initialized with non-homogeneous mixture with preheated oxidizer. The initial mixture fraction field is shown in Figure 4.6, and it is initialized

Table 4.4: Parameter for LES simulation.

LES domain dimension	$3.6 \times 3.6 \times 3.6$
LES grid	$16 \times 16 \times 16$
LES time step	0.04
SGS stress model	Smagorinsky model

Table 4.5: Parameter for ODT simulation.

Domain length	3.6
ODT grid	256
number of ODT domains	768 ($3 \times 16 \times 16$)
viscosity penalty	0.002
minimum eddy size	6
degree of energy exchange among velocities in ODT	0.33
ratio of maximum ODT eddy size to LES grid size	1
maximum ODT eddy size	16
ODT stirring time step	1.0×10^{-5}
ODT diffusion and reaction time step	1.2×10^{-5}
ODT convection time step	0.9×10^{-5}

randomly using the von Karman-Pao spectrum [8]. The reaction mechanism is simplified to single step and irreversible. Periodic boundary conditions are implemented for all three directions.

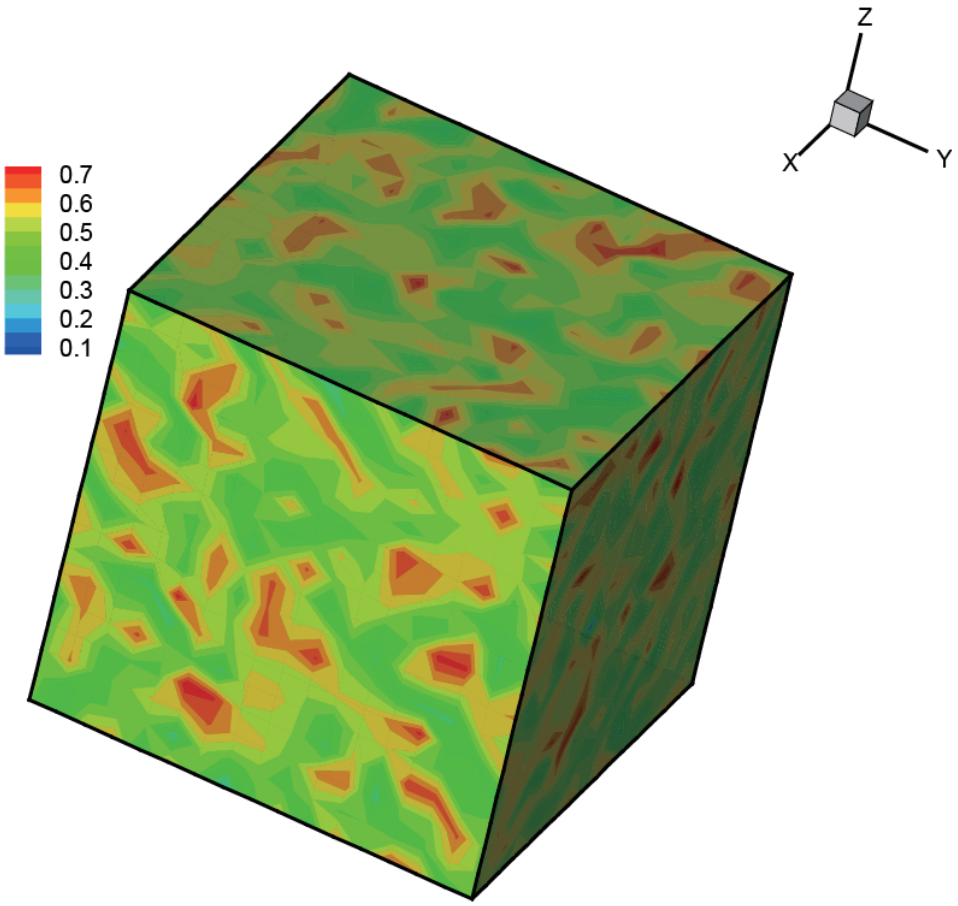

Figure 4.6: Initial mixture fraction field with preheated oxidizer.

4.5.2 Wavelet-Based Compounding

The wavelet-based compounding is done for the case stated above. For more intuitive illustration, the compounding results of two ODT domains, denoted as ODT1 and ODT2, and their corresponding LES lines are shown in Figure 4.7, but the compounding is done for the whole computational domain for the implementation. Daubechies 4 wavelet is used for the compounding.

The wavelet-based compounding is done for the case stated above. For more intuitive illustration, the compounding result of one ODT domain and its corresponding LES line is shown in Figure 4.7. But in the LES-ODT formulation, the compounding is done for the whole computational domain. Daubechies 4 wavelet is used for the compounding.

In Figure 4.7, the thin solid lines represent the LES lines, the thin dashed lines are the velocity of ODT domains, with the thin solid lines are the velocity of the ODT domains after the compounding process adopted in this dissertation. The wavelet-based compounding tracks the large scale contribution from LES and the residual contribution from ODT subgrid statistics. This trend coincide with the purpose of the downscaling process, as downscaling is to pass the resolved LES large scale information to ODT while keeping the ODT subgrid statistics intact. Furthermore, the ODT velocity field after the compounding is consistent with LES in large scale thus the ODT model has more accurate subgrid statistics as the subgrid information is passed from large scale. Due to the close relationship between the wavelet transform and the Fourier transform, the results of the compounding also shows consistency in Fourier domain as shown in Figure 4.8.

In Figure 4.8, the thin solid lines are the LES energy spectra, the thin dashed lines are the ODT energy spectra, and the thick solid lines represent the energy spectra of the ODT velocity after the compounding. As noted in the graph, the LES spectra have narrower

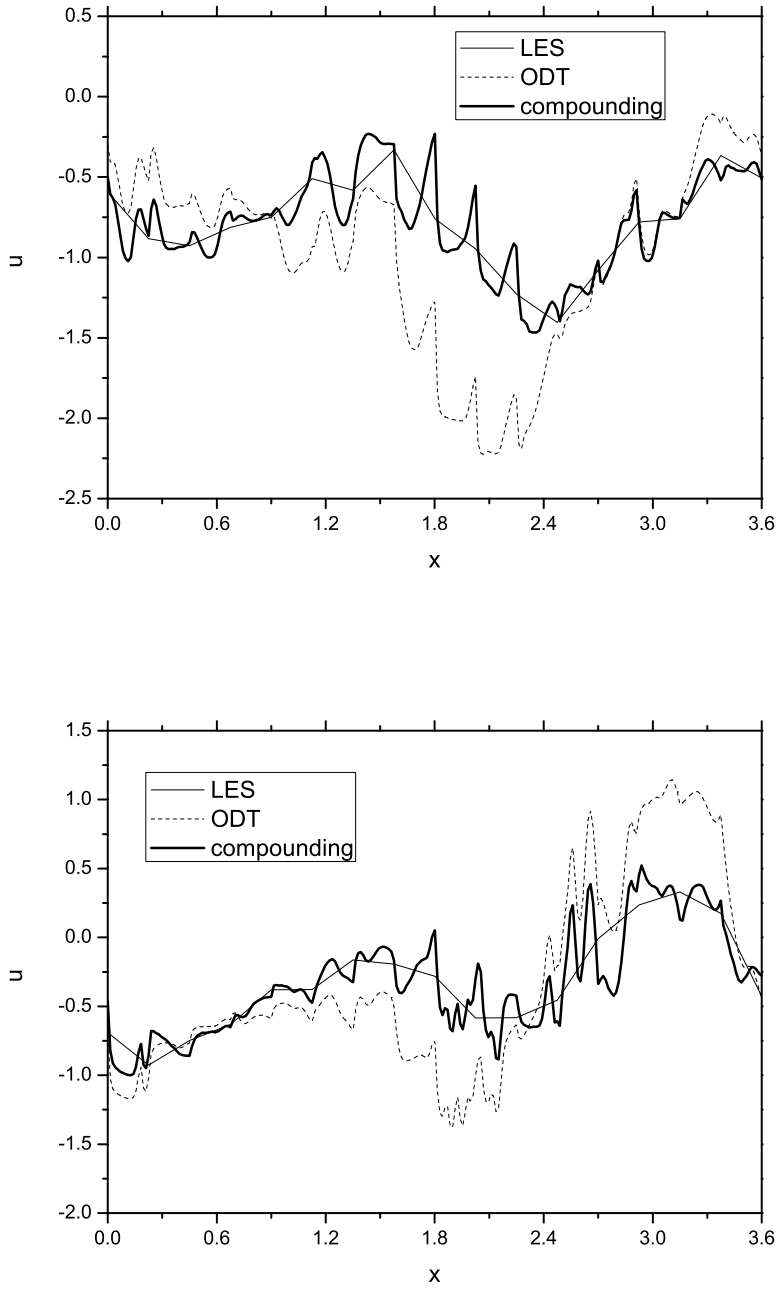

Figure 4.7: u velocity before and after compounding of ODT domain1 (upper one) and ODT domain2 (lower one).

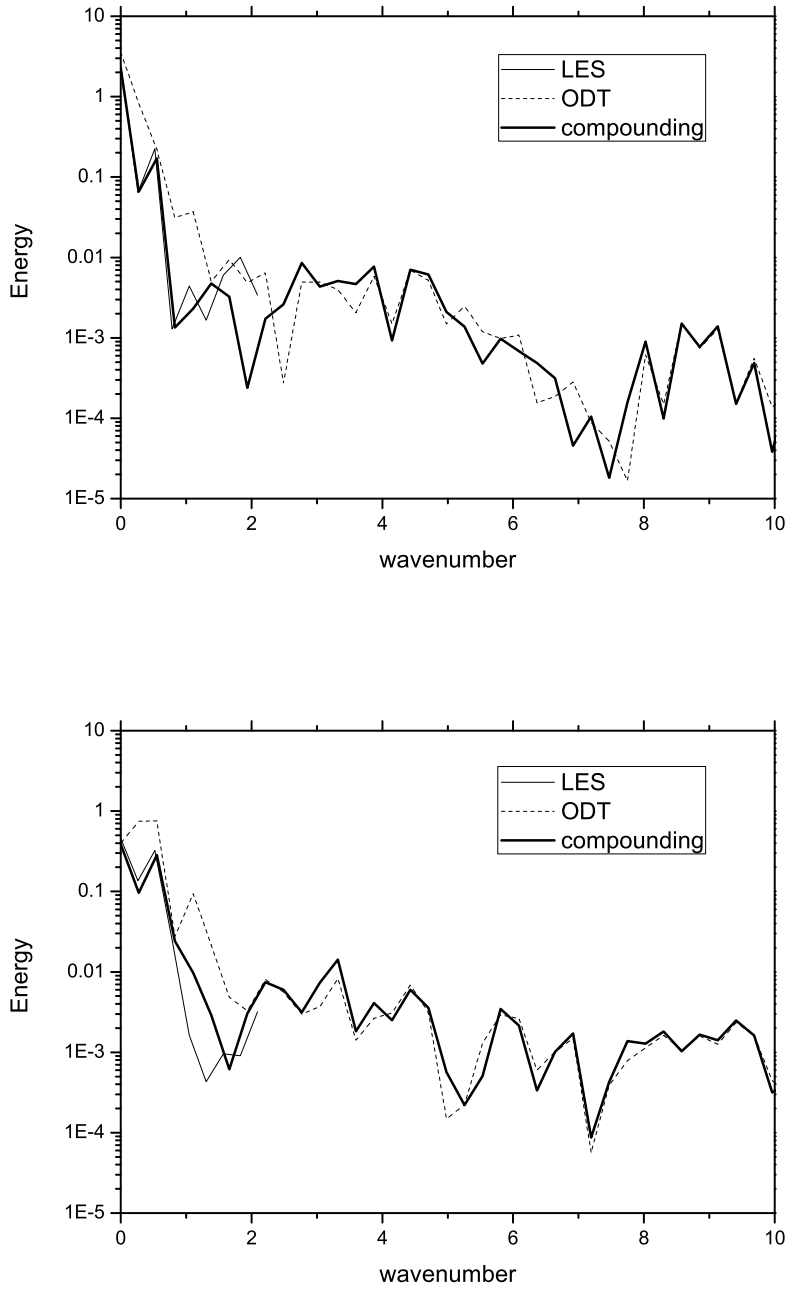

Figure 4.8: FFT of the u velocity before and after compounding of ODT domain1 (upper one) and ODT domain2 (lower one).

span in wavenumber coordinate compared with the ODT spectra. This is because the LES solutions cover less scales than the ODT, which corresponds a narrower wavenumber span. In the configuration in Tables. (4.3)–(4.5), the LES should have a wavenumber span of 1/16 of the ODT. In order to show the results more clearly, the results shown in Figure 4.8 are zoomed and part of the ODT and the compounded results are not shown.

The compounded results are consistent with the LES solution in low wavenumber or large scale and the ODT solution in high wavenumber which corresponds with small scale, with a minor inconsistency for the transition wavenumber.

As a superior alternative of the original interpolation based implementation, the comparison between the wavelet-based and the interpolation based implementations are carried out, and the results are shown in Figure 4.9. Furthermore, the comparison between the two approaches are also shown in Fourier space as in Figure 4.10.

The results in Figure 4.9 and Figure 4.10 shows that the wavelet-based compounding presents substantial advantages over the interpolation based compounding, which can be addressed as the following:

1. The wavelet-based compounding has the ability to retain large scale information from resolved LES solution and adding subgrid scale information. But according to Figure 4.9 and Figure 4.10, the interpolation based compounding is very close to the ODT solution thus does not preserve large scale information from LES;

2. The wavelet-based compounding approach provides a correction mechanism for ODT. It is very important for the ODT implementation as the subgrid closure model since ODT only has information along with the ODT domain orientation. For subgrid scale, it is possible to perform the calculation under the assumption of isotropic turbulence; but for large scale, it is crucial to provide large scale in-

(a) Interpolation based implementation for ODT domain 1.

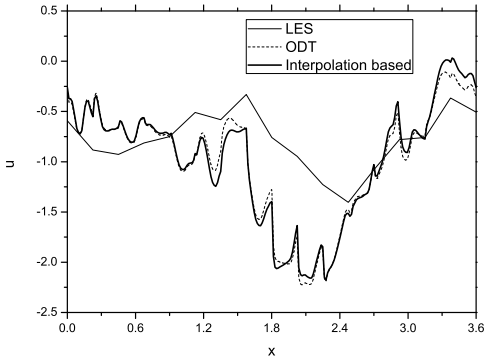

(b) Wavelet-based implementation for ODT domain 1.

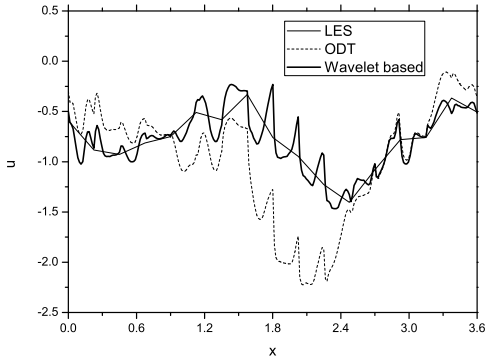

(c) Interpolation based implementation for ODT domain 2.

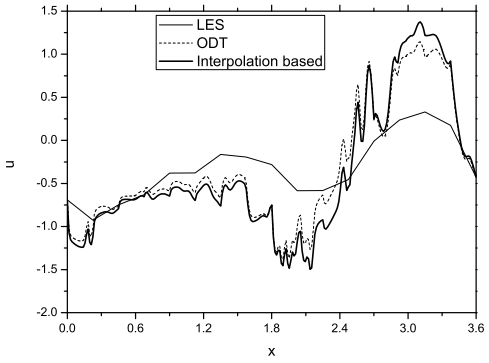

(d) Wavelet-based implementation for ODT domain 2.

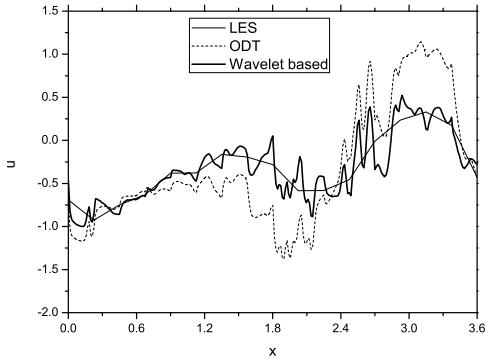

Figure 4.9: Comparison between the interpolation based compounding and the wavelet-based compounding.

(a) Interpolation based implementation for ODT domain 1.

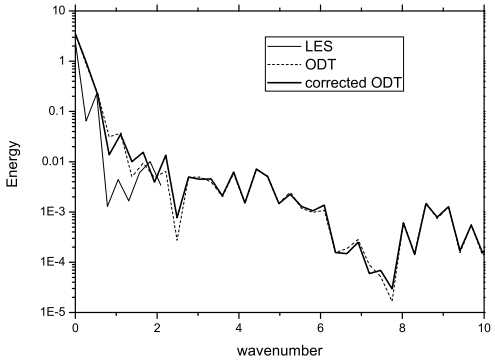

(b) Wavelet-based implementation for ODT domain 1.

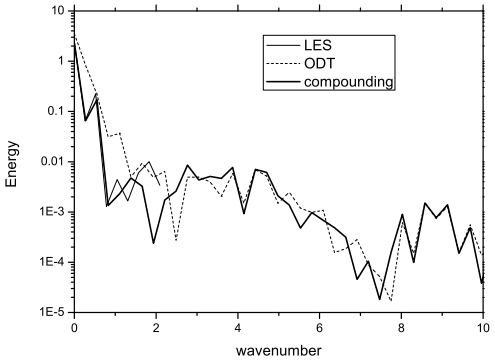

(c) Interpolation based implementation for ODT domain 2.

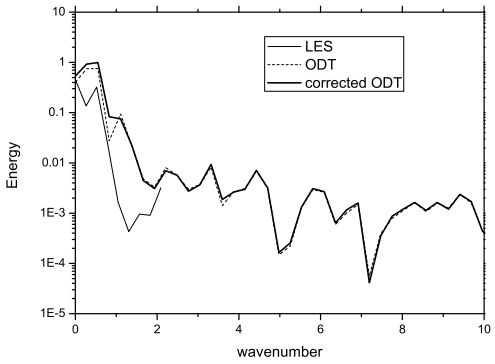

(d) Wavelet-based implementation for ODT domain 2.

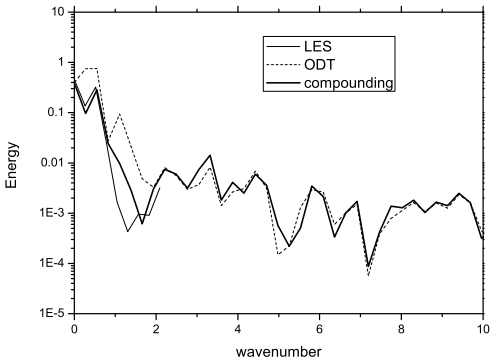

Figure 4.10: Comparison the Fourier spectra between the interpolation based compounding and the wavelet-based compounding.

formation to ODT. The wavelet-based compounding can perform this correction, whether in physical domain as in Figure 4.7 or in Fourier domain as in Figure 4.8;

3. The wavelet coefficients, which have the information of both scale and location, can be used for other application. For example, the wavelet coefficients can be used to distinguish the flame kernel information, both size and location.

As shown in chapter 3, there are many kinds of mother wavelets. Wavelet transform based on different mother wavelets for ODT domain 1 and ODT domain 2 are shown in Figure 4.11 and Figure 4.12, respectively. Wavelet transform based on different wavelet does not change the nature of the compounding as all four kinds of wavelet transforms have the ability to capture the large scale trend and small scale fluctuations. But, in terms of consistency, it is still obvious that the Daubechies 4 wavelet has the best consistency for small scale fluctuations between the compounded solution and the ODT solution. From mathematical point of view, it is suggested that the mother wavelet should have similar shape as the features that need to be captured. This can be explained from the definition of the wavelet transform Eq. (3.16), the wavelet coefficients is maximized if the mother wavelet $\psi(t)$ is the same as the feature to be detected. Also, by comparing the shape of the Daubechies 4 mother wavelet Figure 3.6d with the triplet map shape Figure 2.3, they have the most similar shape among all other kinds of wavelets.

It is also very important to address the computational cost of the wavelet-based compounding implementation. Although the wavelet transform is done for every ODT domains, due to the low cost nature of the wavelet transform, the wavelet-based compounding does not add extra noticeable time cost to the simulation. Profiling results show that the compounding subroutine takes less than 1% of the total computational time cost.

(a) Compounding based on Haar wavelet.

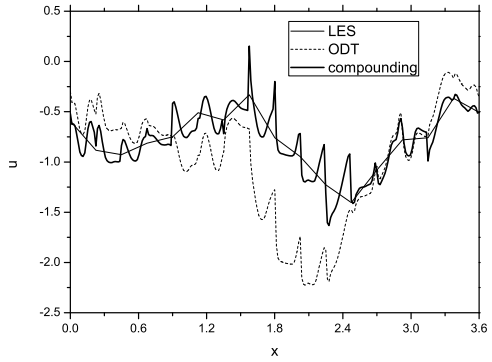

(b) Compounding based on Daubechies 4 wavelet.

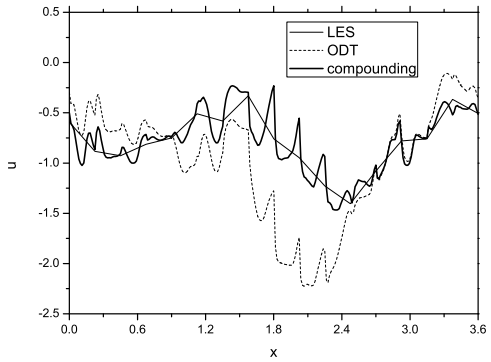

(c) Compounding based on Meyer wavelet.

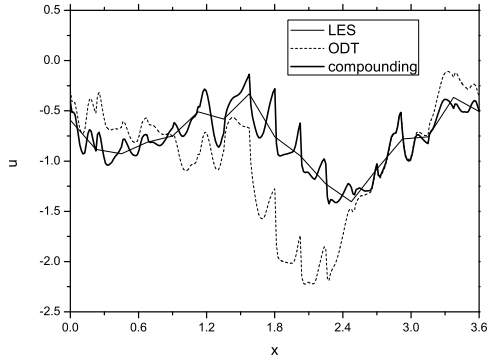

(d) Compounding based on symlet wavelet.

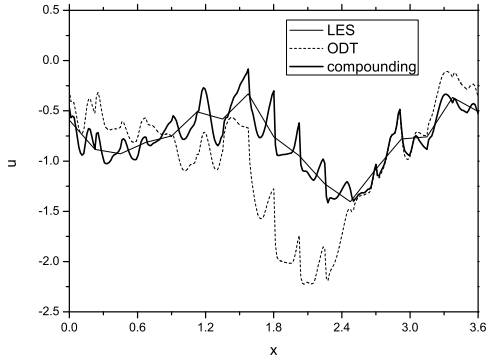

Figure 4.11: Comparison of compounding based on different wavelets of ODT domain1.

(a) Compounding based on Haar wavelet.

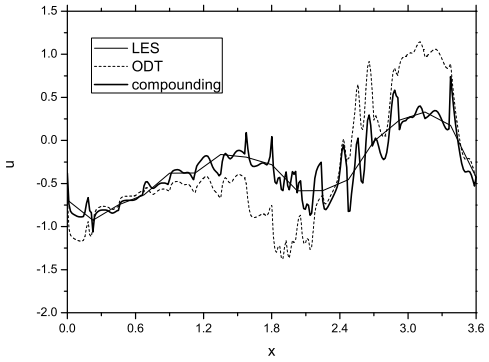

(b) Compounding based on Daubechies 4 wavelet.

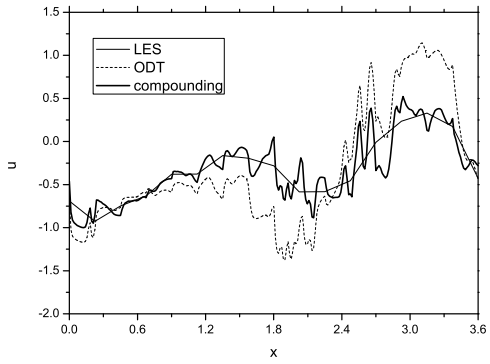

(c) Compounding based on Meyer wavelet.

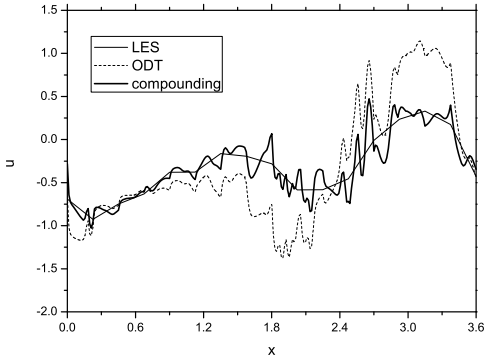

(d) Compounding based on symlet wavelet.

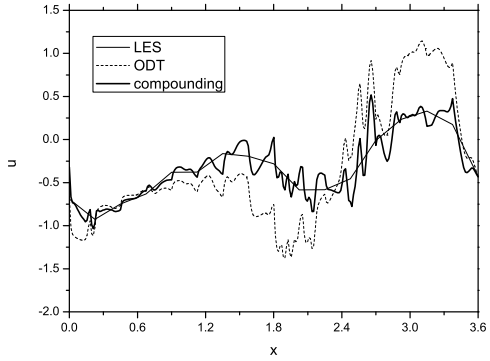

Figure 4.12: Comparison of compounding based on different wavelets of ODT domain2.

4.5.3 Wavelet-Based Spatial Filtering of Combustion Features

The wavelet-based spatial filtering is applied for both density and the progress variable. It is also applied for the same auto-ignition in isotropic decaying turbulence case introduced in chapter 4.5.1.

Filtering the density

The filtering is used to pass ODT density information to LES. Since ODT have all the chemical reaction information while LES does not, the density information from ODT which can be effected by chemical reactions is filtered and passed to LES for the following iteration.

In the original LES-ODT formulation by Cao & Echekki [9], box filter is used for the filtering. As for the compounding part discussed in chapter 4.5.2, the wavelet-based approach has major advantages for multiscale problems. Consider density fields for two ODT domains, ODT 1 and ODT 2, the density field of the two ODT domains are show as well as the filtered density fields and the wavelet-based filtered density fields are shown in Figure 4.13. For both ODT domains, the wavelet-based filtering has the ability to capture peaks while the box filter is smoothing the peaks. This can be further shown in the comparison in Fourier domain as shown in Figure 4.14. The wavelet filtered density has much more consistency in Fourier domain with the large scale ODT density than the filtered density. The ability to detect peaks is very important in detecting flame kernels, thin flame front, *etc.*

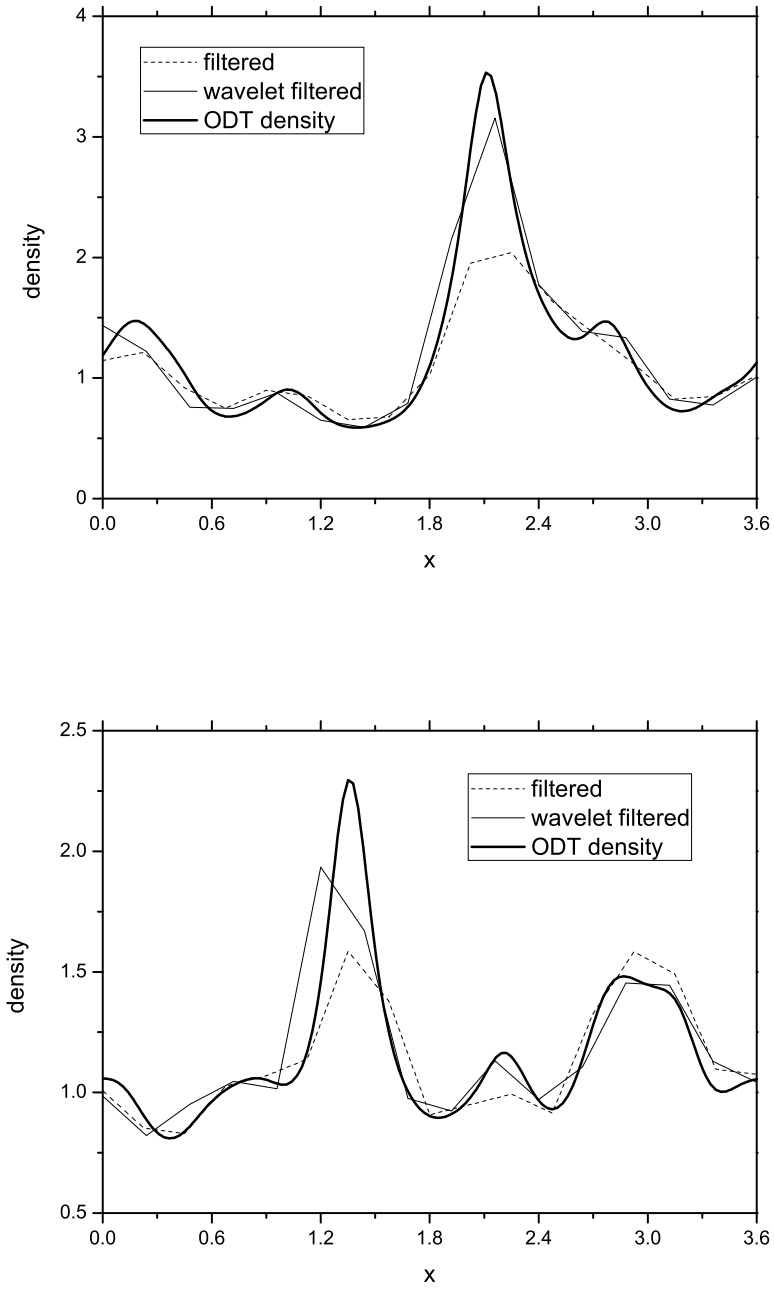

Figure 4.13: Comparison between ODT density field, filtered density field and wavelet-based filtered density field for ODT domain 1 (upper) and ODT domain 2 (lower).

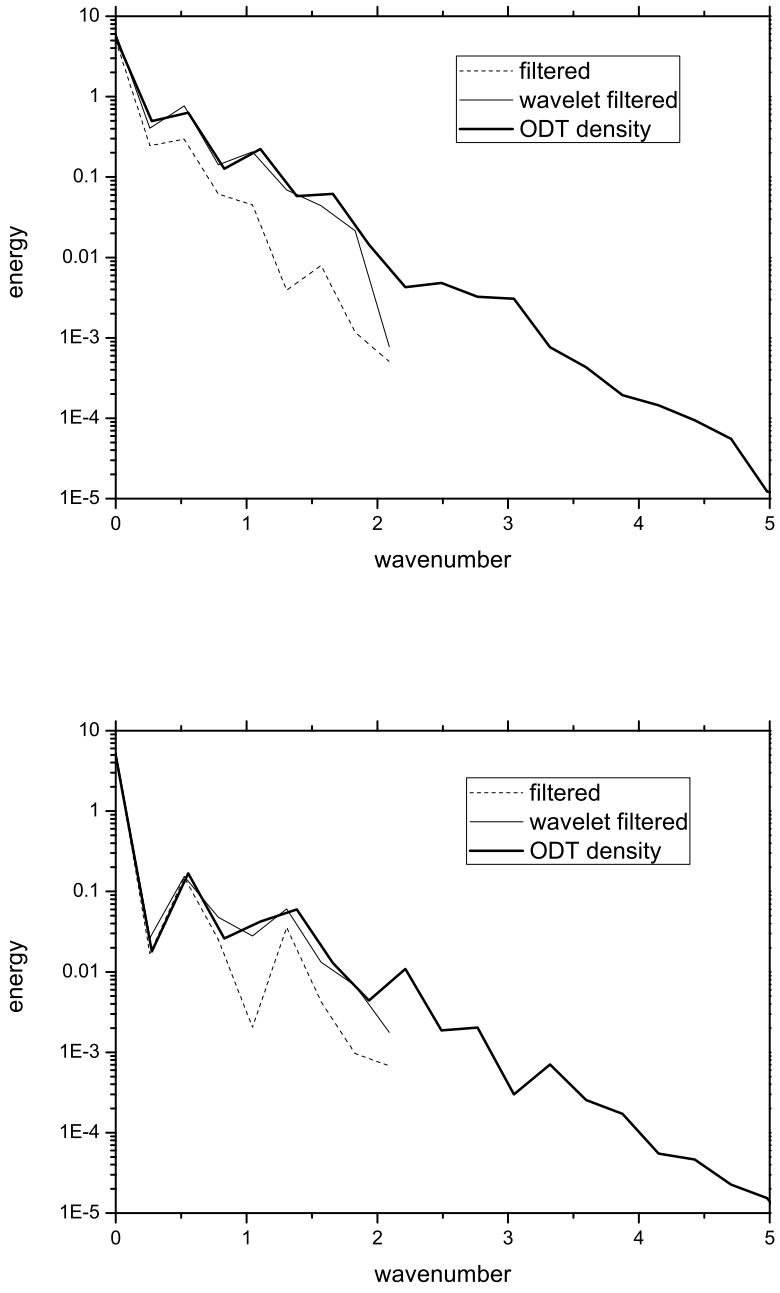

Figure 4.14: FFT comparison between ODT density field, filtered density field and wavelet-based filtered density field for ODT domain 1 (upper) and ODT domain 2 (lower).

Filtering the progress variable

The combustion features occur from small scale first. In order to detect these small scale combustion features, wavelet-based filtering is used. The iso-surfaces for progress variable of 0.5 at different time steps are presented in Figure 4.15. The four graphes correspond to the 1st, 11st, 21st and 31st LES time step, which is at dimensionless time of 0.04, 0.44, 0.84 and 1.24.

The combustion features come from ODT; and because of the wavelet-based filtering process, which zeros out all small scale information, the combustion only appears at small scales without showing any large scale features, as shown in Figure 4.15a. In Figure 4.15b, discrete small flame kernels appear at small scales and is detectable even from LES scale. Because of the peak preserving feature of the wavelet-based filtering, small flame kernels are preserved rather than smoothed out. As the auto-ignition process proceeds, different flame kernels begin to merge, showing as a larger continuous flame across the whole computational domain as shown in Figure 4.15c. And finally, in Figure 4.15d, combustion appears in the whole domain, and flames are fully developed.

4.5.4 Wavelet Spectra Based ODT Parameter Determination

The wavelet spectra based ODT parameter determination is also applied to the auto-ignition in non-homogeneous mixture in decaying isotropic turbulence case. Figure 4.16 shows the wavelet energy spectra before and after the ODT parameter adjustment. The circled points in both the dash line and the solid line indicate the LES subfilter scale and both the LES wavelet energy spectrum slope and ODT wavelet energy spectrum slope are calculated at this point. The ODT parameter adjustment shows great improvement of the consistency between LES and ODT energy spectrum thus ODT has better coupling

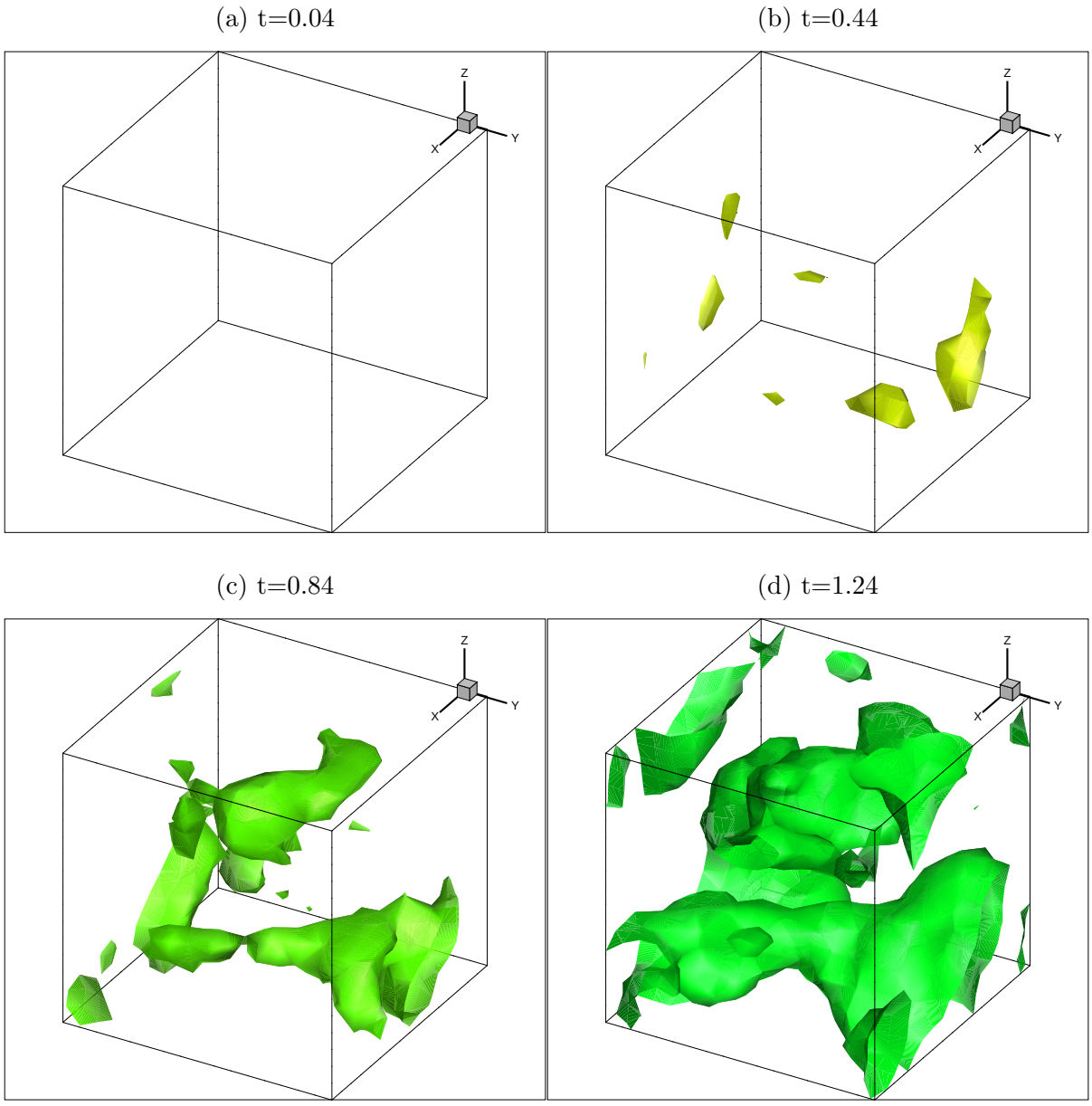

Figure 4.15: Iso-surface of progress variable at 0.5 at different dimensionless time.

with LES as a subgrid closure model.

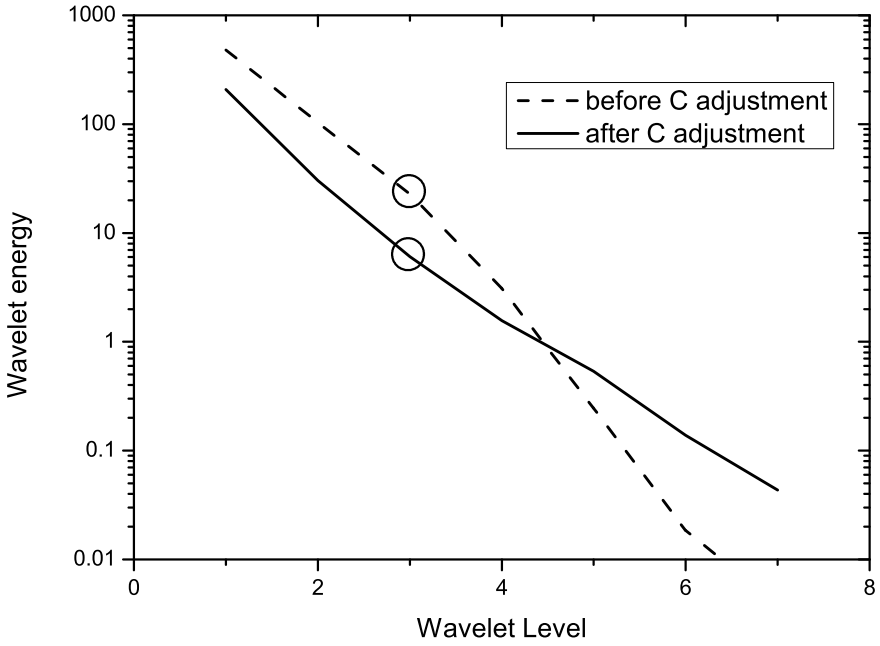

Figure 4.16: Wavelet energy spectrum before and after C adjustment.

The other way of showing the efficiency of the ODT parameter determination approach is by tracking the ODT parameter during the simulation. The ODT parameter tracking result is shown in Figure 4.17. In this simulation, the initial guess, which is 200, is much larger than the actual value of the parameter, which is around 70 according to the final converged value. As the code runs, the parameter converges to the right value within 10 LES time steps, which is just a fraction of time of the full simulation. Therefore, the incorrect parameter does not effect the simulation too much. The time steps that is needed for convergence can be further reduced by guessing the initial value closer to the

converged value.

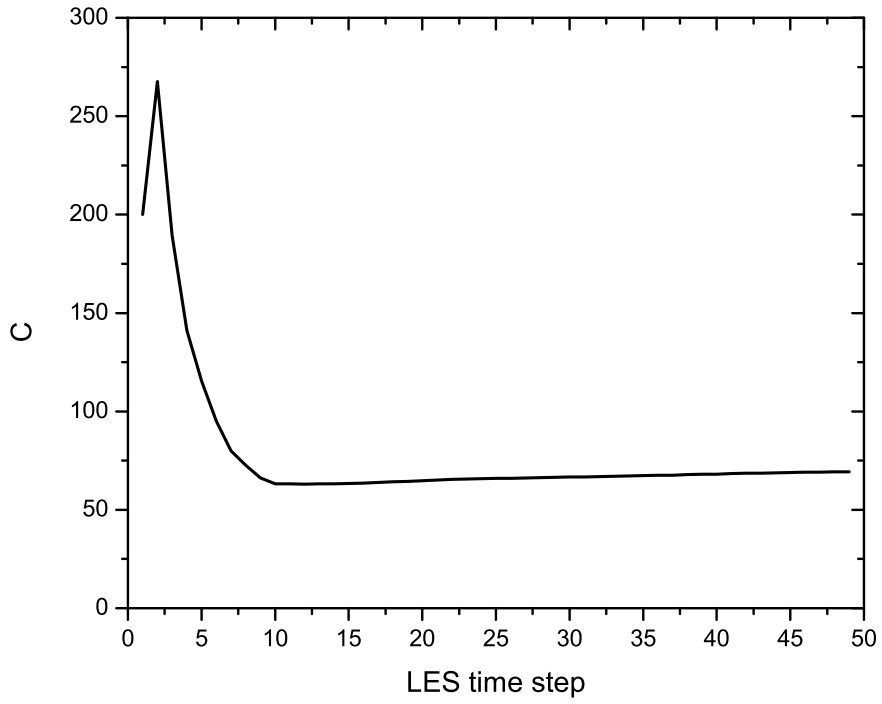

Figure 4.17: Calibration process for ODT parameter during LES-ODT simulation.

4.6 Summary

In this chapter, the wavelet-based downscaling approach is implemented to the LES-ODT model. By combining the large scale wavelet coefficients of the LES velocity components and the small scale wavelet coefficients of the ODT velocity components, the compounded velocity fields show consistency with the LES velocity in large scale and ODT in small

scale in both physical domain and Fourier domain. This shows significant improvement with the original interpolation based downscaling which introduces small scale fluctuations during interpolation. Also, inspired by the energy detection feature of the wavelet transform, filtering of density and progress variable in physical domain is also adopted, which results in smaller energy distortion in large scale. Also, by matching the LES and ODT energy spectra at the compounding point, the ODT parameter can be determined. A bettering coupling is achieved by adjusting the ODT parameter to the right value.

Chapter 5

Kalman Filter and Kalman Filter Based Assimilation Approach

5.1 Introduction and Objective

Proposed by Rudolf E. Kalman [33, 32], Kalman filter is essentially a set of mathematical equations that implement a predictor-corrector type estimator that is optimal in the sense that it minimizes the estimated error covariance when some presumed conditions are met [83]. Cahuzac, *et al.* [6, 7] proposed a point based Kalman filter approach to extract low frequency turbulent features in large-eddy simulation. The ensemble Kalman filter (EnKF) [17] was also developed when a massive number of observations or predictions are presented. By selecting a limited number of samples out of many observations or predictions to reduce the computational cost, the EnKF is widely used in simulation of large scale turbulent systems, like weather forecasting, ocean system, *etc.* [17, 25].

The objective of this chapter is to introduce a novel Kalman filter based upscaling scheme for LES-ODT coupling. Since ODT solves for thermo-chemical scalars while LES

does not, ODT can capture heat release which impacts the density of the flow. This approach is achieved by filtering ODT density into LES grid in the formulation proposed by Cao & Echekki [9]. A potential drawback of the filtering operation may result from the limited sample of ODT resolution used to evaluate the filtered density [80]. Also, filtering density from ODT to LES may impair the mass conservation of LES itself. The sample noise can be reduced by adding more ODT solutions within one LES cell which will increase the computational cost. But the mass conservation cannot be guaranteed since ODT is a stochastic model. An alternative way of upscaling is the Kalman filter based smoothing process across a broad range of wave numbers, or assimilation process in general. This process addresses the coupling of a coarse-grained deterministic density solution from LES with a fine-grained stochastic density solution from ODT. This coupling is established primarily because of the redundancy of density solution between LES and ODT. Kalman filter is used to combine the two density solutions.

Two solutions are considered by the Kalman filter. Within the LES-ODT framework, the two solutions are the density fields obtained from LES and ODT. The deterministic solution of density field is corrected with the stochastically density field obtained from ODT. With the estimation of the errors from both solutions, the result density field that Kalman filter produces would be better than both in terms of the estimated error covariance. The density field result from the Kalman filter has several desired properties which includes the following:

1. Being a filter, the Kalman filter has the ability to smooth the density field and filters out small scale fluctuations of the filtered ODT density field. These fluctuations are due to the averaging process of the 3 ODT points, which cannot be filtered out by a traditional filter.

2. By combing the LES density and the filtered ODT density, result density of the Kalman filter takes consideration of both the continuity information from LES and the chemical reaction information from ODT.

5.1.1 Model Formulation

For the LES-ODT framework considered in this dissertation, Kalman filter combines the filtered density from the ODT solution and the LES density solution. The resulting density field represents the advancement of the LES density field in the following integration. The information involved in the Kalman filter implementation includes:

- **The State Vector $\boldsymbol{x}$:**

  In the current model formulation, the state vector corresponds to the LES density field. The state vector can be written as:

$$\overline{\boldsymbol{\rho}} = \left(\overline{\rho}_{1,1,1}, \overline{\rho}_{1,1,2}, \cdots, \overline{\rho}_{1,1,N}, \overline{\rho}_{1,2,1}, \overline{\rho}_{1,2,2}, \cdots, \overline{\rho}_{N,N,N}\right)^T \tag{5.1}$$

  That is, the vector has the length of $N \times N \times N$, and N is the size of the LES grid in one direction.

- **The Prediction Matrix $\boldsymbol{A}$:**

  The prediction matrix is used to relate the previous step at time step $k-1$ to the current time step k. Here, it is assumed that the evolution of the large scale density from LES is very slow compared to the evolution of the small scale density from ODT so that no deterministic evolution is prescribed for $\overline{\boldsymbol{\rho}}$: $\overline{\boldsymbol{\rho}}_k = \overline{\boldsymbol{\rho}}_{k-1}$, which implies

$$\boldsymbol{A} = \boldsymbol{I} \tag{5.2}$$

- **The Observation $\boldsymbol{z}$:**

  The observation vector $\boldsymbol{z}$ is a set of data that is obtained independently from the state vector, and it is used to "correct" the prediction result. Here, filtered density of ODT $\overline{\boldsymbol{\rho}}_f$ is used for the observation.

$$\overline{\boldsymbol{\rho}}_f = \left(\overline{\rho}_{f,1,1,1}, \overline{\rho}_{f,1,1,2}, \cdots, \overline{\rho}_{f,1,1,N}, \overline{\rho}_{f,1,2,1}, \overline{\rho}_{f,1,2,2}, \cdots, \overline{\rho}_{f,N,N,N}\right)^T \tag{5.3}$$

- **The Measurement Error Covariance Matrix $\boldsymbol{R}$:**

  The measurement error covariance matrix $\boldsymbol{R}$ is associated with the ODT small scale fluctuations. It is modeled as the root mean square (RMS) of the ODT points around one certain LES grid point. A 2D illustration is shown in Figure 5.1, the ODT points inside the circle are considered when calculating the error of the LES point in the center of the figure. In 3D LES-ODT formulation, it is actually the ODT points inside a sphere rather than a circle shown here. With all of the density from identified ODT points collected, denoted as $\rho_1, \rho_2, \rho_3, \cdots, \rho_m$ with m representing the ODT points within the range of the LES point, the measurement error vector $\boldsymbol{v}$ is calculated as

$$\boldsymbol{v}_{i,j,k} = \sqrt{\rho_1^2 + \rho_2^2 + \cdots + \rho_m^2} \tag{5.4}$$

  The symmetric error covariance matrix is calculated as

$$\boldsymbol{R} = < \boldsymbol{v}, \boldsymbol{v}^T > = \boldsymbol{v} \cdot \boldsymbol{v}^T \tag{5.5}$$

  $\boldsymbol{v}$ is a vector of length N^3, so $\boldsymbol{R}$ is a square matrix of size $N^3 \times N^3$.

- **The Process Error Covariance Matrix $\boldsymbol{Q}$:**

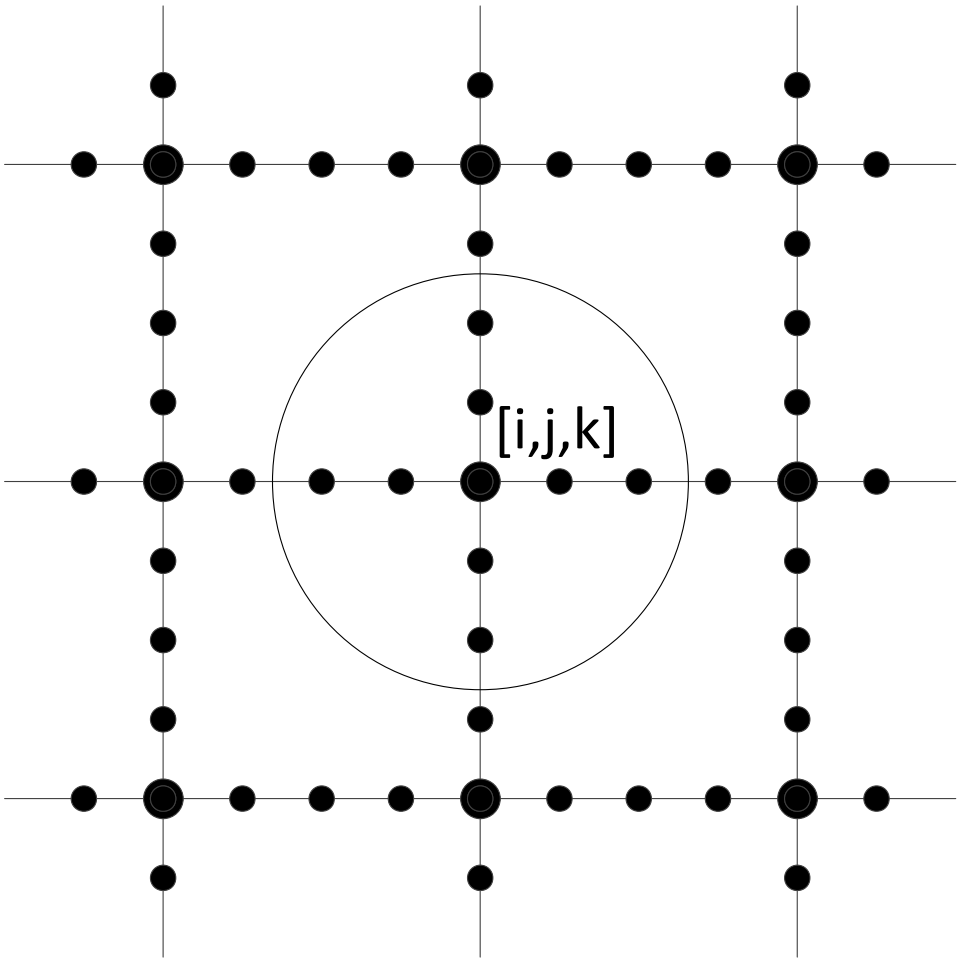

Figure 5.1: Error covariance matrix cover range.

The process error covariance matrix, or the LES error covariance matrix, is associated with the discretization of the LES solution. It is considered as the truncation error of LES model formulation. With the fluctuations appearing mainly in ODT, it is valid to assume that the process error vector $\boldsymbol{w}$ remains constant during the whole simulation. It is prescribed as an empirical value, but for the further refinement of this model, it is reasonable to address further details about the process error. The process error covariance matrix $\boldsymbol{Q}$ is calculated as

$$\boldsymbol{Q} =< \boldsymbol{w}, \boldsymbol{w}^T >= \boldsymbol{w} \cdot \boldsymbol{w}^T \tag{5.6}$$

$\boldsymbol{w}$ is a vector of length N^3, and $\boldsymbol{Q}$ is a square matrix of size $N^3 \times N^3$.

- **The $\boldsymbol{H}$ Matrix:**

  The $\boldsymbol{H}$ matrix relates the observation vector to the state vector. Since both the observation and the state vector are filtered density in the LES-ODT formulation,

$$\boldsymbol{H} = \boldsymbol{I} \tag{5.7}$$

- **Initialization of the Error Covariance Matrix $\boldsymbol{P}$:**

  The error covariance matrix $\boldsymbol{P}$ represents the error of the model and it decreases during the simulation. It is initialized as the LES error covariance matrix $\boldsymbol{Q}$:

$$\boldsymbol{P}_1 = \boldsymbol{Q} \tag{5.8}$$

- **Kalman Gain Matrix $\boldsymbol{K}$:**

  The Kalman gain matrix $\boldsymbol{K}$ is used to minimize the error estimated by error co-

variance matrix $\boldsymbol{P}$. There are a lot of forms of the Kalman gain matrix, and the derivation of the Kalman gain matrix is purely mathematical. Detailed discussion about the derivation and different forms of Kalman gain matrices can be seen in Maybeck [54], Jacobs [29] and Brown & Hwang [4].

The calculation for the Kalman gain matrix K_k at time step k can be expressed as

$$\boldsymbol{K}_k = \boldsymbol{P}_k^- \boldsymbol{H}^T (\boldsymbol{H} \boldsymbol{P}_k^- \boldsymbol{H}^T + \boldsymbol{R})^{-1}, \tag{5.9}$$

if the ODT error covariance matrix is zero matrix, $\boldsymbol{R} = \boldsymbol{0}$, meaning that ODT is accurate, and $\boldsymbol{K}_k = \boldsymbol{H}^{-1}$. Substituting back into the estimation update equation Eq. (5.9) gives $\boldsymbol{x}_k = \boldsymbol{z}_k$. On the other hand, if the prediction error is zero, $\boldsymbol{Q} = \boldsymbol{0}$, $\boldsymbol{P}_k^-$ is a zero matrix also, resulting in $\boldsymbol{K}_k = \boldsymbol{0}$. Another way of understanding the Kalman gain matrix is that when the prediction error is small compared with the observation error, the Kalman filter trusts the prediction result more, and *vice versa*.

Using the implementation shown above, the standard Kalman filter calculation is shown in the following steps:

1. **Projection of the State:**

$$\overline{\boldsymbol{\rho}}_k^- = \overline{\boldsymbol{\rho}}_{k-1}^- \tag{5.10}$$

2. **Projection of Error Covariance Matrix:**

$$\boldsymbol{P}_k^- = \boldsymbol{P}_{k-1} + \boldsymbol{Q} \tag{5.11}$$

3. **Compute the Kalman Gain:**

$$\boldsymbol{K}_k = \boldsymbol{P}_k^- (\boldsymbol{P}_k^- + \boldsymbol{R})^{-1} \tag{5.12}$$

4. **Update the Estimate:**

$$\overline{\boldsymbol{\rho}}_k = \overline{\boldsymbol{\rho}}_k^- + \boldsymbol{K}_k (\overline{\boldsymbol{\rho}}_{f,k} - \overline{\boldsymbol{\rho}}_k^-) \tag{5.13}$$

5. **Update the Error Covariance Matrix:**

$$\boldsymbol{P}_k = (\boldsymbol{I} - \boldsymbol{K}_k) \boldsymbol{P}_k^- \tag{5.14}$$

All vectors are of length N^3 and all matrices are square matrices with size of $N^3 \times N^3$. N is LES grid number in one direction. Eq. (5.10) and Eq. (5.11) are often denoted as the prediction steps, while Eq. (5.12), Eq. (5.13) and Eq. (5.14) are often denoted as the correction steps. The corrected results, $\boldsymbol{x}_k$ and $\boldsymbol{P}_k$, which are obtained in the correction steps will feed back into Kalman filter prediction steps as the input for next time step iteration. In Kalman filter, the prediction and correction steps are executed alternately.

5.1.2 Model Simplification

As can be noticed in the Kalman filter formulation for LES-ODT model, all matrices are diagonal matrices. The product of two diagonal matrices is a diagonal matrix and the inverse of a diagonal matrix is also a diagonal matrix, with element to element

correspondence.

$$\begin{bmatrix} a_1 & & & \\ & a_2 & & 0 \\ & & a_3 & \\ & 0 & & \ddots \\ & & & & a_n \end{bmatrix} \cdot \begin{bmatrix} b_1 & & & \\ & b_2 & & 0 \\ & & b_3 & \\ & 0 & & \ddots \\ & & & & b_n \end{bmatrix} = \begin{bmatrix} a_1 b_1 & & & \\ & a_2 b_2 & & 0 \\ & & a_3 b_3 & \\ & 0 & & \ddots \\ & & & & a_n b_n \end{bmatrix} \tag{5.15}$$

$$\begin{bmatrix} a_1 & & & \\ & a_2 & & 0 \\ & & a_3 & \\ & 0 & & \ddots \\ & & & & a_n \end{bmatrix}^{-1} = \begin{bmatrix} \frac{1}{a_1} & & & \\ & \frac{1}{a_2} & & 0 \\ & & \frac{1}{a_3} & \\ & 0 & & \ddots \\ & & & & \frac{1}{a_n} \end{bmatrix} \tag{5.16}$$

With the implementation shown above, all points are decoupled with no information exchange between adjacent points. Instead of applying inversion for $N^3 \times N^3$ matrices, only N^3 reciprocal operations are needed. For every LES grid point with indices of i, j and k, the simplified Kalman filter implementation is

$$\begin{cases} \overline{\boldsymbol{\rho}}_k^-(i,j,k) = \overline{\boldsymbol{\rho}}_{k-1}^-(i,j,k) \\ \boldsymbol{P}_k^-(i,j,k) = \boldsymbol{P}_{k-1}(i,j,k) + \boldsymbol{Q}(i,j,k) \\ \boldsymbol{K}_k(i,j,k) = \dfrac{\boldsymbol{P}_k^-(i,j,k)}{\boldsymbol{P}_k^-(i,j,k) + \boldsymbol{R}(i,j,k)} \\ \overline{\boldsymbol{\rho}}_k(i,j,k) = \overline{\boldsymbol{\rho}}_k^-(i,j,k) + \boldsymbol{K}_k(i,j,k)(\overline{\boldsymbol{\rho}}_{f,k}(i,j,k) - \overline{\boldsymbol{\rho}}_k^-(i,j,k)) \\ \boldsymbol{P}_k(i,j,k) = (1 - \boldsymbol{K}_k(i,j,k))\boldsymbol{P}_k^-(i,j,k) \end{cases} \tag{5.17}$$

5.1.3 Implementation

The implementation of Kalman filter is shown in Figure 5.2. The Kalman filter is implemented within each LES time step, and only a few extra subroutines are needed without changing the main structure of the LES-ODT formulation. The calculation of the LES error covariance matrix $\boldsymbol{Q}$ is needed in the initialization part to initialize the error covariance matrix $\boldsymbol{P}$. A subroutine with a loop of N^3 scalar Kalman filter is also implemented for updating the density and error covariance purpose.

5.2 Results

5.2.1 Case description

The LES-ODT formulation with Kalman filter based upscaling is implemented for a problem of twin planar premixed flames in decaying isotropic turbulence in a simple geometry. The non-dimensionalized governing equations for both LES and ODT are shown in Eqs. (4.10)–(4.11) and Eqs. (4.12)–(4.15), respectively. The initial field of mass fraction for both reactant and oxidizer are shown in Figure 5.3 with mass fraction of reactant and oxidizer equal to each other everywhere. The twin flames are separated by reactants. They will propagate toward each other and finally the two flames will merge. The grid formulation follows the same formulation of Cao & Echekki [9] for the non-homogeneous auto-ignition case which is presented in Chapter 2.

The parameters for the LES-ODT simulation are shown in Table 5.1. The parameters for LES and ODT are shown in Table 5.2 and Table 5.3, respectively. All these parameters are non-dimensionalized. The definition of the Reynolds number Re, Prandtl number Pr,

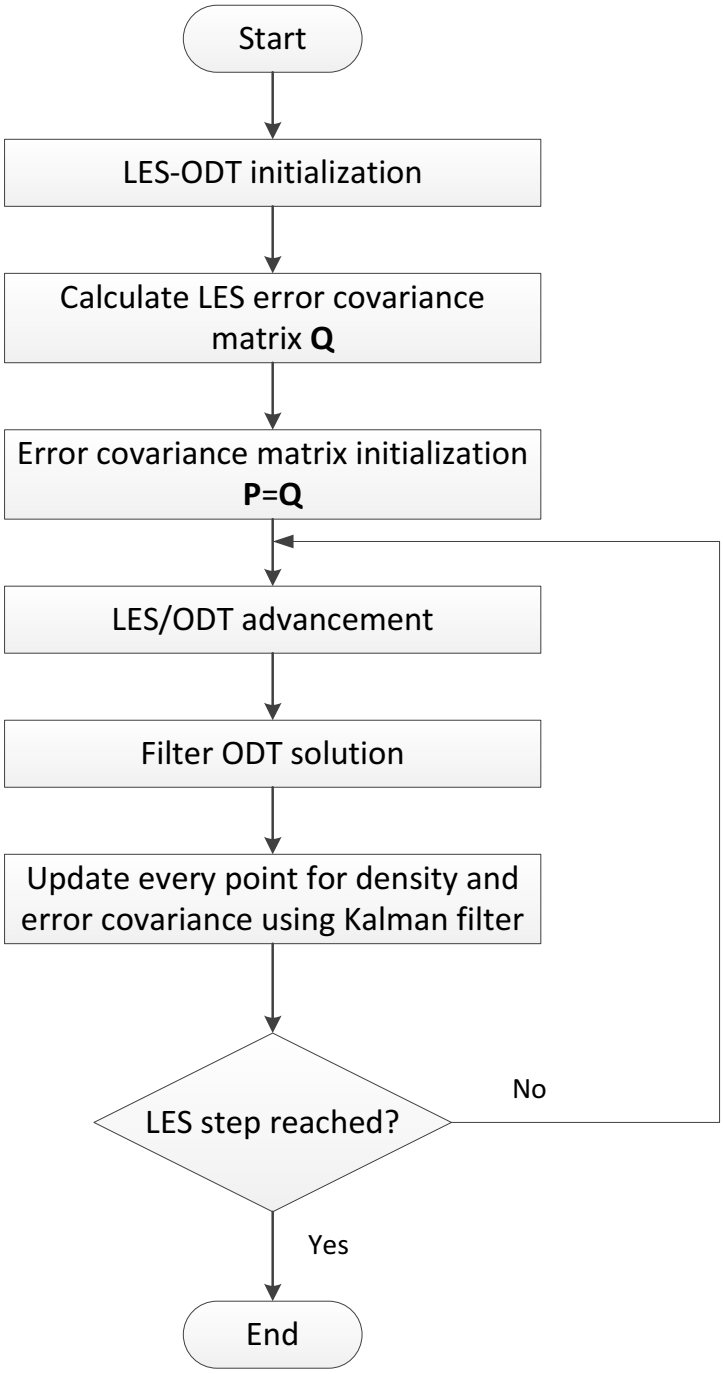

Figure 5.2: Flowchart for Kalman filter implementation.

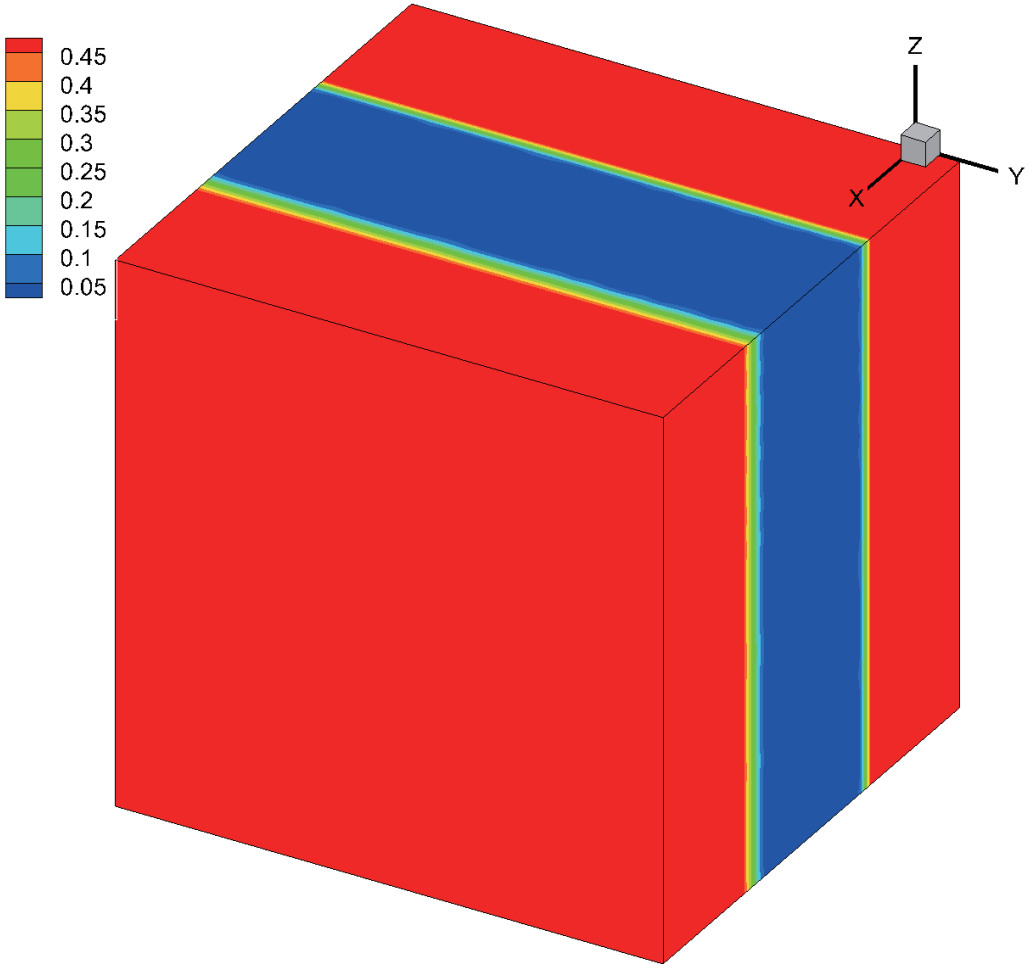

Figure 5.3: Initial mass fraction field for both reactant and oxidizer.

Table 5.1: Parameter for LES-ODT formulation

Domain dimension	$3.6 \times 3.6 \times 3.6$
Re	100
zeroth-order pressure	1.0
Prandtl number	0.7
Lewis number	1.0
Damköhler number	200
non-dimensional heat release	0.75
non-dimensional activation energy	6.0
x boundary condition	outlet
y boundary condition	periodic
z boundary condition	periodic

non-dimensional heat release α, non-dimensional activation energy β, Damköhler number Da and zeroth-order pressure P_0 are definied in Eqs. (4.16)–(4.21).

The LES has a formulation of $33 \times 33 \times 33$ across the whole domain with an integration time step of $\Delta t = 0.01$. Every ODT domain has the length of 3.6 with 257 grid points. Viscosity penalty is discussed in Chapter 2; the velocity energy exchange coefficients is also presented in Chapter 2. The initial turbulence is prescribed using a von Kalman-Pao spectrum with zero mean velocity [60]. The boundary condition is outlet boundary condition for x direction of LES and x orientation ODT domains. It is periodic for y and z directions of LES and y and z orientation ODT domains.

Table 5.2: Parameter for LES simulation.

LES domain dimension	$3.6 \times 3.6 \times 3.6$
LES grid	$33 \times 33 \times 33$
LES time step	0.01
SGS stress model	Smagorinsky model

Table 5.3: Parameter for ODT simulation.

Domain length	3.6
ODT grid	257
number of ODT domains	3267 ($3 \times 33 \times 33$)
viscosity penalty	0.002
minimum eddy size	6
degree of energy exchange among velocities in ODT	0.33
ratio of maximum ODT eddy size to LES grid size	2
maximum ODT eddy size	16
ODT stirring time step	1.0×10^{-5}
ODT diffusion and reaction time step	1.2×10^{-5}
ODT convection time step	0.9×10^{-5}

5.2.2 Comparison with the Filtered ODT and LES

The comparison between the filtered ODT density and the density after the Kalman filter is shown in Figure 5.4. The iso-contour of the density field after the Kalman filter shows much less fluctuations and smoother flame surface. The density after the Kalman filter also shows some other difference with the filtered ODT density other than small scale fluctuations. This is because that the Kalman filter takes consideration of both density field rather than smoothing the filtered ODT density.

The Fourier spectra are given for the LES density field, the filtered ODT density field and the density field after Kalman filter based on the LES and filtered ODT density field in Figure 5.5 for further illustration. Due to the limited grid points in the LES-ODT implementation, the energy spectra shown in the graph are obtained by averaging the energy spectra over all the ODT domains or the corresponding LES lines. The average eliminates energy fluctuations due to the limited grid number with the overall trend of changes remain. In Figure 5.5, the Fourier spectrum of the density after Kalman filter shows less fluctuations in small scale which corresponds to the lower energy in high wave number. On the contrary, the ODT density field exhibits several peaks in high wave number region, which is an indication of the non-smoothness of the density profile in the physical domain.

5.2.3 Comparison with DNS

The flame structure of the simulation case described in Tables. (5.1)–(5.3) is shown as the iso-surface of temperature at $T = 0.5$. The iso-surfaces in Figure 5.6 are presented at different dimensionless times $t = 0.1$, $t = 0.2$, $t = 0.3$ and $t = 0.4$. The twin flames wrinkle at early times and eventually interact with each other. Thus, the twin flame case

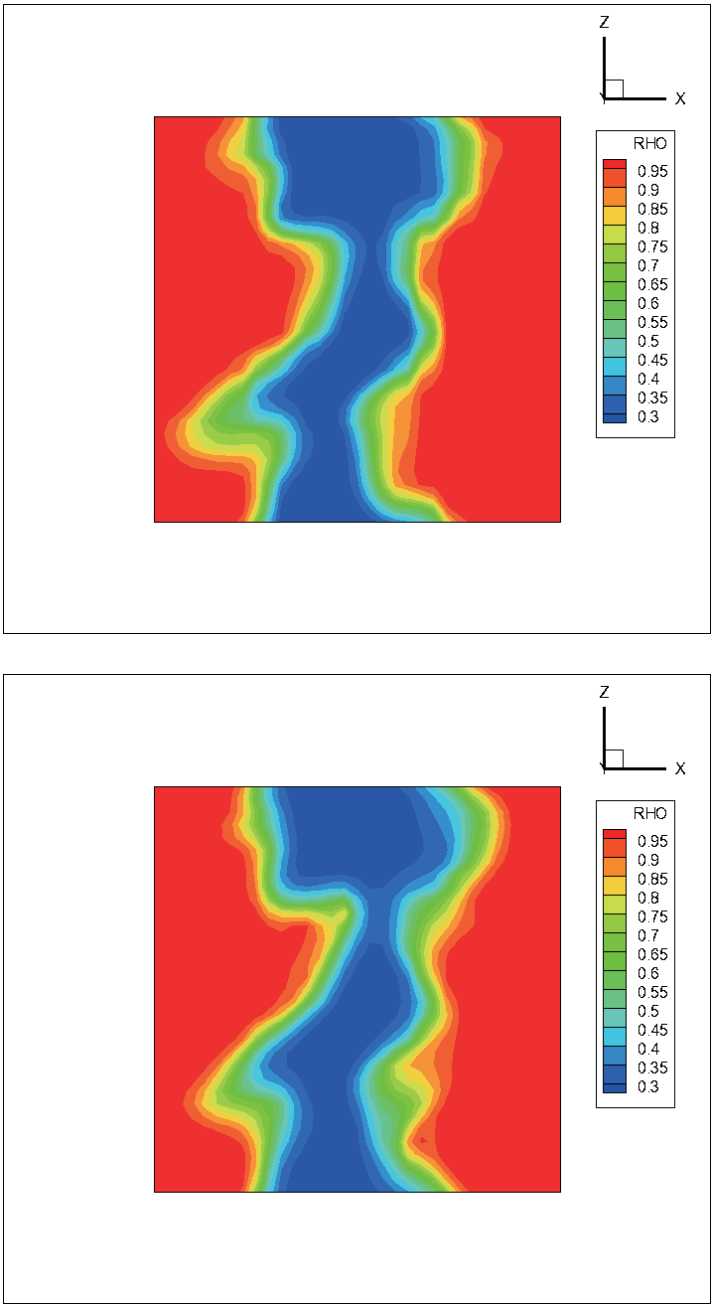

Figure 5.4: Comparison of a density slice between the filtered ODT density (upper) and the density after the Kalman filter (lower).

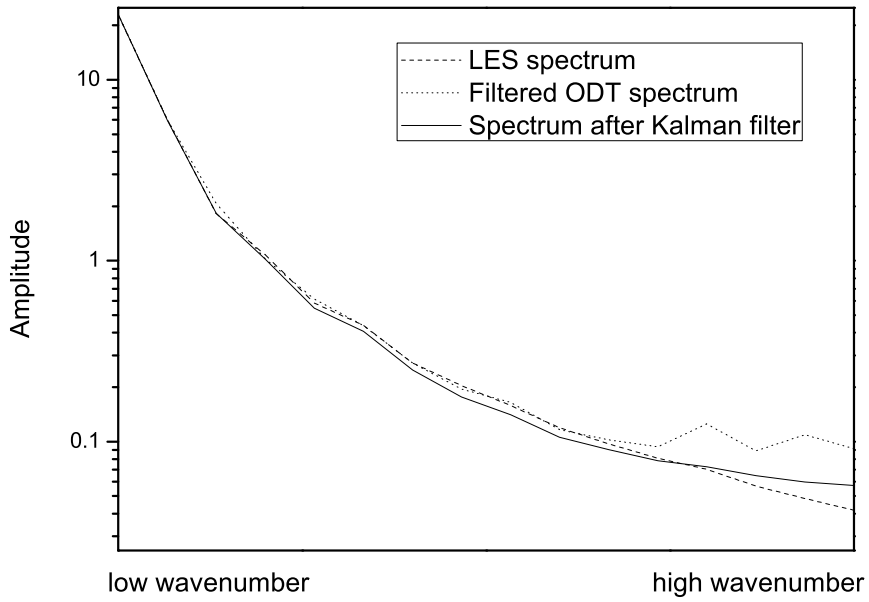

Figure 5.5: FFT spectra for the density field of LES, filtered ODT and Kalman filter.

shown here provide a convincing way of proving the ability to predict the flame structure and statistics for the LES-ODT formulation with the Kalman filter implementation.

The comparison between the LES-ODT formulation and the DNS formulation is carried out. The DNS governing equations are express as

Continuity Equation:

$$\frac{\partial \rho}{\partial t} + \frac{\partial \rho u_j}{\partial x_j} = 0 \tag{5.18}$$

Momentum Equation:

$$\frac{u_i}{\partial t} + u_j \frac{\partial u_i}{\partial x_j} = -\frac{1}{\rho}\frac{\partial p}{\partial x_i} + \frac{1}{\rho}\frac{\partial^2 \tau_{ij}}{\partial x_j^2} \tag{5.19}$$

Energy Equation:

$$\frac{\partial T}{\partial t} + u_j \frac{\partial T}{\partial x_j} = \frac{\nu}{\mathrm{Pr}}\frac{\partial^2 T}{\partial x_j^2} + Q\omega \tag{5.20}$$

Species Equation (For both fuel and oxidizer):

$$\frac{\partial Y_{F,O}}{\partial t} + u_j \frac{\partial Y_{F,O}}{\partial x_j} = \frac{\nu}{\mathrm{PrLe}}\frac{\partial^2 Y_{F,O}}{\partial x_j^2} - \omega \tag{5.21}$$

The subscripts 'F' and 'O' refer to the fuel and the oxidizer, respectively. The non-dimensional parameters, Pr and Le, correspond to the Prandtl number and the Lewis number, respectively. The reaction is prescribed by a single step, second order, irreversible reaction of the fuel with the oxidizer:

$$F + O \longrightarrow P. \tag{5.22}$$

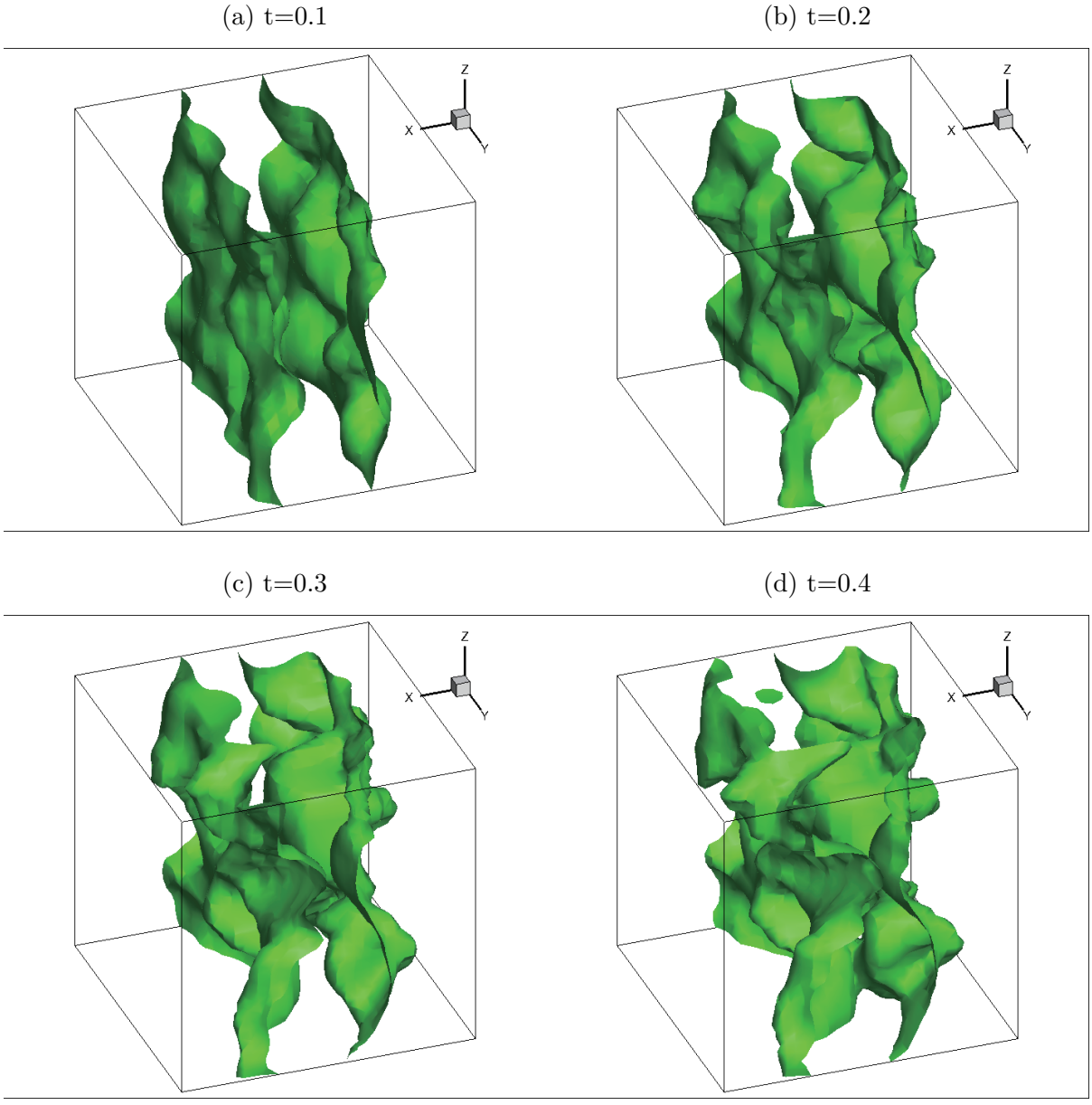

Figure 5.6: Iso-surface of filtered ODT temperature at $T = 0.5$

Table 5.4: Formulation of DNS and LES

	LES formulation	DNS
grid number	33^3	129^3
time step	0.01	0.001
domain size	$3.6 \times 3.6 \times 3.6$	$3.6 \times 3.6 \times 3.6$
Reynolds number	100	100
turbulent intensity u_{rms}	3.0	3.0

The reaction rate is expressed in Arrhenius form:

$$\omega = \mathrm{Da}\rho^2 Y_F Y_O \exp\left[\frac{-\beta(1-T)}{1-\alpha_0(1-T)}\right], \tag{5.23}$$

where α_0 and β are defined in Eq. (4.18) and Eq. (4.19).

The Kalman filter is implemented as the upscaling scheme for the LES-ODT formulation. Both of them have the same non-dimensional turbulence intensity $u_{rms} = 3.0$; the same Reynolds number Re = 100.0; and the same Lewis number which equals to unity. The same boundary conditions are adopted also, with outlet boundary condition in x direction and periodic boundary conditions in y and z directions. The simulation of the DNS has a resolution of 129^3. The LES-ODT is initialized from the DNS field at dimensionless time $t = 0$, therefore, both LES-ODT and DNS have the same initialization field. The DNS initialization field is based on the von Karman-Pao spectrum with zero mean velocity [60]. Some important parameters for the LES-ODT and DNS simulation are shown in Table 5.4.

The comparison between the LES-ODT formulation and the DNS formulation is

shown for temperature as in Figure 5.7 and Figure 5.8, mass fraction as in Figure 5.9 and Figure 5.10, reaction rate as in Figure 5.11 and Figure 5.12. They are all shown in a fixed z plane. The peak reaction rate of filtered ODT is higher than the filtered DNS, which is the result of the multiplicity of reaction fronts due to the higher flame surface density within the LES filter. Furthermore, the higher reaction rate feeds back into LES through density; then the higher density gradient also increases the turbulent convection; which results in a thickened flame structure. The filtered ODT flame also presents the flame structure with less wrinkling. The reason for this is that the filtering eliminates small scale features below the filter size. The difference of the flame thickness between the filtered ODT and the filtered DNS results can be reduced by cycling a number of times of the ODT node convection.

Another LES-ODT formulation with coarser LES implementation is also adopted. The LES has a resolution of $17 \times 17 \times 17$ instead of $33 \times 33 \times 33$ for the finer case discussed above. The comparison of the reaction rate between the filtered ODT for the coarse formulation and the filtered DNS is shown in Figure 5.13 and Figure 5.14, respectively. With the coarse formulation of the LES, less energy is resolved by LES. The ODT has to take consideration of the remaining energy, yet the filtered ODT results still match the filtered DNS results. The effectiveness of upscaling is further proved.

It is also important to address the difference between the computational cost of LES-ODT formulation and DNS. The computational cost of ODT is linearly dependent on DNS resolution in one direction and on the square of the LES resolution in one direction. In the example shown above, with the ODT resolution twice as DNS, DNS has $129^3 = 2,146,689$ grid points, while the total number of ODT points is $257 \times 3 \times 33 \times 33 = 839,619$ for the fine case and $257 \times 3 \times 17 \times 17 = 222,819$ for the coarse case. The saving for computational cost is significant. For the case shown above, the fine case takes about 12

(a) t=0.1 (b) t=0.2

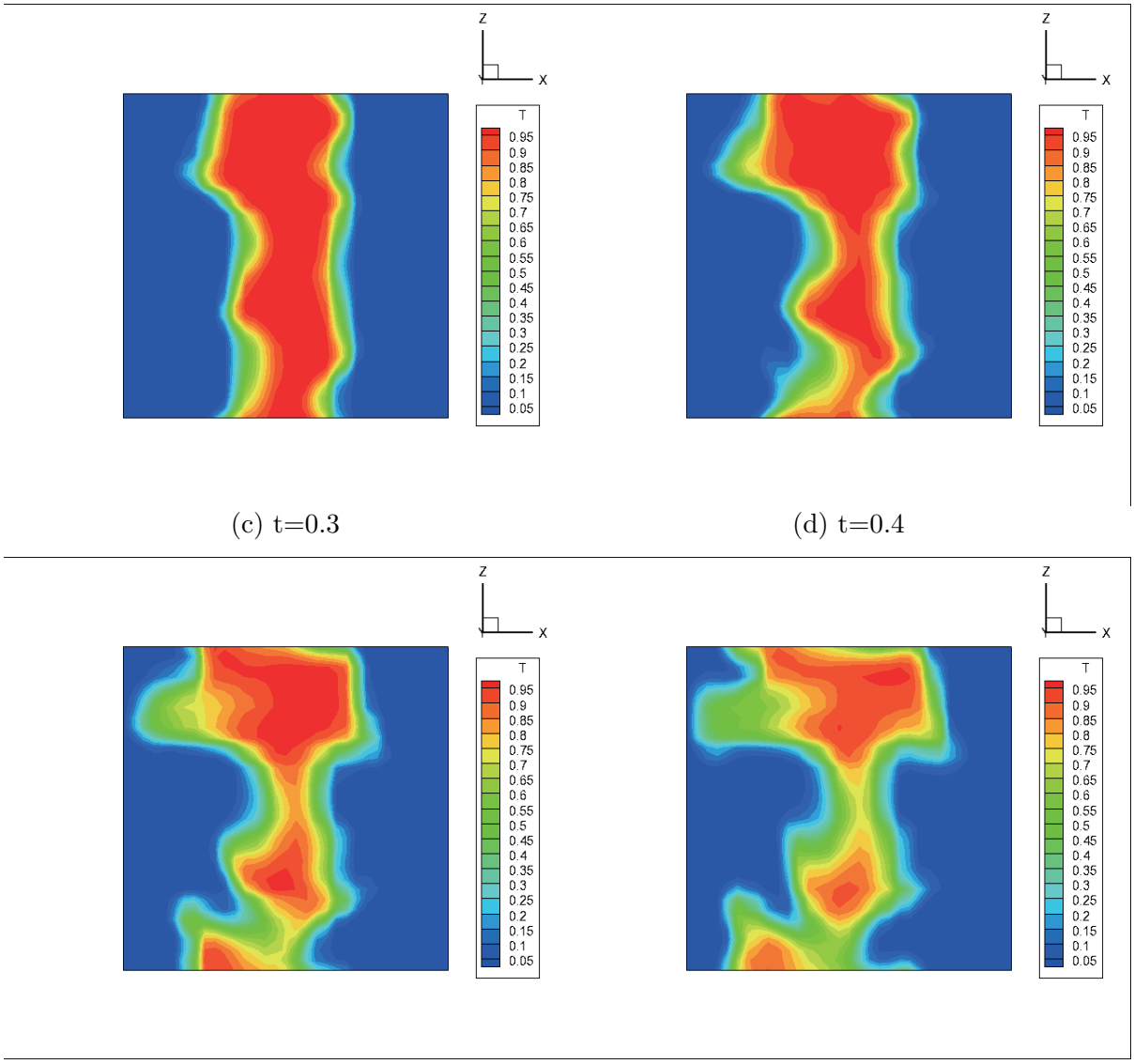

(c) t=0.3 (d) t=0.4

Figure 5.7: Iso-contour of filtered ODT temperature at different times of evolution of the twin flames.

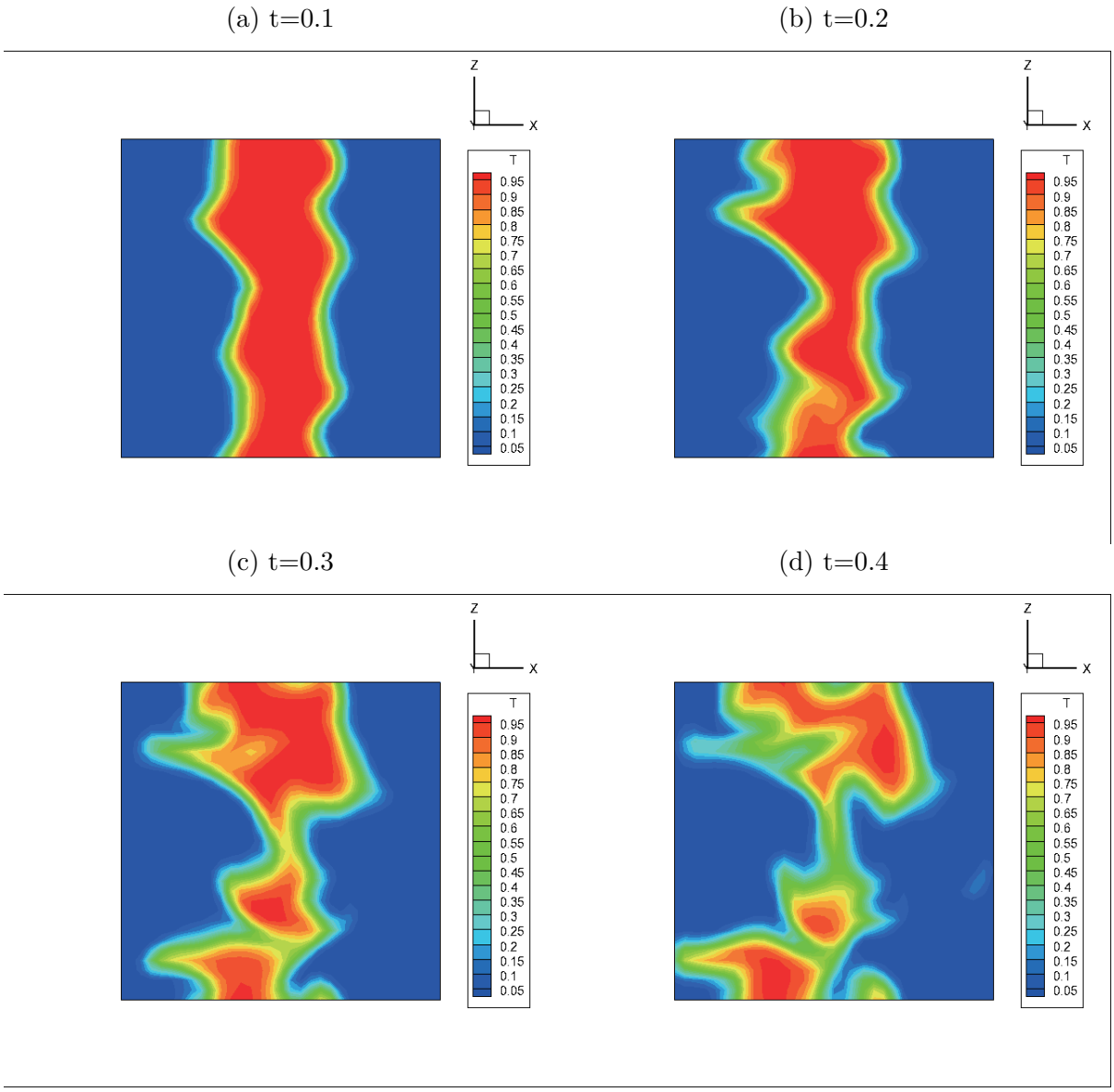

Figure 5.8: Iso-contour of filtered DNS temperature at different times of evolution of the twin flames.

(a) t=0.1 (b) t=0.2

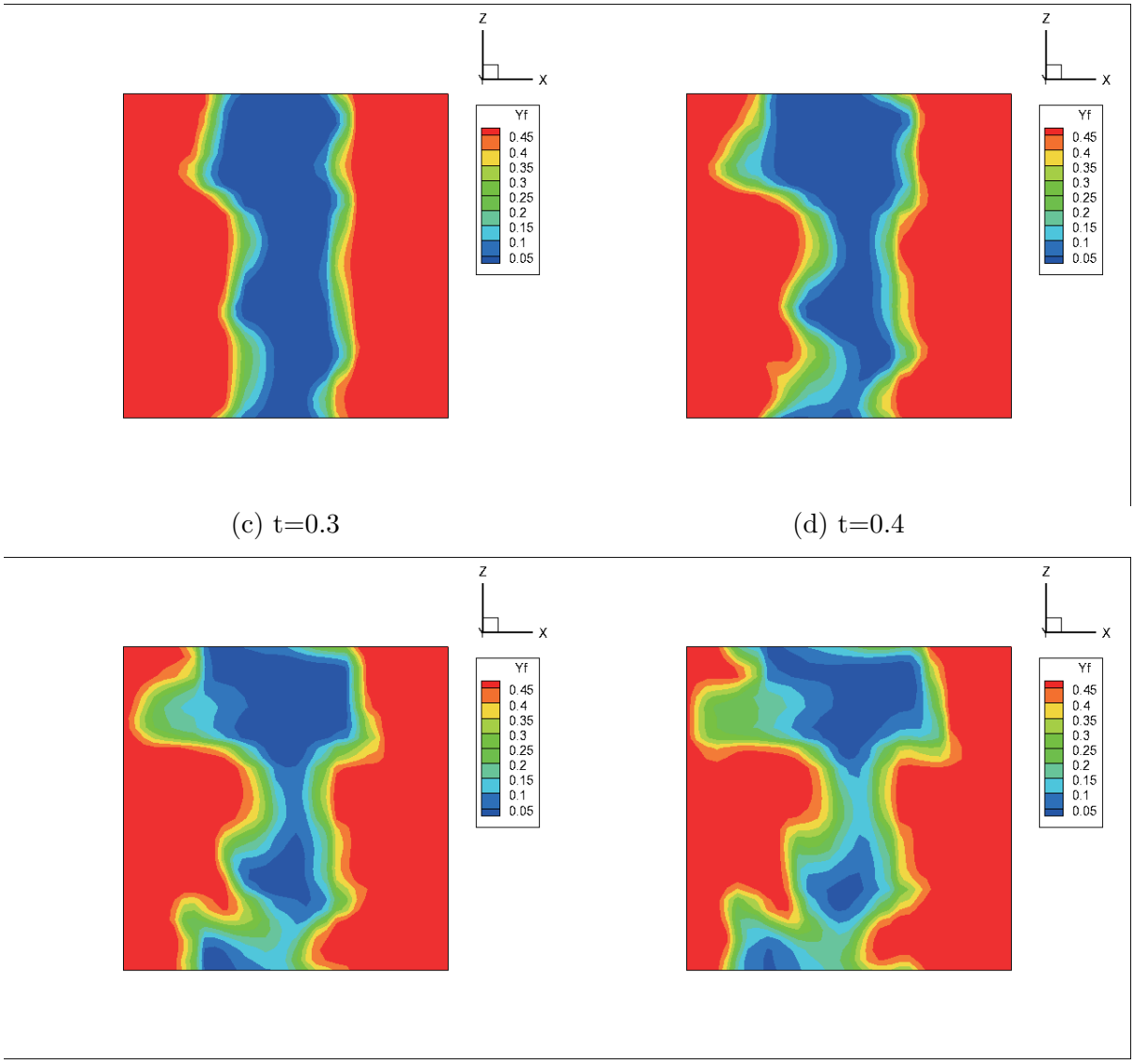

(c) t=0.3 (d) t=0.4

Figure 5.9: Iso-contour of filtered ODT mass fraction at different times of evolution of the twin flames.

(a) t=0.1 (b) t=0.2

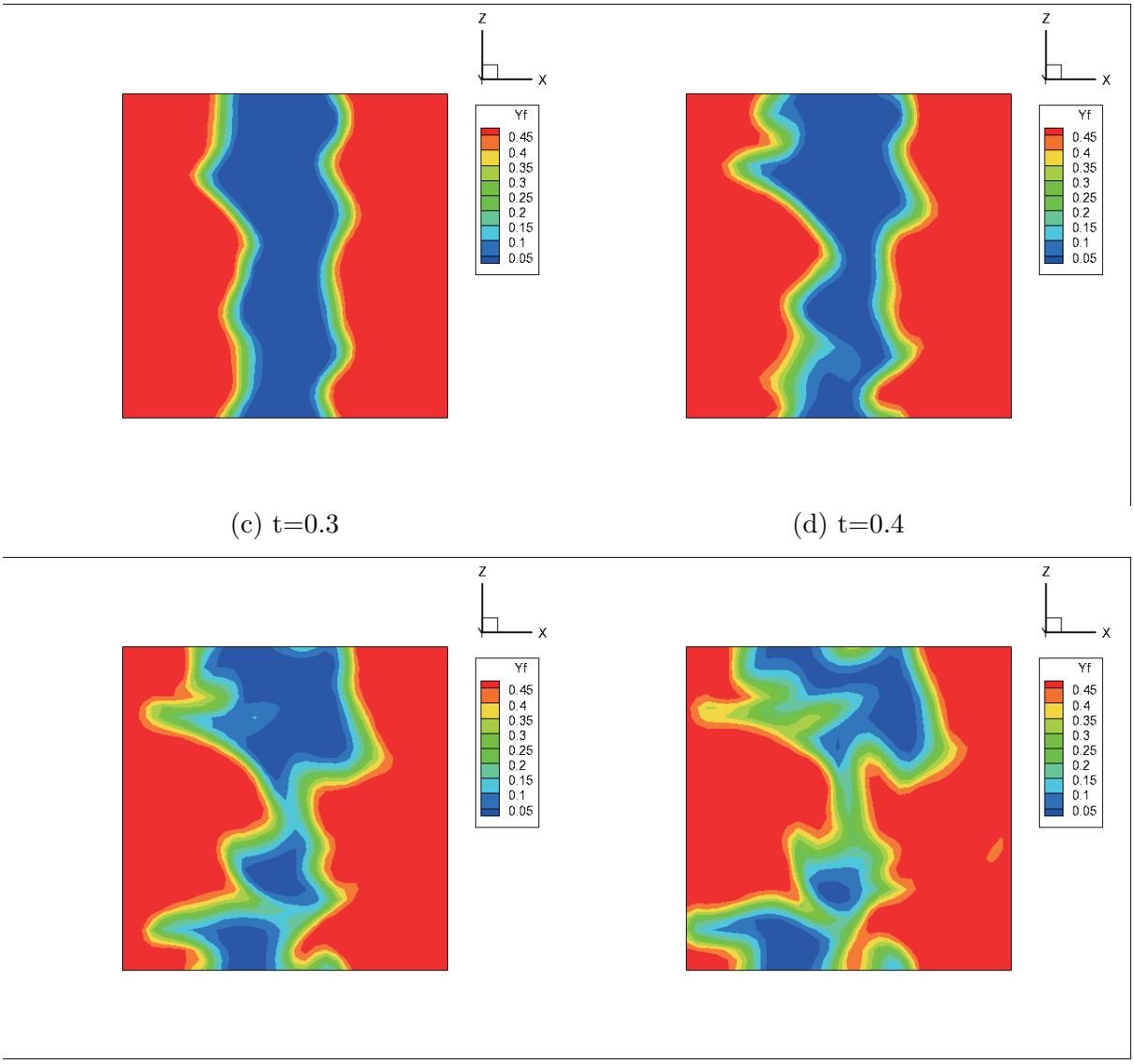

(c) t=0.3 (d) t=0.4

Figure 5.10: Iso-contour of filtered DNS mass fraction at different times of evolution of the twin flames.

(a) t=0.1 (b) t=0.2

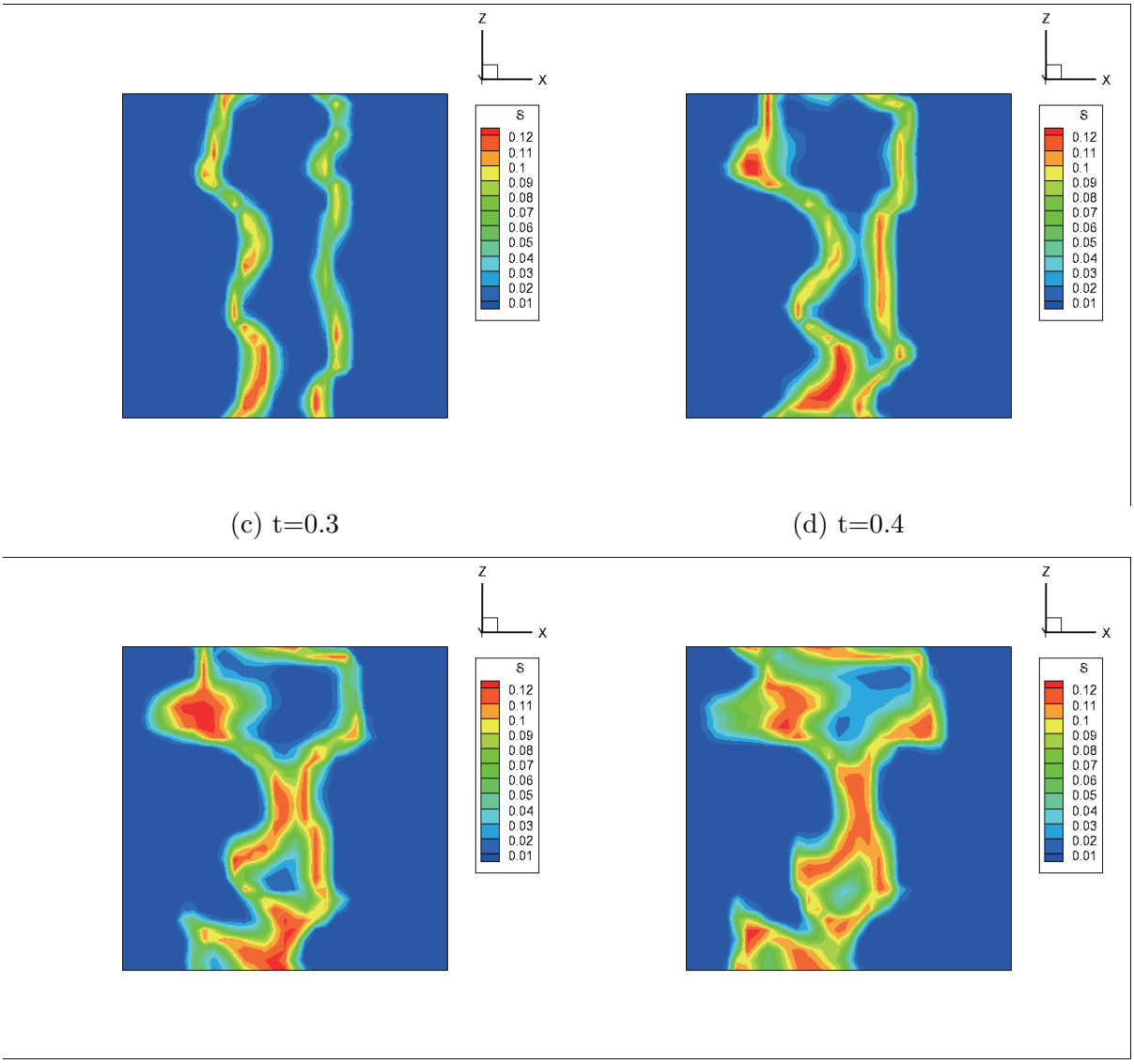

(c) t=0.3 (d) t=0.4

Figure 5.11: Iso-contour of filtered ODT reaction rate at different times of evolution of the twin flames.

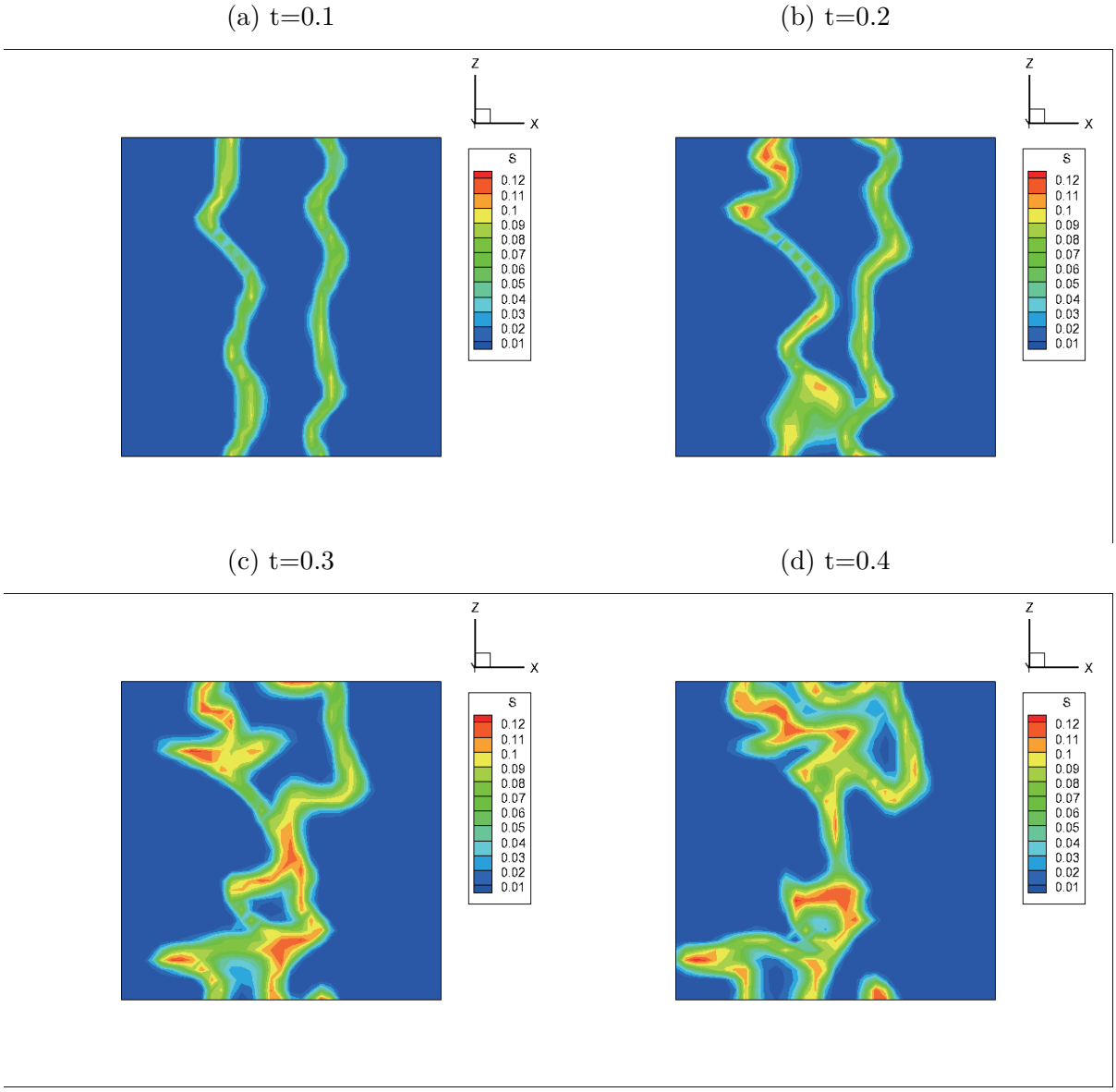

Figure 5.12: Iso-contour of filtered DNS reaction rate at different times of evolution of the twin flames.

(a) t=0.1 (b) t=0.2

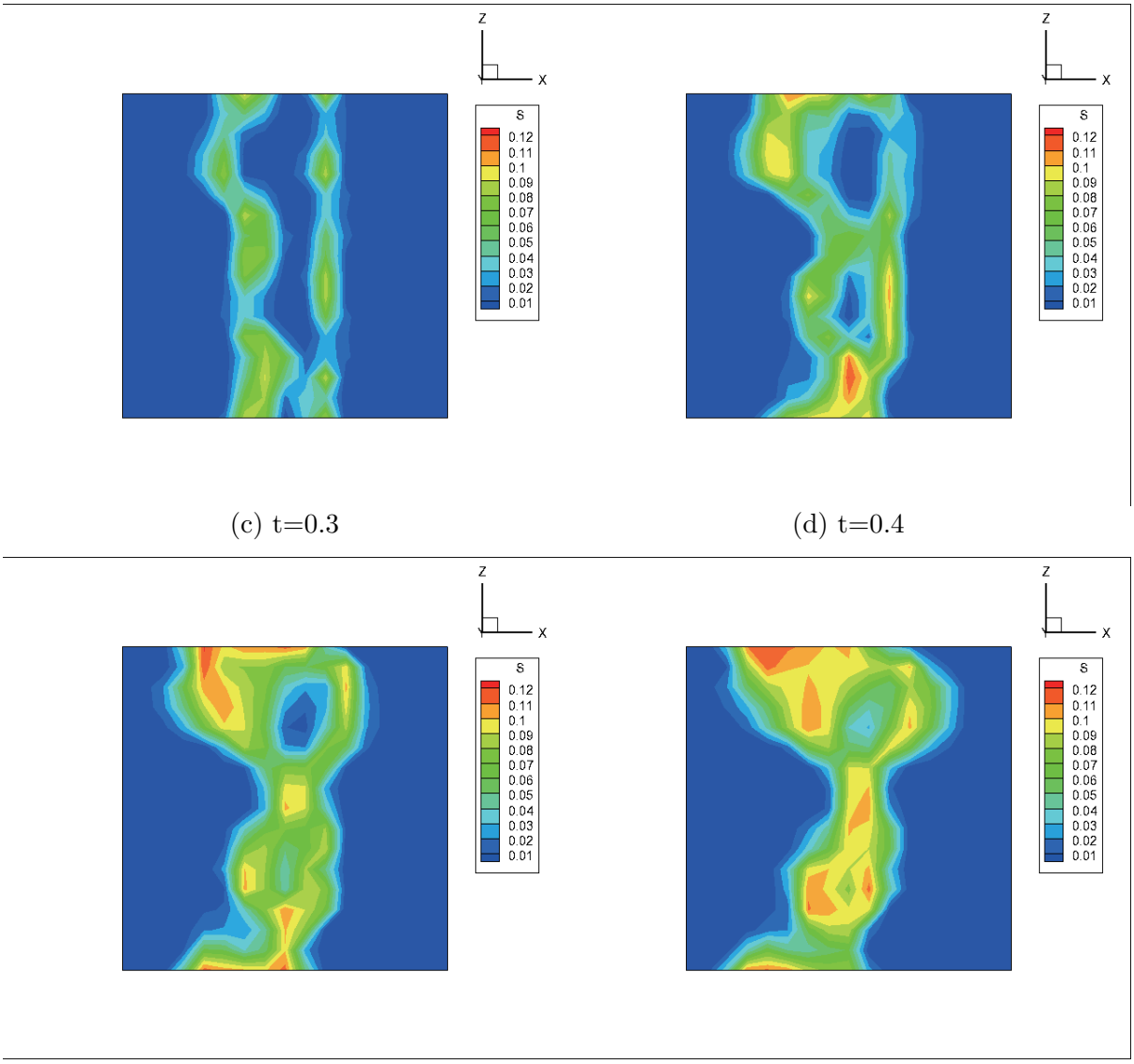

(c) t=0.3 (d) t=0.4

Figure 5.13: Iso-contour of filtered ODT reaction rate based on 17^3 grid at different times of evolution of the twin flames.

(a) t=0.1 (b) t=0.2

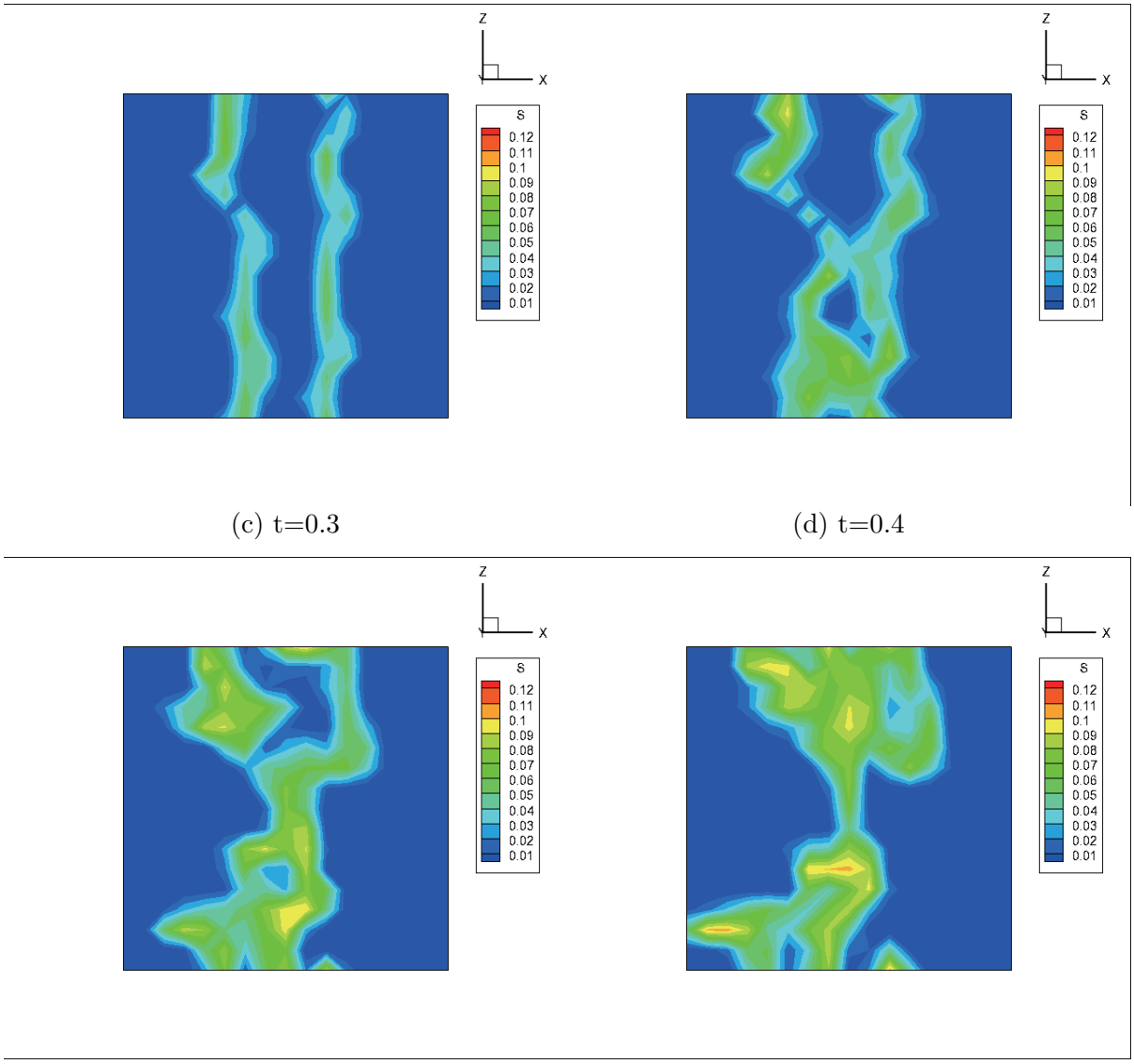

(c) t=0.3 (d) t=0.4

Figure 5.14: Iso-contour of filtered DNS reaction rate based on 17^3 grid at different times of evolution of the twin flames.

hours while the coarse case takes only about 4 hours on a single processor; meanwhile, the DNS simulation takes around 30 hours on the same processor.

5.3 Summary

In this chapter, the upscaling implementation using Kalman filter based approach is applied for the LES-ODT framework. The density field, which is used for the upscaling, is smoothed by the Kalman filter without losing the subgrid contribution. The filtered scalar fields from ODT solution matches the filtered DNS scalar fields. Moreover, with a coarse LES formulation, the filtered ODT can still match the filtered DNS solution, which indicates the effectiveness of the Kalman filter based upscaling.

Chapter 6

Conclusions and Recommendations for Future Work

6.1 Conclusions

In this dissertation, novel strategies for coupling 3D LES with ODT solutions are developed, which involves downscaling and upscaling. Instead of using interpolation and box filtering as the downscaling and the upscaling approaches, the wavelet-based compounding of velocity field is used for the downscaling and the Kalman filter of density field is used for the upscaling.

The wavelet-based downscaling is achieved by combining large scale velocity component from LES with small scale velocity component from ODT. Both of the components are assembled in terms of wavelet coefficients which results in a velocity field with consideration of both LES and ODT. More importantly, the velocity fields after compounding have several important features that are desired for the LES-ODT coupling and simulation, which include:

1. In physical domain, the compounded velocity fields have consistency with LES velocity fields in large scale trend and ODT velocity fields in small scale fluctuation.

2. In Fourier domain, the compounded velocity fields coincide with LES in low wavenumber and ODT in high wavenumber.

3. The compounding is based on the wavelet transform, which is a mathematical method; therefore, it can be applied to any kind of turbulent flows.

4. Daubechies 4 wavelet has a similar shape as the ODT small scale characteristics (triplet map); therefore, it is very effective for extracting ODT information.

5. With the extreme low cost of fast wavelet transform, the compounding is implemented without additional computational cost.

Moreover, the various features that wavelet transform possesses inspires other application, which include spatial filtering and ODT parameter determination. The spatial filtering is applied for density and progress variable. By comparing the wavelet-based spatial filtering with the traditional filtering with box filter, the wavelet-based filtering has the ability to maintain large scale peaks while the box filter is smoothing the peaks without catching them. The Fourier analysis also shows that the wavelet-based filtering is well behaved and attached with the density function across all the frequencies that the filtered density has. The ability to maintain the peak of the function for the wavelet-based filtering is used to capture the combustion features of the auto-ignition in non-homogeneous mixture in decaying isotropic turbulence case. Flame kernels spreading across the whole computational domain are detected and well preserved.

The ODT parameter determination is inspired by the fact that the wavelet energy spectrum is smoother than the Fourier energy spectrum. By adjusting the ODT param-

eter, the slope of the energy spectra of LES and ODT matches at the compounding scale. With limited number of grid points, which is far away from generating smooth Fourier spectrum, the wavelet transform provides a robust way of determining the ODT parameter from the energy spectra of both LES and ODT.

The Kalman filter based upscaling is also implemented. The prediction is obtained from the LES density and the observation is obtained from the filtered ODT density which takes consideration of chemical scalars. In this way, reaction from the ODT and continuity from the LES are both accounted. With the assumption that the evolution of the large scale density from LES is very slow compared to the evolution of the small scale density from ODT, the computational cost of the Kalman filter is greatly reduced. The density field after Kalman filter is smoother than the filtered ODT solution which is demonstrated in Fourier domain. Comparison between the LES-ODT with Kalman filter implementation and the filtered DNS is demonstrated for a twin planar premixed flames in decaying isotropic turbulence case. Two LES resolution configurations are used for the comparison, the resolution of $17 \times 17 \times 17$ and the resolution of $33 \times 33 \times 33$. The comparison is shown for temperature, mass fraction and reaction rate between both configurations and their correspondent filtered DNS results. This demonstrates that the LES-ODT with Kalman filter based upscaling shows similar flame topologies as DNS.

6.2 Recommendations for Future Work

6.2.1 Local Determination of the ODT Parameter

The ODT parameter determination is based on the slope of the wavelet energy spectra for both LES and ODT. Because the result of wavelet transform has two parameters,

location parameter b and scale parameter a. Therefore, the wavelet energy spectrum can be calculated locally, or expressed as

$$E(a, b_m \leq b \leq b_n) = \sum_{i=m}^{i=n} W(a, b_i)^2. \tag{6.1}$$

$W(a, b_i)$ is the wavelet coefficient at scale a and location b_i. Thus, the expression shown in Eq. (6.1) represents the energy at scale a for a certain physical span $b_m \leq b \leq b_n$. The ODT parameter determination can be expanded for each flow section. Finer resolution enables more flow sections thus more precise control of the flow field.

6.2.2 Expansion of the Kalman Filter Implementation

The Kalman filter is implemented with the assumption that the evolution of the large scale density from LES is very slow compared to the evolution of the small scale density from ODT so that no deterministic evolution is prescribed. An alternative for density evolution from the LES could come from the continuity equation. If the LES has a resolution of N^3, a $N^3 \times N^3$ matrix inversion would be way more expensive to afford. The ensemble Kalman filter (EnKF) could be used to solve this problem. By selecting a portion of the grids, the computational cost will be greatly reduced.

6.2.3 Application to Other Types of Flows

The current LES-ODT framework is validated for the non-homogeneous auto-ignition in isotropic turbulence case and the twin planar premixed flames in decaying isotropic turbulence case. Applying the LES-ODT formulation discussed in this dissertation to other more general cases would be challenging yet exciting.

REFERENCES

[1] R. Bilger. Conditional moment closure for turbulent reacting flow. *Physics of Fluids A: Fluid Dynamics*, 5(2):436, 1993.

[2] R. Bilger, S. Pope, K. Bray, and J. Driscoll. Paradigms in turbulent combustion research. *Proceedings of the Combustion Institute*, 30(1):21–42, Jan. 2005.

[3] K. Bray, P. A. Libby, and J. Moss. Unified modeling approach for premixed turbulent combustionPart I: General formulation. *Combustion and Flame*, 61(1):87–102, July 1985.

[4] R. G. Brown and P. Y. Hwang. *Introduction to Random Signal and Applied Kalman Filtering with Matlab Exercises and Solutions*. John Wiley, Hoboken, NJ, 4th edition, 2012.

[5] C. Burrus, R. Gopinath, and H. Guo. *Introduction to wavelets and wavelet transforms: a primer*. Prentice Hall, Upper Saddle River, N.J., 1998.

[6] A. Cahuzac, J. Boudet, P. Borgnat, and E. Lévêque. Smoothing algorithms for mean-flow extraction in large-eddy simulation of complex turbulent flows. *Physics of Fluids*, 22(12):125104, 2010.

[7] A. Cahuzac, J. Boudet, P. Borgnat, and E. Lévêque. Dynamic Kalman filtering to separate low-frequency instabilities from turbulent fluctuations: Application to the Large-Eddy Simulation of unsteady turbulent flows. *Journal of Physics: Conference Series*, 318(4):042047, Dec. 2011.

[8] S. Cao. *A novel hybrid scheme for Large Eddy Simulation of turbulent combustion based on the One-Dimensional Turbulence model*. PhD thesis, North Carolina State Unversity, 2006.

[9] S. Cao and T. Echekki. A low-dimensional stochastic closure model for combustion large-eddy simulation. *Journal of Turbulence*, 9(2):1–35, 2008.

[10] V. Chakravarthy and S. Menon. Subgrid modeling of turbulent premixed flames in the flamelet regime. *Flow, Turbulence and Combustion*, 65(2):133–161, 2000.

[11] J. H. Chen. Petascale direct numerical simulation of turbulent combustionfundamental insights towards predictive models. *Proceedings of the Combustion Institute*, 33(1):99–123, 2011.

[12] I. Daubechies. *Ten lectures on wavelets*. Society for Industrial and Applied Mathematics, Philadelphia, 1992.

[13] L. Davidson and S. H. Peng. Hybrid LES-RANS modelling: a one-equation SGS model combined with a k-ω model for predicting recirculating flows. *International Journal for Numerical Methods in Fluids*, 43(9):1003–1018, Nov. 2003.

[14] T. Echekki and K. G. Gupta. Hydrogen autoignition in a turbulent jet with preheated co-flow air. *International Journal of Hydrogen Energy*, 34(19):8352–8377, Oct. 2009.

[15] T. Echekki, A. Kerstein, T. Dreeben, and J.-Y. Chen. 'One-dimensional turbulence' simulation of turbulent jet diffusion flames: model formulation and illustrative applications. *Combustion and flame*, 125(3):1083–1105, May 2001.

[16] T. Echekki and E. Mastorakos. *Turbulent combustion modeling: Advances, new trends and perspectives*. Springer, 2011.

[17] G. Evensen. *Data assimilation: the ensemble Kalman filter*. New York : Springer, Dordrecht, 2009.

[18] M. Farge. Wavelet transforms and their applications to turbulence. *Annual Review of Fluid Mechanics*, 24(1):395–457, Jan. 1992.

[19] M. Farge, G. Pellegrino, and K. Schneider. Coherent Vortex Extraction in 3D Turbulent Flows Using Orthogonal Wavelets. *Physical Review Letters*, 87(5):054501, July 2001.

[20] G. Frantziskonis, S. K. Mishra, S. Pannala, S. Simunovic, C. S. Daw, P. Nukala, R. O. Fox, and P. A. Deymier. Wavelet-based Spatiotemporal Multiscaling in Diffusion Problems with Chemically Reactive Boundary. *International Journal for Multiscale Computational Engineering*, 4(5-6):755–770, 2006.

[21] J. Fröhlich and D. von Terzi. Hybrid LES/RANS methods for the simulation of turbulent flows. *Progress in Aerospace Sciences*, 44(5):349–377, July 2008.

[22] B. Galperin and S. Orszag. *Large eddy simulation of complex engineering and geophysical flows*. Cambridge University Press, New York, 1993.

[23] M. Germano, U. Piomelli, P. Moin, and W. H. Cabot. A dynamic subgrid-scale eddy viscosity model. *Physics of Fluids A: Fluid Dynamics*, 3(7):1760, 1991.

[24] S. Ghosal, T. S. Lund, P. Moin, and K. Akselvoll. A dynamic localization model for large-eddy simulation of turbulent flows. *Journal of Fluid Mechanics*, 286(-1):229, Apr. 2006.

[25] J.-C. Golaz, V. E. Larson, J. a. Hansen, D. P. Schanen, and B. M. Griffin. Elucidating Model Inadequacies in a Cloud Parameterization by Use of an Ensemble-Based Calibration Framework. *Monthly Weather Review*, 135(12):4077–4096, Dec. 2007.

[26] K. Hanjalic. Will RANS survive LES? A view of perspectives. *Journal of fluids engineering*, 127(5):831, 2005.

[27] K. Hanjalić and S. Kenjereš. 'T-RANS'Simulation of Deterministic Eddy Structure in Flows Driven by Thermal Buoyancy and Lorentz Force. *Flow, turbulence and combustion*, 66(4):427–451, 2001.

[28] T. Ishihara, T. Gotoh, and Y. Kaneda. Study of HighReynolds Number Isotropic Turbulence by Direct Numerical Simulation. *Annual Review of Fluid Mechanics*, 41(1):165–180, Jan. 2009.

[29] O. Jacobs. *Introduction to control theory*. Oxford University Press, New York, 2nd edition, 1993.

[30] J. Janicka and A. Sadiki. Large eddy simulation of turbulent combustion systems. *Proceedings of the Combustion Institute*, 30(1):537–547, Jan. 2005.

[31] L. E. Jones, R. D. Sandberg, and N. D. Sandham. Direct numerical simulations of forced and unforced separation bubbles on an airfoil at incidence. *Journal of Fluid Mechanics*, 602:175–207, Apr. 2008.

[32] R. Kalman. A new approach to linear filtering and prediction problems. *Journal of basic Engineering*, 82(Series D):35–45, 1960.

[33] R. Kalman and R. Bucy. New results in linear filtering and prediction theory. *Journal of Basic Engineering*, 83(1):95, 1961.

[34] D. Kammler. *A first course in Fourier analysis*. Cambridge University Press, New York, rev. ed edition, 2007.

[35] Y. Kaneda, T. Ishihara, M. Yokokawa, K. Itakura, and A. Uno. Energy dissipation rate and energy spectrum in high resolution direct numerical simulations of turbulence in a periodic box. *Physics of Fluids*, 15(2):L21, 2003.

[36] S. Kenjeres and K. Hanjalic. Transient analysis of RayleighBénard convection with a RANS model. *International journal of heat and fluid flow*, 20(3):329–340, June 1999.

[37] S. Kenjereš and K. Hanjalić. LES, T-RANS and hybrid simulations of thermal convection at high Ra numbers. *International Journal of Heat and Fluid Flow*, 27(5):800–810, Oct. 2006.

[38] A. R. Kerstein. A Linear- Eddy Model of Turbulent Scalar Transport and Mixing. *Combustion Science and Technology*, 60(4-6):391–421, Aug. 1988.

[39] A. R. Kerstein. Linear-eddy modeling of turbulent transport. II: Application to shear layer mixing. *Combustion and Flame*, 75(3-4):397–413, Mar. 1989.

[40] A. R. Kerstein. Linear-eddy modeling of turbulent transport. Part V: Geometry of scalar interfaces. *Physics of Fluids A: Fluid Dynamics*, 3(5):1110, 1991.

[41] A. R. Kerstein. Linear-Eddy modeling of turbulent transport. Part 4. Structure of diffusion flames. *Combustion Science and Technology*, 81(1-3):75–96, Jan. 1992.

[42] A. R. Kerstein. One-dimensional turbulence: model formulation and application to homogeneous turbulence, shear flows, and buoyant stratified flows. *Journal of Fluid Mechanics*, 392:277–334, Aug. 1999.

[43] A. R. Kerstein. Linear-eddy modelling of turbulent transport. Part 3. Mixing and differential molecular diffusion in round jets. *Journal of Fluid Mechanics*, 216(-1):289, Apr. 2006.

[44] A. R. Kerstein, W. T. Ashurst, S. Wunsch, and V. Nilsen. One-dimensional turbulence: vector formulation and application to free shear flows. *Journal of Fluid Mechanics*, 447:85–109, Oct. 2001.

[45] S. H. Kim and H. Pitsch. Conditional filtering method for large-eddy simulation of turbulent nonpremixed combustion. *Physics of Fluids*, 17(10):105103, 2005.

[46] A. Y. Klimenko. Multicomponent diffusion of various admixtures in turbulent flow. *Fluid Dynamics*, 25(3):327–334, 1990.

[47] R. H. Kraichnan. Eddy viscosity in two and three dimensions. *Journal of the Atmospheric Sciences*, 33(8):1521–1536, Aug. 1976.

[48] C. Law. *Combustion physics*. Cambridge University Press, New York, 2006.

[49] S. Leonardi, P. Orlandi, R. Smalley, L. Djenidi, and R. Antonia. Direct numerical simulations of turbulent channel flow with transverse square bars on one wall. *Journal of Fluid Mechanics*, 491:229–238, Sept. 2003.

[50] T. F. Lu, C. S. Yoo, J. H. Chen, and C. K. Law. Three-dimensional direct numerical simulation of a turbulent lifted hydrogen jet flame in heated coflow: a chemical explosive mode analysis. *Journal of Fluid Mechanics*, 652:45–64, May 2010.

[51] F. Magagnato and M. Gabi. A new adaptive turbulence model for unsteady flow fields in rotating machinery. *International Journal of Rotating Machinery*, 2002.

[52] B. Magnussen and B. Hjertager. On mathematical modeling of turbulent combustion with special emphasis on soot formation and combustion. *Symposium (International) on Combustion*, 16(1):719–729, Jan. 1977.

[53] S. D. Mason. *Turbulence transport in spatially developing reacting shear layers*. PhD thesis, University of Wisconsin-Madison, 2000.

[54] P. Maybeck. *Stochastic models, estimation, and control*. Academic Press, New York, 1979.

[55] R. McDermott. *Toward one-dimensional turbulence subgrid closure for large-eddy simulation*. PhD thesis, The University of Utah, 2005.

[56] F. R. Menter. Two-equation eddy-viscosity turbulence models for engineering applications. *AIAA Journal*, 32(8):1598–1605, Aug. 1994.

[57] H. Mouri, H. Kubotani, T. Fujitani, H. Niino, and M. Takaoka. Wavelet analyses of velocities in laboratory isotropic turbulence. *Journal of Fluid Mechanics*, 389:229–254, June 1999.

[58] K. Muralidharan and S. Mishra. Dynamic compound wavelet matrix method for multiphysics and multiscale problems. *Physical Review E*, 77(2):026714, Feb. 2008.

[59] S. Orszag and G. P. Jr. Numerical simulation of three-dimensional homogeneous isotropic turbulence. *Physical Review Letters*, 28(January), 1972.

[60] J. Park and T. Echekki. LESODT study of turbulent premixed interacting flames. *Combustion and Flame*, 159:609–620, 2012.

[61] N. Peters. Local quenching due to flame stretch and non-premixed turbulent combustion. *Combustion Science and Technology*, 30(1-6):1–17, Jan. 1983.

[62] C. Pierce and P. Moin. Progress-variable approach for large-eddy simulation of non-premixed turbulent combustion. *Journal of Fluid Mechanics*, 504(March 2002):73–97, Apr. 2004.

[63] U. Piomelli. Large-eddy simulation: achievements and challenges. *Progress in Aerospace Sciences*, 35(4):335–362, May 1999.

[64] H. Pitsch. Large-eddy simulation of turbulent combustion. *Annu. Rev. Fluid Mech.*, 38(1):453–482, Jan. 2006.

[65] S. Pope. *Turbulent flows*. Cambridge University Press, 2000.

[66] S. Pope. Ten questions concerning the large-eddy simulation of turbulent flows. *New Journal of Physics*, 6:35–35, Mar. 2004.

[67] A. J. Ricks, J. C. Hewson, A. R. Kerstein, J. P. Gore, S. R. Tieszen, and W. T. Ashurst. A Spatially Developing One-Dimensional Turbulence (ODT) Study of Soot and Enthalpy Evolution in Meter-Scale Buoyant Turbulent Flames. *Combustion Science and Technology*, 182(1):60–101, Jan. 2010.

[68] M. J. Ringuett, M. Wu, and M. P. Martin. Coherent structures in direct numerical simulation of turbulent boundary layers at Mach 3. *Journal of Fluid Mechanics*, 594:59–69, Dec. 2007.

[69] S. Ross. A course in simulation. 1990.

[70] A. Sadiki, A. Maltsev, B. Wegner, F. Flemming, A. Kempf, and J. Janicka. Unsteady methods (URANS and LES) for simulation of combustion systems. *International Journal of Thermal Sciences*, 45(8):760–773, Aug. 2006.

[71] F. Sarghini, U. Piomelli, and E. Balaras. Scale-similar models for large-eddy simulations. *Physics of Fluids*, 11(6):1596, 1999.

[72] P. Schlatter and R. Örlü. Assessment of direct numerical simulation data of turbulent boundary layers. *Journal of Fluid Mechanics*, 659:116–126, July 2010.

[73] R. C. Schmidt, A. R. Kerstein, and R. McDermott. ODTLES: A multi-scale model for 3D turbulent flow based on one-dimensional turbulence modeling. *Computer Methods in Applied Mechanics and Engineering*, 199(13-16):865–880, Feb. 2010.

[74] B. Sen and S. Menon. Linear eddy mixing based tabulation and artificial neural networks for large eddy simulations of turbulent flames. *Combustion and Flame*, 157(1):62–74, Jan. 2010.

[75] J. Smagorinsky. General circulation experiments with the primitive equations. *Monthly Weather Review*, 91(3):99–164, Mar. 1963.

[76] K. Sone and S. Menon. Effect of Subgrid Modeling on the In-Cylinder Unsteady Mixing Process in a Direct Injection Engine. *Journal of Engineering for Gas Turbines and Power*, 125(2):435, 2003.

[77] P. Spalart. Strategies for turbulence modelling and simulations. *International Journal of Heat and Fluid Flow*, 21(3):252–263, June 2000.

[78] P. Spalart and S. Allmaras. A one-equation turbulence model for aerodynamic flows. *Recherche Aerospatiale*, (1):5–21, 1994.

[79] D. Spalding. Mixing and chemical reaction in steady confined turbulent flames. *Symposium (International) on Combustion*, 13(1):649–657, Jan. 1971.

[80] S. Srivastava and T. Echekki. A Smoothing Approach for a Hybrid Reacting Flow Coarse-Fine Grained Scheme. Technical report, North Carolina State University, Raleigh, 2012.

[81] A. Travin, M. Shur, M. Strelets, and P. Spalart. Detached-eddy simulations past a circular cylinder. *Flow, Turbulence and Combustion*, 63(1):293–313, 2000.

[82] B. Wegner, A. Maltsev, C. Schneider, A. Sadiki, A. Dreizler, and J. Janicka. Assessment of unsteady RANS in predicting swirl flow instability based on LES and experiments. *International Journal of Heat and Fluid Flow*, 25(3):528–536, June 2004.

[83] G. Welch and G. Bishop. An introduction to the Kalman filter, 2001.

[84] X. Wu and P. Moin. A direct numerical simulation study on the mean velocity characteristics in turbulent pipe flow. *Journal of Fluid Mechanics*, 608:81–112, July 2008.

[85] X. Wu and P. Moin. Direct numerical simulation of turbulence in a nominally zero-pressure-gradient flat-plate boundary layer. *Journal of Fluid Mechanics*, 630:5, June 2009.

[86] S. Wunsch and A. Kerstein. A model for layer formation in stably stratified turbulence. *Physics of Fluids*, 13(3):702, 2001.